UNIVERSIDADE ESTADUAL PAULISTA
"JÚLIO DE MESQUITA FILHO"
CAMPUS DE GUARATINGUETÁ

THALITA MAYUMI CASTALDELLI NISHIME

Development and characterization of extended and flexible plasma jets

Guaratinguetá - SP
2019

Thalita Mayumi Castaldelli Nishime

Development and characterization of extended and flexible plasma jets

PhD thesis presented to the School of Engineering of Guaratinguetá, São Paulo State University, as part of the requirements for achievement of the title: Doctor in Physics in the field of Plasma Physics and Electrical Discharges.

Supervisor: Prof. Dr. Konstantin Georgiev Kostov
Co-supervisor: Profª. Drª. Cristiane Yumi Koga-Ito
Co-supervisor: Dr. Jörn Winter

Guaratinguetá - SP
2019

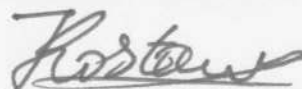**unesp** ✦ UNIVERSIDADE ESTADUAL PAULISTA
CAMPUS DE GUARATINGUETÁ

THALITA MAYUMI CASTALDELLI NISHIME

ESTA TESE FOI JULGADA ADEQUADA PARA A OBTENÇÃO DO TÍTULO DE

"DOUTOR EM FÍSICA"

PROGRAMA: FÍSICA

APROVADA EM SUA FORMA FINAL PELO PROGRAMA DE PÓS-GRADUAÇÃO

Prof. Dr. Konstatin Georgiev Kostov
Coordenador

BANCA EXAMINADORA:

Prof. Dr. KONSTANTIN GEORGIEV KOSTOV
Orientador / UNESP/FEG

Prof. Dr. FELLYPE DO NASCIMENTO
UNICAMP

Prof. Dr. RODRIGO SAVIO PESSOA
ITA

Prof.ª Drª. CARINA BARROS MELLO
INPE/SJC

Prof. Dr. GILBERTO PETRACONI FILHO
ITA/cta

Agosto de 2019

CURRICULAR DATA

THALITA MAYUMI CASTALDELLI NISHIME

BORN   01.07.1991 – São Paulo / SP – Brazil

FILIATION   Alberto Nobuo Nishime
Ieda Soraia Castaldelli Nishime

2009/2014   Bachelor in Physics
School of Engineering, Guaratinguetá
Universidade Estadual Paulista "Júlio de Mesquita Filho" (Unesp)

2014/2015   Master in Physics
School of Engineering, Guaratinguetá
Universidade Estadual Paulista "Júlio de Mesquita Filho" (Unesp)

2015/2019   Ph.D. in Physics
School of Engineering, Guaratinguetá
Universidade Estadual Paulista "Júlio de Mesquita Filho" (Unesp)

2017/2017   Sandwich Ph.D. in Plasma Physics
Plasma Sources Department
Leibniz Institute for Plasma Science and Technology (INP), Germany

To my parents

De modo especial, dedico esta tese aos meus pais, por todo o apoio e carinho ao longo dessa jornada.

ACKNOWLEDGMENTS

My most sincere thanks to Felipe V. P. Kodaira for being always by my side and supporting me no matter what.

I would like to thank my family for all the support at all times and for everything they have always done for me.

Finally, I would like to thank everyone that somehow contributed for making this work possible.

"The one thing that you have that nobody else has is you. Your voice, your mind, your story, your vision. So write and draw and build and play and dance and live as only you can."

Neil Gaiman

ABSTRACT

The use of atmospheric pressure plasmas for different purposes has increased in recent years. With the development of atmospheric pressure plasma jets, some precise treatments such as in the biomedical field or specific surface processing became more often. However, the delivery of plasma to irregular shaped objects, inside tubes or even hollow organs is limited with the use of conventional plasma jet configurations. Therefore, those limitations can be surpassed with the development of elongated or remotely generated plasma jets. In this work, two extended plasma jet configurations aiming at different application fields were further developed and characterized. Firstly, an endoscopic plasma jet (plasma endoscope) operating with a dielectric barrier discharge (DBD) configuration in millimeter dimensions that can be coupled to a typical endoscope was developed. This plasma jet can operate with helium or neon and counts with an external concentric shielding gas channel that provides the introduction of an electronegative gas curtain around the plasma plume. The shielding gas allows the preservation of the plasma jet shape when operated inside closed cavities. The construction difficulties arisen from the use of different feed and shielding gases were explored. Carbon dioxide was proven to be a good option for the curtain gas around the plasma plume avoiding the formation of parasitic discharges inside the shielding gas tube and the endoscopic housing. When operated with neon, the plasma jet was ignited with lower applied voltages and reached a wider range of transferred power. The other developed plasma jet was the remotely generated long tube plasma jet that consists of a DBD primary discharge connected to a 1 m long flexible plastic tube with a floating metal wire inside. The metal wire penetrates a few millimetres inside the discharge and allows the generation of a plasma plume at the end of the plastic tube. This configuration permits safer and better manipulation of the plasma jet. The device was characterized using two different excitation sources, an AC power supply with continuously provided signal and one operating in burst mode. The application of voltage signal in burst mode allowed a fine adjustment of discharge parameters reaching a wider range of power. In the case using "continuous" AC voltage signal, power values up to only 1.2 W were achieved. The primary discharge geometry, when using a parallel plates configuration device, exhibited minimal influence on the plasma mean power. A pin electrode configuration long plasma jet was successfully applied for inhibition of *C. albicans* in inoculated Petri dishes in which inhibition zones were observed after treatment. This plasma jet was also used for surface modification of polyethylene terephthalate (PET) samples using different tilting positions. In this case, reductions of around

60º of water contact angle were observed after plasma exposure for 60s and tilting the plasma jet let to formation of bigger treated areas.

RESUMO

Nos últimos anos, tem intensificado o emprego de plasmas em pressão atmosférica para diferentes aplicações. Com o desenvolvimento dos jatos de plasma em pressão atmosférica, alguns tratamentos precisos, como no campo biomédico ou em específicos processamentos de superfícies, tornaram-se mais frequentes. No entanto, a aplicação de plasma à objetos irregulares, dentro de tubos ou mesmo dentro de órgãos ocos é limitada quando se utilizam configurações convencionais de jatos de plasma. Portanto, essas limitações podem ser superadas com o desenvolvimento de jatos de plasma alongados ou gerados remotamente. Neste trabalho, duas configurações de jato de plasma longo visando diferentes campos de aplicação foram aperfeiçoadas e caracterizadas. Inicialmente foi desenvolvido um jato de plasma endoscópico (plasma endoscope) operando em configuração de descarga por barreira dielétrica (DBD) com dimensões milimétricas, versátil ao acoplamento em endoscópios típicos. Este jato de plasma pode operar com hélio ou neônio e conta com um canal externo e concêntrico de gás que permite a introdução de uma cortina de gás eletronegativo ao redor da pluma de plasma. A cortina de proteção a gás preserva a forma do jato de plasma quando operado dentro de cavidades fechadas. As dificuldades advindas do desenvolvimento deste foram investigadas quando diferentes gases foram testados como cortina de proteção dele, dentre estes, o dióxido de carbono se mostrou uma boa opção evitando a formação de descargas parasitas dentro do tubo de gás de proteção e da estrutura do endoscópio. Quando operado com neônio, o jato de plasma pôde ser iniciado com tensões mais baixas e atinge faixas mais amplas de potência transferida. Outra configuração desenvolvida foi a de jato de plasma de tubo longo gerado remotamente que consiste em uma descarga primária DBD conectada a um tubo plástico flexível de 1 m de comprimento com um fio metálico flutuante em seu interior. O eletrodo metálico penetra alguns milímetros na descarga e permite a geração de uma pluma de plasma na extremidade final do tubo. Esta configuração possibilita uma manipulação mais segura e precisa do jato de plasma. O dispositivo foi caracterizado quando utilizadas duas fontes de excitação diferentes, uma com tensão AC aplicada continuamente e outra operando em modo "burst". O uso de sinal de tensão em modo "pulsado" (burst) permite um ajuste mais preciso dos parâmetros da descarga atingindo um intervalo mais amplo de potência transferida. No caso do emprego da fonte de tensão AC "contínua", a faixa de potência atingida se restringe a apenas 1,2 W. A variação da geometria da descarga primária, quando um reator de placas paralelas foi utilizado, influenciou minimamente a potência média do jato de plasma. Para aplicações, um eletrodo de alta tensão em forma de haste foi utilizado na descarga primária. Com este reator,

a inibição do fungo *C. albicans* inoculado em placas de Petri se fez possível, onde a formação de halos de inibição foi observada após o tratamento com plasma. Este jato também foi utilizado para a modificação de superfície de amostras de politereftalato de etileno (PET) com diferentes ângulos de aplicação. Neste caso, reduções de aproximadamente 60º de ângulo de contato com água foram obtidos após tratamentos por 60s e a inclinação do jato de plasma permitiu um aumento na área tratada.

LIST OF FIGURES

LIST OF TABLES

LIST OF ABBREVIATIONS

AC	Alternating current
APP	Atmospheric pressure plasma
APPJ	Atmospheric Pressure Plasma Jet
DBD	Dielectric Barrier Discharge
DC	Direct current
Dist	Distance between two steps.
DNA	Deoxyribonucleic acid
EEDF	Electron energy distribution function
FOT	Fibre optical thermometer
GaAs	Gallium arsenide
HV	High voltage
ICCD	Intensified charge-coupled device
LTE	Thermodynamic equilibrium
OES	Optical Emission Spectroscopy
PET	Polyethylene terephthalate
PTFE	Polytetrafluoroethylene
M.F.C.	Mass flow controller
Q-V	Charge-voltage
RF	Radio frequency
Rn	Reynolds number
RONS	Reactive oxygen and nitrogen species
ROS	Reactive oxygen species
RNS	Reactive nitrogen species
sccm	Standard cubic centimetre
SD	Sabouraud Dextrose
slm	Standard liters per minute
UV	Ultraviolet
VUV	Vacuum ultravioleta
CFU	Colony-forming unit
WCA	Water contact angle

LIST OF SYMBOLS

He   Helium

Ne   Neon

N_2 Nitrogen

N_2^+ Nitrogen ion

NO_x Nitrogen oxides

CO_2 Carbon dioxide

O_2 Oxygen

O_3 Ozone

OH   Hydroxide

γ Secondary-electron-emission coefficient

V_b Breakdown voltage

d   Distance

p   Pressure

n_e Electron's density

T_e Electron's temperature

T_i Ions temperature

T_g Gas temperature

E'   Local electric field

e   electron charge

R   Avalanche head radius

α Number of ionizations per length of path (Townsend's first coefficient)

E_0 Applied electric field

$V_{r,c}$ Voltage across a resistor (r) or a capacitor (c)

U_c Energy per cycle

V_i Measured voltage in equation 3

I_i Measured current in equation 3

M   Length of recorded data in equation 3

Δt_3 Sample interval of equation 3

T   Period of voltage oscillation

Q   Charge

P   Power

C_{cell} Capacitance of the dielectric

C_{eff} Effective capacitance

U_{gap} Bandgap energy

V_{ion} Ionization potential

Ne*   Neon metastable

He*   Helium metastable

N   Number of oscillation cycles

T_r Repetition period

Δt Period of high voltage oscillations

f   Frequency

D   Duty cycle

CONTENTS

1 INTRODUCTION

Non-thermal atmospheric pressure plasmas have been studied since the 19th century, when dielectric barrier discharges (DBDs) were firstly employed by Siemens for ozone generation (KOGELSCHATZ, 2003). Since then, the use of cold atmospheric plasmas such as DBD and corona discharges have been also investigated for gas purification, electrostatic precipitation and, in the last decades, for materials surface functionalization (BRUGGEMAN; IZA; BRANDENBURG, 2017, VESEL; MOZETIC, 2017). Once they do not require expensive vacuum equipment, atmospheric pressure plasmas are cost-effective alternative for some low-pressure plasma techniques, mainly concerning material processing (VESEL, MOZETIC, 2017). Additionally, in the last years, non-thermal atmospheric pressure plasmas have presented unique applications in biomedical fields such as in the so-called plasma medicine (LAROUSSI, 2018, METELMANN; VON WOEDTKE; WELTMANN, 2018).

There are many ways of generating non-equilibrium plasmas at atmospheric pressure. Among them, the use of asymmetric electrodes (corona discharge) and insulating barrier between the electrodes (DBDs) are the most common. Besides, pulsed applied voltage and high gas flow rates can also be employed (TENDERO et al., 2006). Mostly, at atmospheric pressure, the discharge gaps are in the range from few mm to some cm, which limit the size of objects that can be directly treated (LU; LAROUSSI; PUECH, 2012). To overcome this drawback, cold atmospheric plasmas can be generated in open space by combining some of the above-mentioned methods as in the case of atmospheric pressure plasma jets (APPJs). Thus, APPJs are plasma devices able of generating plasma plumes in open space when a gas flow is flushed through the reactor gap (NEHRA; KUMAR; DWIVEDI, 2008). Because of the non-confined discharge, APPJs have drawn much attention for the treatment of not only large and irregular materials, but also objects that cannot support vacuum conditions (BORGES et al., 2017).

APPJs can be used for treatment of heat-sensitive surfaces such as polymers. In this case, ions, electrons, photons and reactive species are transported to the material, interacting with the surface and functionalizing it (PENKOV et al., 2015, ONYSHCHENKO et al., 2015b). Plasma treatment can activate surfaces (KOSTOV et al., 2014), can be used for cleaning (GOTOH et al., 2016, JIN et al., 2013), etching (LUAN et al., 2017) or improving hydrophobic or hydrophilic properties (KOSTOV et al., 2013, MUSA et al., 2016, VAN DEYNSE et al., 2015, SHAW et al., 2016). Usually, polymers have low surface energy, which leads to poor adhesion. Therefore, APPJs have been successfully used for the surface activation of different polymers improving their adhesion properties (KOSTOV et al., 2014, ONYSHCHENKO; DE GEYTER;

MORENT, 2017). However, plasma jet treatments usually provide a punctual and precise modification, which is interesting for some applications, but disadvantageous for treatment of big surfaces. Thus, the inner surface modification of packages and shallow plastic objects are also possible with APPJ, but the treatment of long tubes can be challenging. Hence, new alternatives need to be investigated.

Another important and growing application of APPJs is in biomedical field such as for sterilization (BORGES et al., 2017, FRICKE et al., 2012a, LIN et al., 2016, MORITZ et al., 2017), wound healing (BREATHNACH et al., 2018, CHENG et al., 2018), blood coagulation (LEE et al., 2012), Dentistry (BORGES et al., 2018, YAMAZAKI et al., 2011) and cancer treatment (KIM et al., 2010, XU et al., 2018, YAN; SHERMAN; KEIDAR, 2017). It has been observed that APPJs can effectively eradicate microorganisms (DAESCHLEIN et al., 2010, NISHIME et al., 2016) and the generated reactive oxygen and nitrogen species (RONS) are pointed out as the major factor responsible for apoptotic cellular retrogression (WEISS et al., 2015). Some investigations concluded that RONS can cause DNA damage and lipid peroxidation (KIM et al., 2010, JOSHI et al., 2011). However, the success of APPJ treatments seems to derive from synergetic effect of several plasma agents, as electric field, UV radiation, energetic electrons and reactive species (KOSTOV et al., 2015a, YUSUPOV et al., 2017). The precise control of plasma treatment dose is crucial for the desired outcome. Low power plasma jets are able to stimulate cell proliferation and heal wounds, while higher power treatment can be used to induce apoptosis of cancer cells (KOSTOV et al., 2015a). As a result of their local effect, plasma jets can be used to precisely treat specific regions like tumors. In this case, the control of treatment area and depth while preserving the surrounding healthy cells can be achieved (RATOVITSKI et al., 2014). APPJs are widely studied for treatment of external tissues or surface treatment when a preliminary surgical procedure is necessary to provide access to the desired spot (BRULLÉ et al., 2012). Thus, one interesting and advantageous plasma jet specification is the development of elongated devices capable of delivering plasma to remote locations inside living bodies, like endoscopy, allowing minimal invasive procedures.

Endoscopes are flexible, slender and tubular instruments used for monitoring hollow organs for diagnostics or surgeries. An endoscope combines fiber optics for illumination, a charge-coupled device for imaging and, in many cases, a working channel to provide surgical instruments at the distal endoscope end. Combining this functionality with a medically active plasma jet would enable physicians to apply plasma and investigate its effects inside the body. For that, the plasma jet size needs to be minimized to few mm diameter and the discharge temperature should not overcome 40ºC (BINENBAUM et al., 2017). Additionally, the device

must be long enough to reach the whole extension, or the plasma needs to be transported through a tube like in the case of transporting plasmas (OMRAN et al., 2017).

There are only few studies regarding the transport of plasma through long dielectric tubes. Robert and coauthors (2009) developed the first transporting plasma device called "plasma gun". It consists of a DBD primary reactor connected to a gas-flushed capillary in which the primary discharge propagates through the entire tube extension generating a plasma plume at its end (ROBERT et al., 2009). The plasma gun was also tested for branching capillaries where T connectors were used and four simultaneous plasma plumes could be achieved (ROBERT et al., 2013). In addition, the discharge propagation through metallic tubes was feasible and the transfer duration was much shorter. Other groups also developed similar long plasma jets. Omran and coauthors (2017) investigated the characteristics of single and multi-channel transporting plasmas from a DBD-like plasma jet. The group studied the discharge propagation mechanisms and concluded that the transporting plasma comprises of discrete ionization waves originated from the HV electrode and propagate by deposition of positive charges at the tube wall creating a high potential region (OMRAN et al., 2017). Onyshchenko and coauthors (2015a) investigated the plasma plume extension when long thin polymeric tubes were placed 3 mm away from the plasma jet nozzle allowing their inner surface treatment. Kostov and coauthors (2015c) studied the propagation of a primary discharge through a long plastic tube with a floating wire inside. This metal wire is in contact with the DBD discharge, thus producing a strong electric field close to the tube end that helps generating a plasma plume at the tip without igniting plasma along the plastic tube. Another class of endoscopic plasma source consists of long plasma jets in which the HV electrode is localized close to the tip end. Examples of this plasma jets class are the RF APPJ arranged at the tip of an elongated and flexible capillary developed by Binenbaum and coauthors (2017) and the hollow core fiber plasma jet with bifilar helicoidally arranged electrodes created by Polak and coauthors (2012).

In the present work, two different elongated plasma jets based in pre-existing devices were investigated. The first, called plasma endoscope, is the miniaturization and improvement of the above-mentioned hollow core fiber plasma jet introduced by Polak and coauthors in 2012. This plasma jet was developed and characterized at the Leibniz Institute for Plasma Science and Technology (INP) in Greifswald, Germany. It consists of a millimeter dimension plasma jet with helicoidal electrode arrangement that can be adapted inside commercial endoscopes. The use of a shielding gas around the main noble gas stream is proved to be crucial for in-body application. The efficiency of different feed and shielding gases are investigated, where the use of carbon dioxide as shielding gas helps reducing formation of parasitic discharges within the

tube. Once the development of this plasma source aims at its operation inside endoscopes, it must fulfill some requirements that are explored throughout the text. The second extended plasma jet studied here consists of a primary DBD reactor connected to a long dielectric tube with an inserted floating metal wire in its axis. It was firstly developed at the São Paulo State University (Unesp), Guaratinguetá, Brazil by Kostov and coauthors (2015c).This jet device generates a remote plasma plume that is far away (~ 1.0 m) from the HV source, in this way allowing safe manipulation of the plasma jet and facilitating plasma application to places of difficult access. In this study, different excitation systems are applied for generating the primary DBD discharge and the role of the primary reactor configuration is investigated. Additionally, applications concerning its microbial efficiency and material surface modification using tilting positions are also explored.

2 LITERATURE REVIEW

2.1 PLASMA

In general, plasma can be described as an electrically neutral and chemically reactive medium composed by high quantities of electrons, free radicals, positive and negative ions and gas molecules in their fundamental or excited state (BITTENCOURT, 2004). Besides, this medium must exhibit a collective behavior, be macroscopically neutral and the electrostatic interactions have to be dominant (SOUZA, 2012). It can be generated in laboratory when energy is applied to a gas, for instance thermal or electric energy or electromagnetic radiation. When electric energy is delivered to the gas, electrons respond quickly to the electric field being accelerated. Thus, they transfer the acquired kinetic energy to the neutral particles by means of collisions (OLDHAM, 2009, TENDERO et al., 2006). The most common inelastic process occurring in the plasma is the so-called electron impact ionization, where a primary electron removes another electron from a neutral particle resulting in the formation of a positive ion and two electrons. These two electrons can start new ionization processes resulting in an avalanche of electrons and ions formation (Townsend avalanche), which forms the discharge (FRIDMAN, 2008). In case of a low-pressure DC discharge, ions are accelerated onto the cathode, which can emit secondary electrons due to ion bombardment. The number of electrons per impinging ion is given by the secondary-electron-emission coefficient γ. If every electron ionizes such a number of atoms that in return results in one new emitted secondary electron, the discharge is called self-sustained. The breakdown voltage V_b of a self-sustained discharge depends on the product pd of the inter-electrodes distance (d) and pressure (p) and expressed by the Paschen's law.

$$V_b = \frac{B(pd)}{\ln[A(pd)] - \ln\left[\ln\left(1 + \frac{1}{\gamma}\right)\right]} \tag{1}$$

Figure 2.1: Paschen curves for different gases.
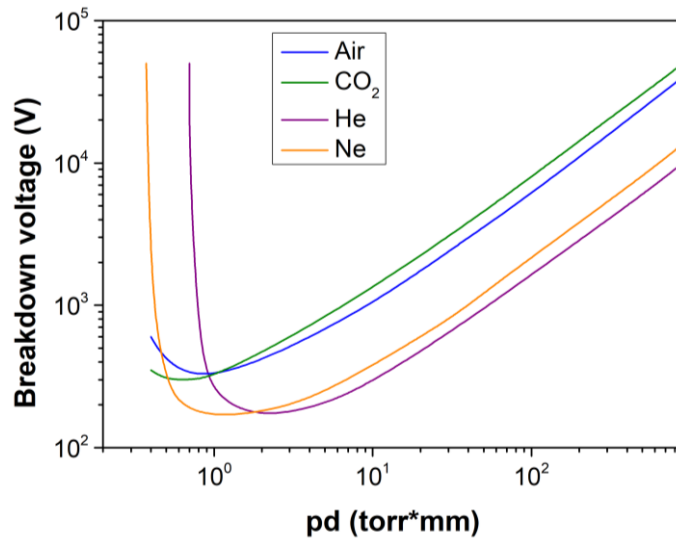
Source: Adapted from Merche, Vandencasteele, Reniers, (2012)

As can be observed from the Paschen curve in Figure 2.1 for different gases, there is a minimum breakdown voltage for generating discharge. The abrupt increase of breakdown voltage for lower *pd* values occurs due to small probability of collisions at low pressure (so-called vacuum insulation). On the other hand, for higher values of the product *pd*, the collision rate strongly increases and the particles quickly lose energy. Hence, at higher pressures higher voltage values are necessary to breakdown (NEHRA; KUMAR; DWIVEDI, 2008).

Another important process that occurs in plasmas is the excitation, where a bound electron is transferred to a more energetic state. In this reaction, the atom can be excited to a metastable state where the lifetime is longer than for radiative excited levels. Thus, the atom takes some time to deexcite (typically some µs) and during this can suffer other collisions. Thus, metastable atoms act as substantial energy storage reservoir within the plasma. Due to this, metastables are involved in another relevant charge carrier production process, the Penning ionization. It occurs when a metastable atom collides with neutral gas species ionizing it (OLDHAM, 2009).

The plasma properties can change according to the type of excitation source and amount of transferred energy applied. They can be produced in a wide range of pressure and temperature, where it is classified mainly according to the ionization degree (rate between the amount of charged and neutral particles in the medium) and temperature (NEHRA; KUMAR; DWIVEDI, 2008). Figure 2.2 presents different types of plasmas classified according to their electron temperature and density.

Figure 2.2: Clustering of different types of plasma according to the electron temperature and density.
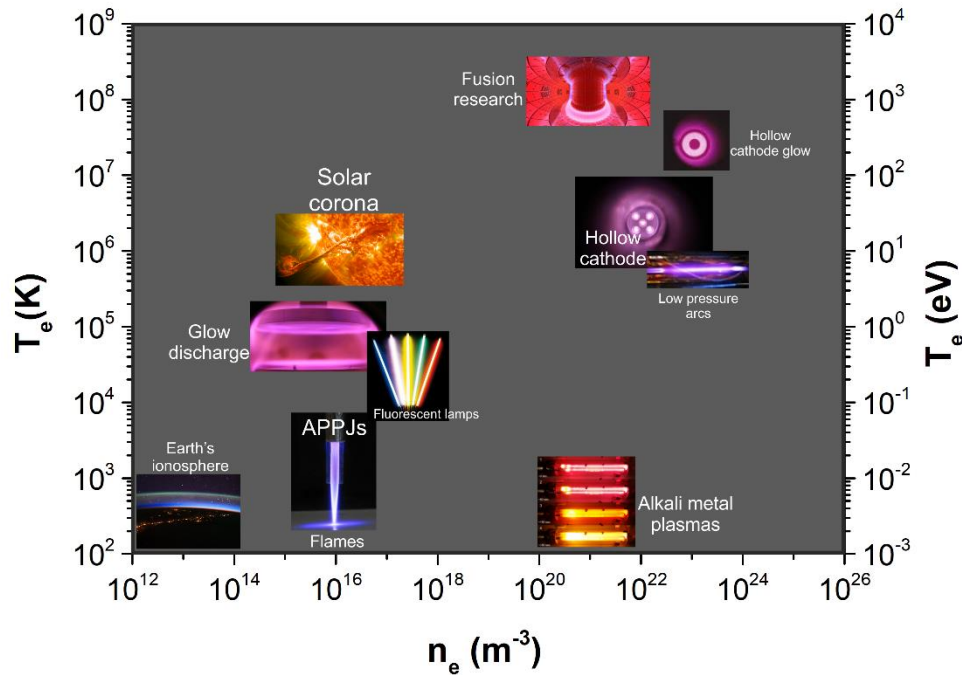
Source: Adapted from Harry (2010)

High temperature plasmas are characterized by presenting similar temperature for electrons and ions and a very high ionization degree, whereas for low temperature plasmas, electrons can present higher temperatures than the heavy particles exhibiting, in this case, a partially ionized medium. Table 2.1 summarizes the classification of plasmas according to their temperature.

Table 2.1: Plasma classification

	High temperature plasmas	Low temperature plasmas	
		Thermal	Non-thermal
Properties	$T_e \approx T_i \approx T_g$ $T_g = 10^6 - 10^8 K$ $n_e \geq 10^{20} m^{-3}$	$T_e \geq T_i \approx T_g$ $T_g \leq 10^4 K$ $n_e \geq 10^{20} m^{-3}$	$T_e \gg T_i \approx T_g$ $T_g = 300 - 10^3 K$ $n_e \approx 10^{13} m^{-3}$
Examples	Fusion plasmas	Arc discharges, plasma torch	Glow discharge, Corona discharge, DBD, APPJ.

Source: Adapted from Nehra; Kumar; Dwivedi (2008)

As can be observed in Table 2.1, the main classification of plasmas is given by the difference in temperature where they can be divided into high and low temperature discharges. However, low temperature plasmas can still be divided into thermal and non-thermal plasmas. Where for thermal plasmas, the electrons temperature can be slightly higher or equal to the heavy particles temperature, non-thermal plasmas show a big discrepancy between electron and ion temperature. In addition, thermal plasmas exhibit much higher ionization degree than the non-thermal discharges and thus, non-thermal plasmas usually operate at room temperature. In DC discharges, this difference in temperature can be easily changed by varying the system pressure as can be seen in Figure 2.3. For a weakly ionized gas in low pressure, the collision rate between electrons and heavy particles is insufficient to lead to thermal equilibrium. Thus, electrons and ions can present temperatures with up to two orders of magnitude difference, which is classified as non-thermal plasma (left hand side of Figure 2.3). However, when the pressure is increased, the collision rate rises and more effective energy transfer takes place leading to the thermal equilibrium among the plasma species (right hand side of Figure 2.3) (SCHÜTZE et al., 1998). Thus, plasmas generated at higher pressures are usually thermal discharges such as arc plasmas.

Figure 2.3: Behaviour of electrons and heavy particles temperatures as a function of the system pressure at constant current.
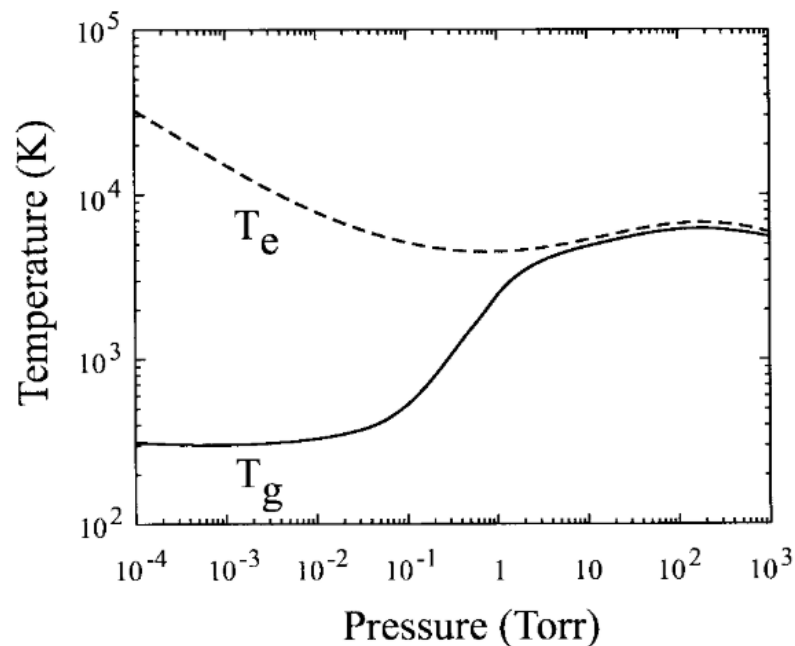
Source: Schütze et al. (1998)

2.2 ATMOSPHERIC PRESSURE PLASMAS (APP)

In the past years, low pressure plasmas have played a dominant role in the materials processing because of their large amount of chemically active species, low gas temperature, controllable particle fluxes and their high and uniform reaction rate capable of covering large areas (PARK et al., 2000). However, the biggest disadvantage of these plasmas is the presence of complex and expensive vacuum systems that limits the size of the target. Additionally, the time needed for the process is also increased due to the low-pressure conditions. In principle, atmospheric pressure plasmas can easily overcome the above-mentioned issues. However, for most of the applications, it is necessary to obtain a cold plasma at atmospheric pressure.

To better understand how to prevent discharge thermalization at atmospheric pressure, the different breakdown mechanisms need to be clarified. For a low-pressure DC discharge, the starting phase is defined by the Townsend mechanism already explained in section 2.1. However, for an atmospheric pressure plasma, the breakdown cannot be explained by means of the Townsend avalanche. At higher pressures, the ions have no time to reach the counter electrode, so the secondary electron emission process can be ignored. Besides, the photoemission mechanism is also not sufficiently fast (RAIZER, 1991). Thus, L. B. Loeb, J. M. Meek and H. Raether formulated a new streamer breakdown theory at around 1940 that can explain the discharge formation at atmospheric pressure (LOEB; MEEK, 1940a, LOEB; MEEK, 1940b, RAETHER, 1964). In such conditions, they observed that the discharge can propagate not only towards the anode but also towards the cathode. The streamers breakdown occurs when the so-called Meek criterion is satisfied. It relates the charge number density in the primary avalanche necessary to perturb the applied electric field (BRUGGEMAN; IZA; BRANDENBURG, 2017).

The theory is based on the formation of a thin ionized channel between the electrodes, called streamer. The process starts if the electric field is sufficiently high so that an electron avalanche can be initiated. The avalanche has a wedge shape rounded at the propagating head and according to Liu (2017), the electric field threshold at atmospheric pressure for starting is around 30 kV/cm. Electrons accumulate in the head front moving towards the anode creating a charge separation and producing a small local electric field. If it is not enough to distort the applied electric field between the electrodes, the avalanche propagates with the electrons drift velocity (RAIZER, 1991). In case secondary electrons are produced close to the avalanche head, its size increases in a way the space-charge electric field raises up to the order of the applied electric field (Meek criterion) and the avalanche can quickly grow into a streamer. This is

known as the streamer formation criterion and is given by Equation 2. Where the local electric field E'

$$E' = \frac{e^-}{R^2} e^{\alpha(E_0)x} \approx E_0 \tag{2}$$

is a function of the electron charge e^-, the avalanche head radius R and the number of ionizations per length of path α (first coefficient of Townsend). E_0 corresponds to the applied electric field.

Two different types of streamers with slightly different propagation mechanisms can be produced: the cathode-directed streamer and the anode-directed streamer. The growth mechanisms schemes are presented in Figure 2.4.

The cathode-directed streamers are those deriving from a normal electron avalanche propagating towards the cathode. Near the avalanche positive head, atoms can be excited creating energetic photons and producing photoionization in its vicinity (RAIZER, 1991). Thus, electrons produced by closeby photoionization processes initiate secondary avalanches that are pulled into the avalanche pathway due to the local electric field, where they merge to the primary avalanche ion tail creating a quasineutral plasma. However, the secondary avalanches can also excite atoms, where new photons are emitted creating secondary avalanche ions and enhancing the positive charge at the head of the primary avalanche, increasing the space-charge electric field (RAIZER, 1991). This increased local charge attracts electrons from new secondary avalanches repeating the process and allowing the streamer to grow until it reaches the cathode. The cathode-directed streamer growth mechanism is schematized in Figure 2.4 (a).

The anode-directed streamer will take place if formation criterion (Equation 2) is satisfied at a distance x (shorter than the gap) from the cathode. The propagation mechanism towards the cathode remains the same described above. However, for the streamer growing towards the anode, the electrons drift in the same direction as the streamer. As a result of photoionization processes, secondary avalanches are also produced in front of the negative head facing the anode. Due to the strong resulting electric field, the front electrons of the head quickly move forward, joining the ionic trail from the secondary avalanches and forming a quasineutral plasma channel (RAIZER, 1991). Figure 2.4 (b) schematized the growth mechanism of anode-directed streamers by photoionization processes. According to Raizer (1991), anode-directed streamers could also propagate without the photons production as an ionization wave. In this case, the negatively charged head would be accelerated by the strong electric field while the

electrons behind the front do not separate from the ions due to a weak field forming a quasineutral plasma trail.

Figure 2.4: Sketch of the propagation mechanisms of a (a) cathode-directed streamer and a (b) anode-directed streamer with secondary avalanches happening close to the streamer head and wavy arrows symbolizing emitted photons.

(a)   (b)
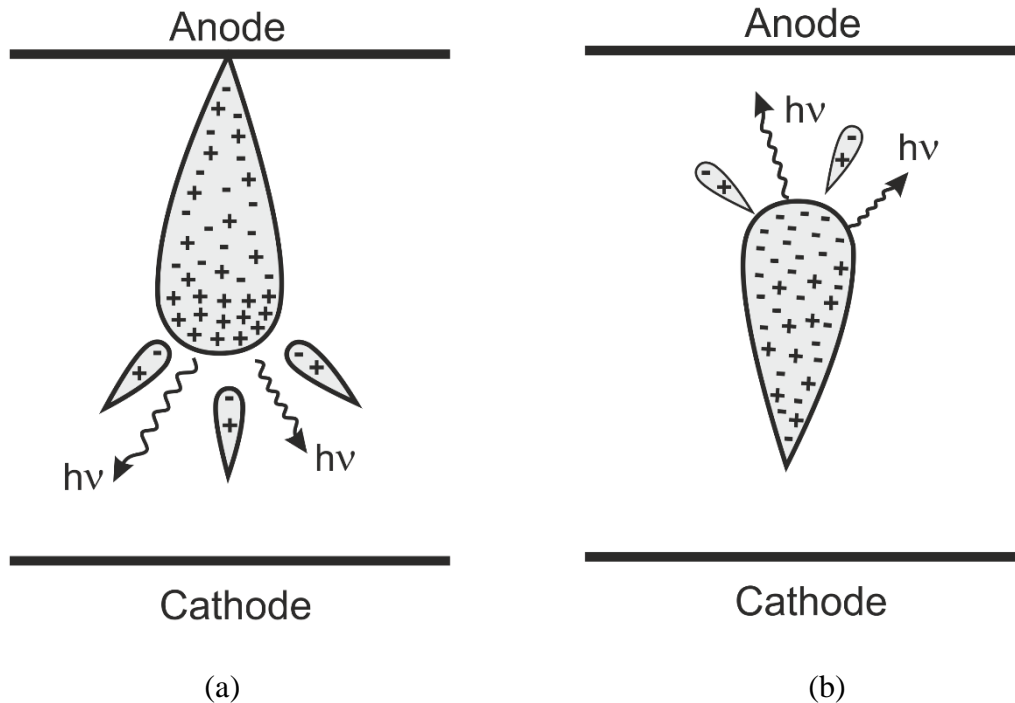
Source: Adapted from Raizer (1991)

Depending on the applied voltage and electrodes separation the streamer can develop into a spark or even to an arc discharge. These transitions are usually identified by a dramatic raise in current due to a rapid increase of ionization degree after the streamer closes the gap in the course of the spark breakdown. After connecting both electrodes, the ionization degree and temperature keep increasing until the spark channel enlarges due to a cylindrical shock wave produced. If the applied voltage is not controlled, the current keeps raising and an arc discharge can take place.

For some applications, the non-uniformity obtained in a discharge with streamers can be unfavorable. Besides, in case of treatment of heat sensitive material it is important to avoid the transition to arc discharge. In order to prevent it, some changes can be adopted in the system. The excitation frequency is important for obtaining cold plasmas. Non-thermal discharges are favored by AC or pulsed DC voltages with short pulses. Due to the higher mobility of electrons,

when AC voltage is used, they acquire energy in a shorter time period than the heavy particles. Thus, the ions keep a much lower temperature than the electrons (TENDERO et al., 2006). Small gaps can also help preventing the transition to thermal plasmas. The use of dielectric barrier covering the electrodes limits the discharge current, which also avoids the transition to arc discharge. When higher gas flow rates are used, the time that particles are present in the plasma core can be controlled. Also, it helps cooling the medium thus suppressing arc formation (BÁRDOS; BARÁNKOVÁ, 2010). The gas choice can also influence the obtained discharge, where helium, for instance, favors the generation of a glow-like discharge at atmospheric pressure. The electrodes shape also plays a role in this case. Sharp edges electrodes intensify the local electric field allowing a reduction of the applied voltage (SOUZA, 2012).

In order to efficiently suppress the formation of a non-uniform discharge or to prevent arc transition, combinations of several of the above-mentioned methods can be employed. Thus, among the possible configurations for generating a stable non-thermal plasma at atmospheric pressure, three of them are highlighted here: corona discharge, dielectric barrier discharge and plasma jets.

2.2.1 Corona Discharge

Corona discharge was the first systematically studied discharge at atmospheric pressure (NEHRA; KUMAR; DWIVEDI, 2008). It was first reported by sailors around the sharp edges of masts and was named St. Elmo's fire as it was seen as a sign from the patron saint of sailors, St. Elmo (LIU, 2017). Corona discharges occur only in strongly non-uniform electric fields produced by asymmetric electrodes (pin to plate configuration or combination of metal electrode and hollow cylinder). The discharge is generated in the region of the sharp electrode when DC or pulsed DC voltages are used. Once the electric field in the asymmetric electrode is highly non-uniform, the gas breakdown voltage is quickly achieved, and a weakly ionized discharge takes place around the electrode. The corona discharge can vary according to the sharp electrode polarity. For instance, more filamentary plasma is obtained if the sharp electrode is negatively charged, while if the electrode is positively charged, a more homogenous discharge can be obtained (CHANG; LAWLESS; YAMAMOTO, 1991). A pin to plate configuration for corona discharge generation is shown in Figure 2.5.

Figure 2.5: Typical pin-to-plate configuration of a corona discharge
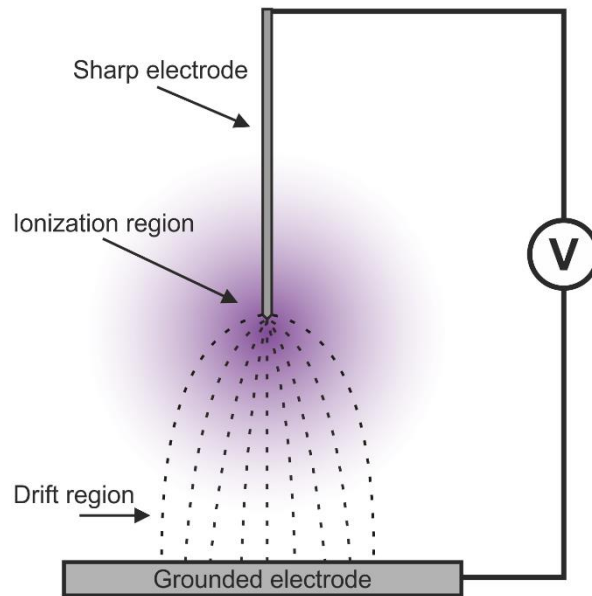
Source: Author's illustration

Glow corona can be produced in energy towers, transmission lines, lightning rods and electric circuits, and in those cases, it is undesirable since it causes energy loss, audible noise and insulating damage (LIU, 2017). Corona discharges have found suitable applications in electrostatic precipitators (MILDE, 1982), ozone generators (HONG; OH; MOON, 2003) and water purification systems (MALIK; GHAFFAR; MALIK, 2001). However, the small region of plasma formation can limit its application in the field of material processing. To avoid problems with non-homogeneity and small plasma zone, the dielectric barrier discharge (DBD) can be used.

2.2.2 Dielectric Barrier Discharge (DBD)

Dielectric barrier discharge is an electric discharge that occurs in the gap between two electrodes, where at least one of them is covered by a dielectric material. When produced at atmospheric pressure, the distance between electrodes must be reduced to few millimeters as shown by the Paschen curve in Figure 2.1. The use of dielectric barrier helps limiting the current avoiding the arc formation, but also prevents the operation with DC voltage. Usually, DBD devices are operated with high AC voltages in the frequency range of 0.05 to 500 kHz and pulsed voltages (FRIDMAN, 2008).

There is a great flexibility regarding the geometrical shape of DBD reactors, the feeding gas composition and operational parameters such as input power, frequency, pressure and gas flow (KOGELSCHATZ, 2003; WAGNER et al., 2003). Thus, with optimized parameters, DBDs can be easily upscaled for industrial treatments. Usually, dielectric materials such as glass, quartz, ceramics, Teflon, rubber or silicon are used. The geometry can be adjusted according to the desired application as shown by Brandenburg (2018). The typical and basic experimental arrangements of a dielectric barrier discharge reactor are presented in Figure 2.6. The most common geometries are plane and cylindrical where a discharge is produced in the gap between electrodes. The presence of one or two dielectric barriers in the gap can play an important role in the plasma production and on its parameters. In Figure 2.6 (a1 and b1) two dielectric barriers are used to cover both electrodes, protecting them from the reactive species that might be generated in the discharge. In the case of Figure 2.6 (a2,3 and b2,3) one or both electrodes are exposed to the discharge which might lead to its corrosion or erosion. However, having at least one bare electrode helps reducing the applied voltage amplitude (BRANDENBURG, 2018). Besides the configurations presented by a and b in Figure 2.6, surface DBD discharges can be obtained by utilizing the structures c1 and c2, surface discharge and coplanar configuration respectively.

The dielectric barrier discharge can operate mainly in two regimes: filamentary and diffuse modes. The filamentary regime is the classical operation mode of a DBD. When operated in the kHz range of frequency, the electrical breakdown leads to charging of the dielectric surface. The surface charges produce local electric field opposite to the applied one, decreasing the total electric field and extinguishing the discharge. However, upon inversing the electric field, the accumulated surface charges on the dielectric helps igniting the discharge. Those local discharge channels formed by charge accumulation on the insulator surface are streamers, in this case also called microdischarges or filaments. The microdischarges are randomly distributed on the insulating surface and occur when the applied electric field exceeds the gas breakdown (FANG et al., 2009, KOGELSCHATZ; ELIASSON; EGLI, 1997). Increasing the voltage amplitude leads to generation of a higher number of microdischarges but does not change the amount of transferred charge by a single filament (BRANDENBURG, 2018). The microdischarges have a short duration of about 10-100 ns and depend on the pressure, gas type and reactor parameters, such as the gap. Filamentary plasmas are usually produced in molecular gases, argon or mixtures of noble and molecular gases. It can be easily identified visually but also exhibits multiple current spikes that occur in both positive and negative cycle of the voltage.

Figure 2.6: Typical DBD configurations with different electrode's arrangements.

Planar DBD Electrode Arrangements

Cylindrical DBD Electrode Arrangement

Surface Discharge　　　　**Coplanar Discharge**
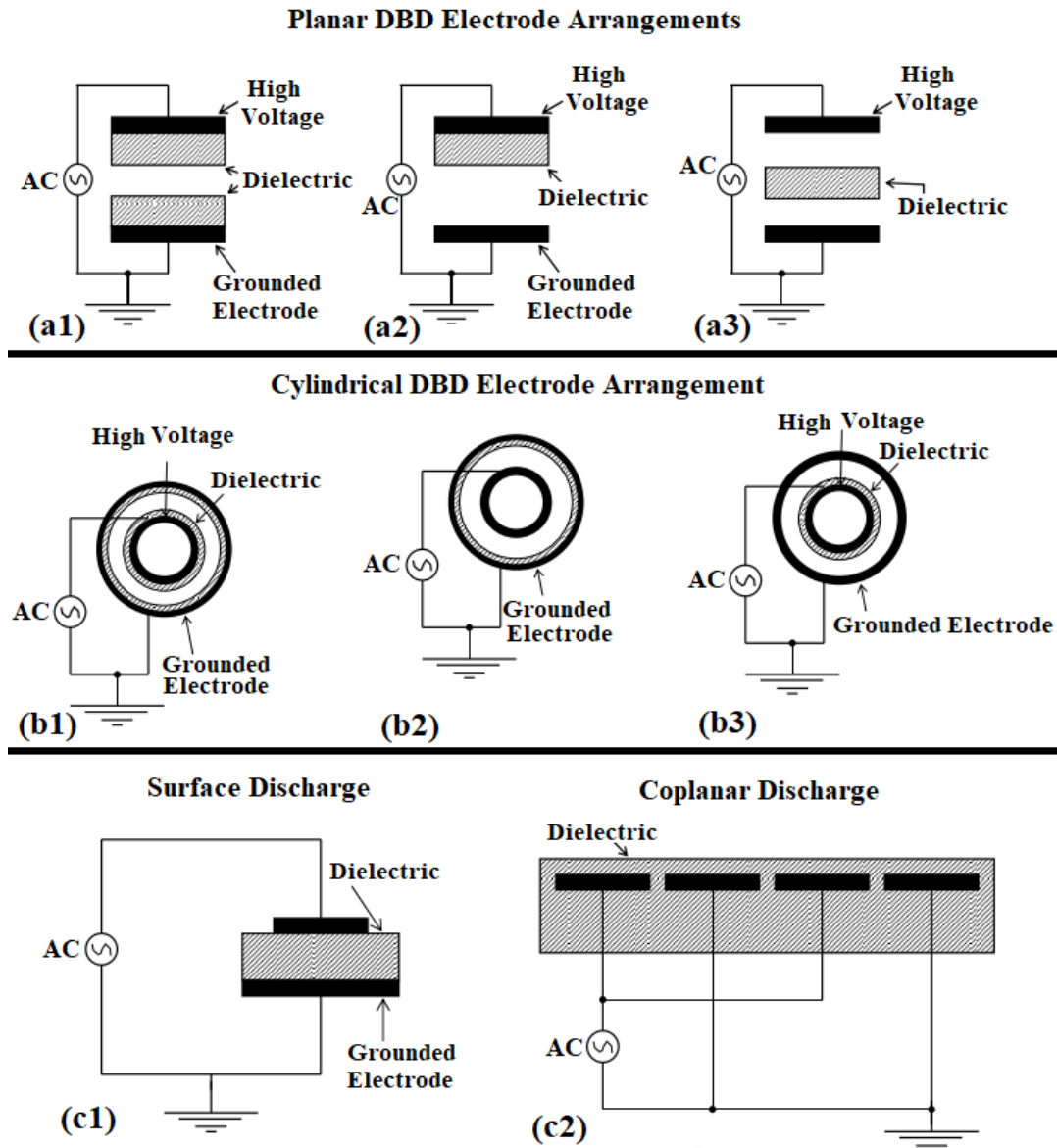
Source: Adapted from Nehra, Kumar and Dwivedi (2008)

The diffuse discharge regime, also called atmospheric pressure glow discharge, requires very specific operation conditions and is characterized by the absence of microdischarges. It can be obtained by external pre-ionization of the gas or by selecting the gas composition and purity (BRANDENBURG, 2018). This discharge mode presents current signal with a single broad current pulse and is typically observed in pure gases such as helium, neon and nitrogen. Changes in the electrode's configuration or even slight voltage variations can lead to a transition from the diffuse mode to a filamentary regime (FANG et al., 2007).

Dielectric barrier discharges can generate a wide and uniform volume of plasma and have a relatively simple configuration. Thus, DBDs are employed for several applications such as

ozone generation (PARK et al., 2006), ultraviolet radiation (UV) source (EL-DAKROURI et al., 2002), decontamination of polluted gases and liquid treatment (ALVA R. et al., 2015; GRINEVICH et al., 2011), surface treatment and deposition (KONG et al., 2018), treatment of seeds (ZAHORANOVÁ et al., 2016) and biomedical applications (DAESCHLEIN et al., 2012). However, one disadvantage of DBDs is the limitation concerning the treated sample size. Since the gap cannot exceed few centimeters and the discharge is only produced inside this region, treatment of irregular or big samples is difficult. It can be performed by indirect methods but in such cases, short-living species such as atomic oxygen and charged particles vanish before reaching the sample (LU; LAROUSSI; PUECH, 2012). Thus, depending on the target, having the plasma extracted outside the electrode's region can be appropriate.

2.2.3 Atmospheric Pressure Plasma jet (APPJ)

Plasma jet is a device capable of generating plasma plumes in open space. The discharge is generated in the region between electrodes and then, by means of the gas flow and the electric field, it is extended as an effluent into the surrounding ambient. It has a great flexibility concerning the electrodes configuration. Basically, a plasma jet comprises of arrangement of corona discharge, DBD or other non-equilibrium atmospheric pressure plasma configuration. Once the plasma is extracted from the electrode's region, it can be easily directed to treat irregular surfaces and big samples. Figure 2.7 presents a schematic setup of a plasma jet with DBD configuration. The choice of electrode's arrangement influences the final plasma plume. Lu, Laroussi and Puech (2012) summarized the main plasma jet configurations and their characteristics. DBD and DBD-like plasma jets are obtained when at least one insulator material is used to cover the electrode. In general, DBD plasma jets have low power and, therefore, a lower temperature, unlike corona type plasma jets in which the power can reach higher values due to the bare electrode. Thus, DBD jets are usually suitable for biomedical applications and treatment of heat sensitive targets. The electrode's shape can vary substantially. The two most common configurations are ring- and rod-shaped electrodes, where the rod electrode enhances the electric field along the central axis and enables the formation of longer plasma plumes. Studies have shown that stronger electric fields in the plume region lead to more active plasma chemistry (WALSH; KONG, 2008).

Figure 2.7: Sketch of a plasma jet with DBD configuration.
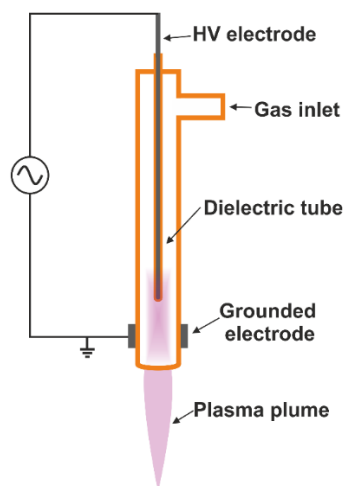
Source: Author's illustration

Unlike the corona and DBD discharges, plasma jets require the use of gas flow (usually several slm). On the one hand, it contributes to cooling down the discharge and enhances the transport of plasma species away from the discharge gap. However, it adds one more parameter that affects the overall performance of the plasma source. For corona discharges and DBDs, the reactor can be sealed and only predicted plasma species from the used gas are generated. In the case of a plasma jet, after the plume is blown outside the device, it interacts with the surrounding air generating new plasma species such as reactive oxygen and nitrogen species (RONS) (LU; LAROUSSI; PUECH, 2012). This transporting of plasma particles and generation of air-based reactive species makes the plasma jet effluent a highly reactive zone. However, the weather conditions like humidity can directly affect the air-species influx at the plasma plume, influencing the reproducibility of the treatments. Thus, the usage of plasma jets in climate-controlled environments can be necessary. An alternative would be the use of chambers with synthetic air atmosphere. Reuter and coauthors (2012) studied the control of effluent species composition by creating a shielding gas around the plasma plume. This gas curtain shields the formed plasma jet from the ambient air and provides the necessary composition to produce the desired reactive species.

Within the last 15 years, studies have shown that APPJs working with noble gases are not exactly formed by a continuous plasma column extracted from the gap but are composed of small plasma volumes propagating with high velocity called plasma bullets.

2.2.3.1 Plasma bullets

In 2005, Teschke and coauthors observed for the first time the propagation of plasma bullets in a helium APPJ driven by AC voltage in the kHz range. By means of ICCD pictures, the group showed that plasma jets are in fact composed of plasma bullets propagating outwards the HV electrode region with velocities of around 15 km/s (TESCHKE et al., 2005). Since then, experimental and numerical simulation investigations have been carried out to deeply understand this phenomenon. According to Lu and coauthors (2014), the dynamics of plasma bullets comprises of 1) ionization wave formation inside the tube moving along the dielectric surface similarly to streamers and 2) propagation of the plasma bullets inside the plume region in a mixture of noble gas and ambient air. Thus, the bullet-like volumes move along predefined paths like guided ionization waves (LU et al., 2014). Inside the dielectric tube, the electrons drifting from the HV electrode and charge accumulated on the dielectric wall produce parallel electric field which sustains the surface ionization wave along the tube (REUTER et al., 2012). This conductive channel produced inside the dielectric tube creates a path for the ionization wave, helping its propagation.

The propagation mechanism of plasma bullets is similar to that of streamers. However, in the case of APPJs, the bullets propagate in strongly non-uniform media due to the mixing of the gas with the surrounding air and thus, the plasma bullet shape can differ from that of a streamer in free space (LU et al., 2014). In addition, differently from streamers that initiate in a stochastic manner, plasma bullets are mostly very repeatable and always appear in the rising slope of the applying voltage (LU; LAROUSSI; PUECH, 2012, TESCHKE et al., 2005). After the breakdown, the streamer propagates via photoionization processes that ionize the front of the bullet head. The produced electrons neutralize the previous positive front, leaving a new positive head slightly further but also excite species leading to emission of new photons. These will start new photoionization processes and the plasma bullet propagates forward. A schematic diagram of the propagation of plasma bullets is presented in Figure 2.8.

Figure 2.8: Plasma bullets propagation mechanism by photoionization process.
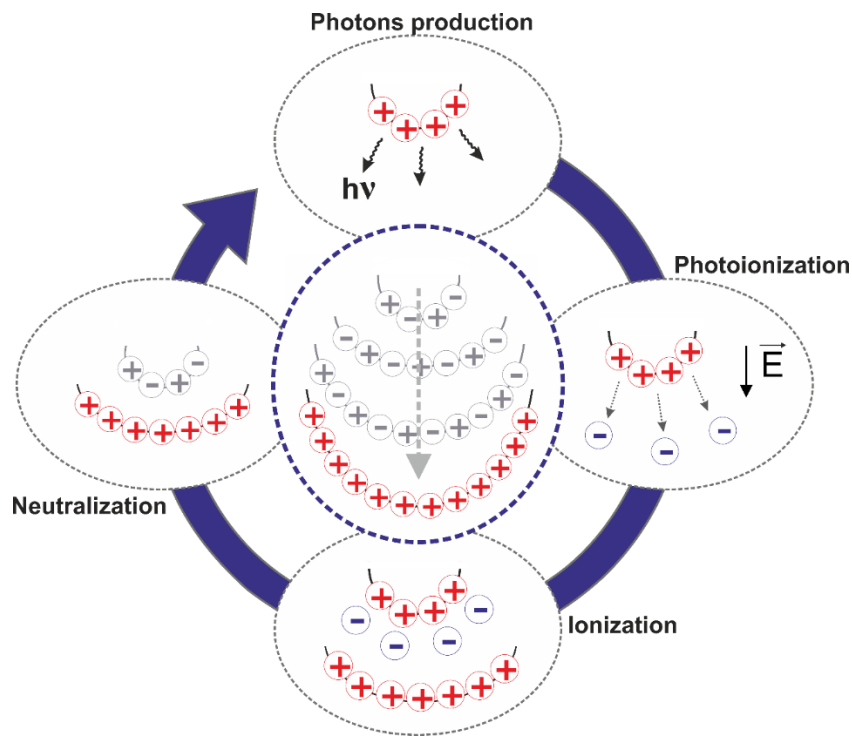
Several investigations have shown that plasma bullets present a hollow (donut-like) shape (CHANG et al., 2014, CHANG et al., 2018, LU; LAROUSSI; PUECH, 2012). Chang and coauthors (2018) concluded that Penning ionization plays an important role in maintaining the donut-shape structure of the plasma bullet since it provides abundant seed electrons in the plasma plume boundaries with ambient air. Thus, it facilitates the discharge to happen predominantly in this region. However, it was demonstrated that Penning ionization has no effect in forming the hollow structure of plasma bullets (CHANG et al., 2018). It is mainly resulted from guided laminar gas flow that allows the discharge propagation along the inner wall surface and from photoionization processes at the head of the plasma bullet (CHANG et al., 2018, MERICAM-BOURDET et al., 2009).

2.3 DISCHARGE CHARACTERIZATION

Cold atmospheric pressure plasmas have gained much interest over the last decades. Due to its convenient generation in ambient environments and the lack of expensive vacuum systems, APP has been widely employed in many applications, since materials science to

biomedical purposes. Depending on the kind of application, the generated plasma needs to fulfill some criterion. Restrictions concerning gas temperature, transferred energy (mean power) and produced reactive species play important role in the development of specific plasma sources. Therefore, discharge characterization is of major importance in the investigation for possible future applications

2.3.1 Electrical characterization

The proper discharge characterization is very important for the understanding of the plasma effects. The measurement of different discharge characteristics, such as the mean discharge power, voltage, frequency, transferred charge and current is essential for assigning the proper discharge application.

2.3.1.1 AC power supply

When operating the discharge with a simple AC power supply, transferred charge and discharge current can be easily obtained by connecting a capacitor or a low inductance resistor, respectively, in series with the discharge cell, as schematized in Figure 2.9. The voltage $V_{r,c}$ across the components is directly related to the charge (for the capacitor) and current (for the resistor) of the discharge.

However, this circuit requires the use of grounded electrodes. For current measurements it is possible to overcome this with a Rogowski coil. This device makes possible the measurement of alternating and high-speed impulse currents in wires based on Faraday's laws. It consists of a toroidal coil and, in some configurations, the winding wire can be returned to the starting position through the central axis of the formed loop, providing an easy manipulation. When a wire is passed through this coil, a voltage is induced on it due to its interaction with the magnetic field from the variable current in the wire. This voltage signal is proportional to the current derivative and can be integrated for the whole coil to provide the actual current passing through it.

Figure 2.9: Experimental setup used for measurement of discharge current and transferred charge of plasma jets.
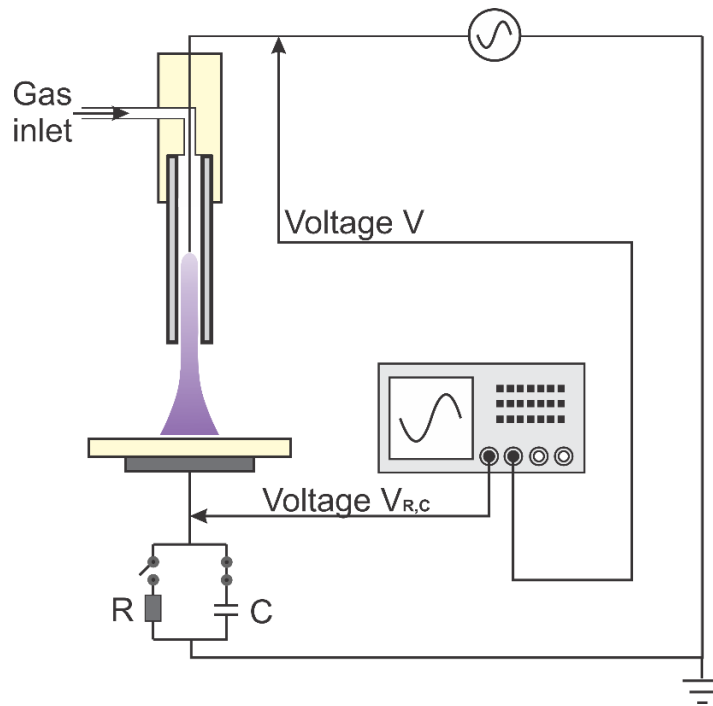
Source: Adapted from Nishime (2015)

The discharge current signal shape will differ according to the type of discharge. Filamentous discharges in AC excited plasmas present several short current peaks randomly distributed in the rising and falling voltage regions. On the other hand, glow discharges can present well determined larger current peaks corresponding to the discharge ignition (increase in electrons generation) that always appear in the same voltage half-cycle position. Hence, the energy consumed per cycle U_c can be obtained by simply integrating the voltage and current signals as follow (JIANG et al., 2013):

$$U_c = \int_0^T v(t)i(t)dt = \sum_{i=0}^{M} V_i I_i \Delta t \tag{3}$$

Where V_i and I_i are the measured values for voltage and current at the recording point I, M is the length of recorded data and Δt is the sample interval.

Another common approach for obtaining the mean discharge power is the Lissajous figure method. The Lissajous figure is the pattern created by the superposition of two sinusoidal signals when their axes are perpendicular to each other (*X-Y* plot). If those signals are phase shifted, then the formed pattern is an ellipse whose eccentricity is related to the phase

difference. In electric discharges excited by sinusoidal voltages, the Lissajous method can be applied for obtaining the discharge power when the voltage and charge are plotted together for one period T. The energy per voltage cycle (M points separated by the time interval Δt) is then given by:

$$U_c = \int_0^T Q\,dV = \frac{1}{M}\sum_{i=1}^M Q_i.\Delta V_i \tag{4}$$

Therefore, the discharge energy can be acquired by evaluating the area of the Lissajous figure and the power calculated by:

$$P = \frac{U_c}{T} = \int U_c \tag{5}$$

This method is very efficient for measuring the power of discharges with noisy current, such as corona or filamentary DBD discharge (BURÁNY; HUBER; PEJOVÍC, 2008), since it integrates the high-frequency current pulses. But can be applied only if the Q-V signal forms a closed figure. In other words, it works only if the Q-V figure is effectively a Lissajous figure.

Figure 2.10: Simplified representation of typical Q-V Lissajous figures for (a) capacitive and (b) resistive discharges.

(a)   (b)
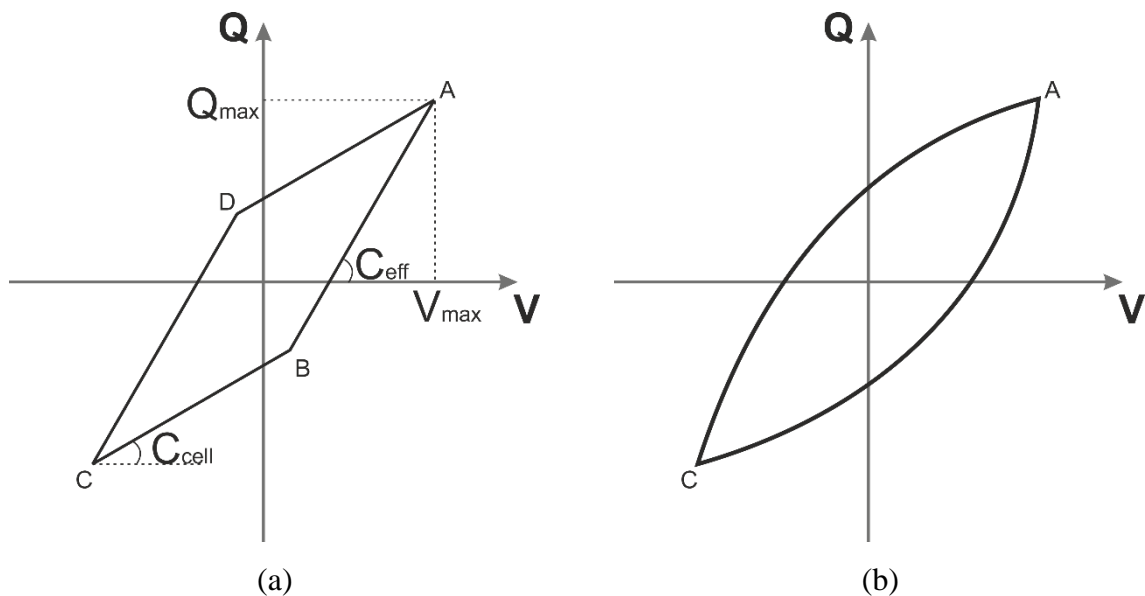
Source: Author's illustration

The Q-V Lissajous figure shape carries important information about the discharge nature (KOGELSCHATZ, 2003). Capacitive discharges, such as DBDs, present a typical parallelogram shape, as shown in Figure 2.10 (a). Lines BC and DA indicate the discharge-off phase, where only the displacement current takes place, and their slopes correspond to the capacitance of the dielectrics C_{cell}. When the voltage breakdown is reached, the discharge-on phase starts and it is represented by the lines AB and CD. The slope of those lines provide the effective capacitance C_{eff} (KOGELSCHATZ, 2003, MEI et al., 2014). On the other hand, corona discharges present a resistive load that turns the Q-V Lissajous figure shape into an almond-like contour (KOGELSCHATZ, 2003, ZHANG; CHA, 2013), as schematized in Figure 2.10 (b).

2.3.1.2 Operation in burst mode

Operating the power supply in burst mode allows a precise tuning of the discharge power. This mode consists of a period of high voltage oscillations followed by a voltage off interval, similar to a pulsed signal. The voltage waveform in burst mode for the employed power supply is shown in Figure 2.11. When connected to the plasma source, discharge is generated in the burst regions and extinguished during the breaks, as assigned in the image. Each burst contains a certain number N of sinusoidal oscillation cycles with similar amplitude and terminates with an exponentially decaying oscillation. In this mode, it is possible to control the repetition period T_r (i.e., the time interval for repetition of the HV bursts) that allows the adjustment of plasma off time. The interval Δt pointed in Figure 2.11 corresponds to the period of burst that is given by $\Delta t = \frac{N}{f}$, where f is the frequency and changing N adjusts the period of plasma on. Usually those parameters can be combined and expressed as duty cycle D that is defined as follows:

$$D = \frac{\Delta t}{T_r} = \frac{N}{fT_r} \tag{6}$$

Figure 2.11: Waveform of modulated voltage signal for a frequency of 32 kHz. T_r is the burst repetition period and Δt is the duration of a group of HV oscillations.
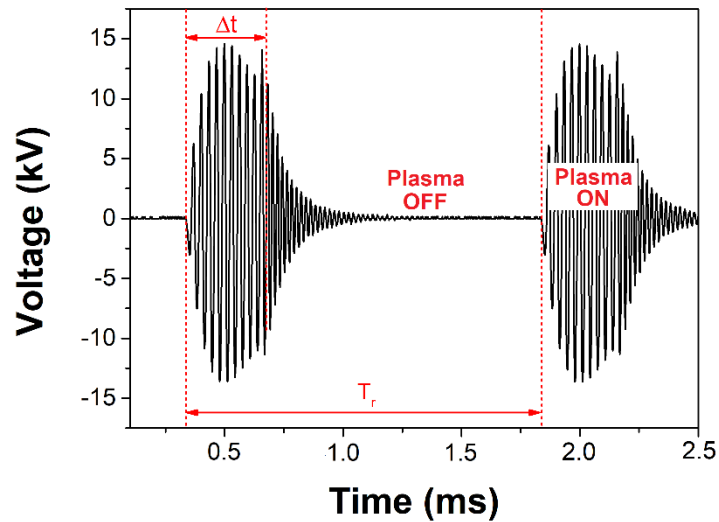
Source: Author's illustration

Therefore, the mean power of a plasma source driven by such burst mode can be calculated by the following expression:

$$P = DfU_c = \frac{U_c N}{T_r} \qquad (7)$$

Where U_c is the energy per cycle of voltage oscillation obtained by the Lissajous figure method.

2.3.2 Optical Emission Spectroscopy (OES)

Optical emission spectroscopy is a very popular technique for plasma diagnostics. The main advantage of this tool is to allow investigation of reactive discharges without physical contact with it. This technique detects emissions of interest from the plasma that originates from electronically excited states. Thus, the emission intensities are proportional to the density of the excited species. However, the electron energy distribution function of the discharge determines the fraction of plasma species that are excited into optically emitting excited state. Therefore, the intensity detected by the optical emission spectrometer is influenced not just by the density of the plasma species involved but also by the electron energy distribution function (COBURN; CHEN, 1980). Thus, the intensity values obtained cannot be directly related to the density of

plasma species but is an indication of its presence in the discharge. Additionally, OES can be used to determine some physical parameters of discharges such as electron and ions density and temperatures (vibrational, rotational and kinetic) (LAUX et al., 2003).

The analysis is performed by means of the emitted radiation from each energy level corresponding to the excitation of atoms and molecules caused by their collision with other particles. The reached excited state is unstable and the particle quickly loses energy by colliding or emitting radiation, turning to its ground state. The radiation wavelength is particular for each excited specie. Thus, it is possible to investigate the excited species in the plasma by analyzing its spectrum.

2.3.3 Temperature measurements

Different temperatures can be evaluated for non-thermal plasmas. The electron temperature, that is much higher than the ion temperature due to the non-local thermodynamic equilibrium (non-LTE) condition, is important for the discharge characteristics evaluation, such as calculation of electrons density. According to Chang and coauthors (2012), the electrons temperature in non-LTE condition can be deduced from the approximation of ions number balance and the electron energy distribution function (EEDF). However, when it comes to plasma application, the heavy particles and their temperature plays direct and important role. Depending on the desired application, limiting the gas temperature can be crucial, for example when dealing with temperature sensitive targets like polymeric materials, plants and seeds, cells and living tissues.

The gas temperature can be measured by different techniques. However, most of the methods include conductive materials that disturb the discharge. One common non-invasive method is by means of optical emission spectroscopy, were the gas temperature can be derived from molecular bands emission (BRUGGEMAN et al., 2009). In this approach, for processes that ionize air, roto-vibrational bands of N_2 or OH are typically fitted in order to obtain the gas temperature, which is represented by the molecular rotational temperature (CHANG et al., 2012, GARG et al., 2008, SARANI; NIKIFOROV; LEYS, 2010). Although OES can provide a good estimation of the gas temperature, the post processing analysis can be arduous depending on the spectrometer resolution. Therefore, fibre optical thermometers (FOTs) are excellent alternatives once their non-conductive coating and the low heat capacity allows minimal discharges disturbance and precise temperature measurements (± 0.2 ℃) in a short period of time (≤ 2.0 s).

FOT is a system that relies on the temperature dependence of a semiconductor band gap, such as gallium arsenide (GaAs), to preform temperature acquisition. It is composed of a Teflon-coated optical fibre connected to a spectral detection unit and a semiconductor crystal located at the fibre tip end. The detector records the photon energy sufficient to promote a valence electron to the conduction band of the semiconductor. This necessary energy to excite the electron is the so-called bandgap energy (U_{gap}) and, for the GaAs crystal case, it has a temperature dependence behaviour as follows (ROLAND et al., 2003):

$$\frac{dU_{gap}}{dT} = -0.452 \frac{meV}{K} \ at \ 300 \ K \tag{8}$$

When the GaAs crystal is placed in a zone of unknown temperature a characteristic curve is generated and the curve edge varies according to the medium temperature. Finally, the probe provides a voltage signal proportional to the temperature.

2.4 ATMOSPHERIC PRESSURE PLASMA APPLICATIONS

2.4.1 Decontamination

Decontamination is considered a process of removal or inhibition of microorganisms. In this attempt to destroy microbes, some different methods such as physical or chemical procedures can be employed (ROCHA, 2009). However, with the worldwide growing antimicrobial resistance of bacterial pathogens, new treatment alternatives have emerged (FRIERI; KUMAR; BOUTIN, 2017). Within past few years, it was observed that atmospheric pressure plasmas present antimicrobial characteristics. Cold plasmas can be employed for decontamination and sterilization of surfaces, heat-sensitive instruments, plastic items, air, water and also the skin. Even though it is known that the plasma components (UV radiation, electric field, charged particles, reactive species) individually can sterilize, the exact mechanisms that lead to microbial inactivation are not precisely understood yet. However, a synergetic effect of all plasma components is considered the key of atmospheric pressure plasmas decontamination effect (FRIDMAN; FRIEDMAN, 2013, KLÄMPFL, 2014, LACKMANN; BANDOW, 2014, ZHOU et al., 2016).

Taking into account the effects of the plasma components separately, Stoffels (2007) observed that the charge accumulation in microorganisms can lead to cell disruption. Reactive

oxygen species such as O and O_3 damage the macromolecules present in the cell membrane (SOUZA, 2012). Several authors investigated the increased microbicide effect of plasma when oxygen is added to the feed gas (ABOUBAKR et al., 2018, LACKMANN et al., 2013, LU et al., 2016). The production of reactive oxygen species (ROS) can be enhanced by the increase of gas humidity that leads to formation of OH radicals by the dissociation of water molecule. The reactive nitrogen species NO_x are also very important for decontamination effects and can be easily obtained by generating plasma in air (SOUZA, 2012). Lackmann and Bandow (2014) showed that some chemical species and (V)UV photons can cause damage to the membrane, nucleic acids and protein. However, UV has not been considered as the major responsible for antimicrobial effects of a plasma jet, since most of the produced radiation is absorbed by the ambient air and only the intensity of UV radiation that reaches the target is very low (LU et al., 2008). Thus, when all plasma components effects act simultaneously, a better and more effective response can be expected.

2.4.2 Material treatment

For decades, plasmas have been employed in the materials processing such as surface etching, thin films deposition and implantation (LIEBERMAN; LICHTENBERG, 2005). In general, those processes were carried out in vacuum chambers. Recently, with the extensive research efforts, atmospheric pressure plasmas became a promising candidate for material surface treatment. In particular, plasma jets allow the treatment of irregular surfaces with no limitations concerning size or shape and have the ability of generating a high flux of reactive species (PENKOV, 2015).

Polymers generally have a low surface energy that leads to poor adhesion properties, wettability and dyeability. Thus, APPs have been used to overcome those problems since they can provide uniform surface treatment with modification depth of less than 10 nm (DOWLING et al., 2011). Some electrons from atmospheric pressure plasmas have enough energy to cause molecular dissociation and atomic excitation from polymer molecules (BORCIA; ANDERSON; BROWN, 2004; SANTOS 2010). Thus, energetic particles and photons from the discharge strongly interact with the polymer surface via free radical chemistry. Four major effects can be observed after plasma treatment: surface cleaning, ablation or etching, cross-linking at the surface and surface chemical structure modification (SHISHOO, 2007). Which one will be dominant depends on the substrate, gas chemistry, reactor and operation conditions.

Plasma treatment can be used to enhance the bond strength in the interface between two different materials, for instance polymer-fiber combination. Thus, the treatment can lead to incorporation of new polar groups at the polymer surface increasing the wettability and modifying the surface chemistry. The modified surface chemistry facilitates reactions with the adhesive layer, forming covalent bonds in the materials interface (SHISHOO, 2007).

3 MATERIALS AND METHODS

3.1 EXTENDED AND FLEXIBLE DBD PLASMA JETS

The present work aims for the study of two different DBD plasma jet devices: the plasma endoscope from the Leibniz Institute for Plasma Science and Technology (INP), Greifswald, Germany and the long tube plasma jet developed at the São Paulo State University (Unesp), Guaratinguetá, Brazil. Although both plasma jets have some similarities, such as their elongated configuration and kind of discharge, they were designed for specific and distinct applications and therefore, they are presented separately in the following sections.

3.1.1 Plasma endoscope (INP)

The plasma jet developed at the INP for endoscopic applications is schematically presented in Figure 3.1. It consists of two concentrically placed polytetrafluoroethylene (PTFE) tubes that are fixed together with a 3D-printed ceramic (99.99% Al_2O_3) nozzle. Given the desired endoscopic application of this plasma jet, the device dimensions must be assuredly reduced. The centermost tube has an inner and outer diameters of 0.9 mm and 1.2 mm, respectively and the outer tube, held in place by the ceramic tip grooves, has inner and outer diameters of 1.5 and 1.8 mm, respectively. This double tube configuration allows the introduction of two different gases, a working gas in the inner tube and the shielding gas in the surrounding one. The use of a shielding gas around the main gas stream provides a new environment in the plasma jet surroundings allowing its operation inside closed cavities. The inner channel of the ceramic nozzle is around 0.4 ± 0.1-mm-diameter. As a result of the small size, the applied gas flows must be in the range of hundreds standard cubic centimeter per minute (sccm).

A 100-µm-diameter copper wire is wrapped around the entirely outer part of the centermost tube and serves as high-voltage (HV) electrode. In order to avoid generation of plasma along the tube due to a local significant electric field, the metal winding spacing is made very narrow, around 80 µm. The electrode tip end is twisted around the ceramic head 1 mm before the thick nozzle region. This ending is fixed and protected with epoxy glue. The tubes lengths can be made as long as necessary once the HV electrode covers the entire range. In the present work, the total length was around 40 cm. The spiral electrode was connected to an AC HV power supply developed at the INP capable of providing amplitudes up to 4.6 kV at a

frequency of 14.2 kHz. The experimental setup is presented in Figure 3.2 together with the schemes of different analysis performed. Primarily, the plasma source was fed with helium and air as a feed and shielding gas, respectively. Air was primarily chosen to provide similar working environment as an open condition. Lately, the plasma jet performance operating with neon as alternative main stream and CO_2 as shielding gas was also investigated. The gas flow rates were varied from 0 to 350 sccm for the shielding gas and from 0 to 550 sccm for the feed gas.

Figure 3.1: Plasma endoscope (a) scheme and (b) picture with dimensions
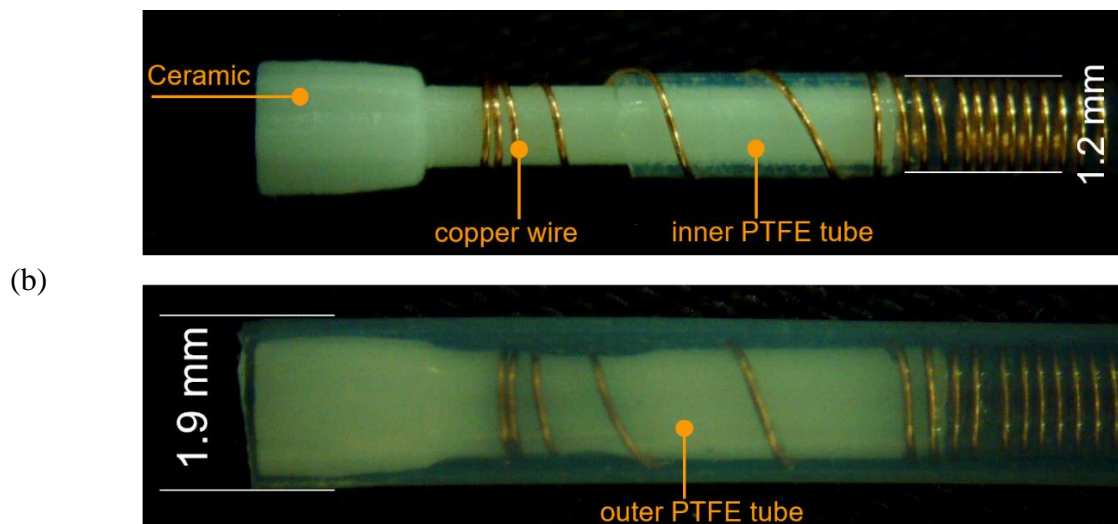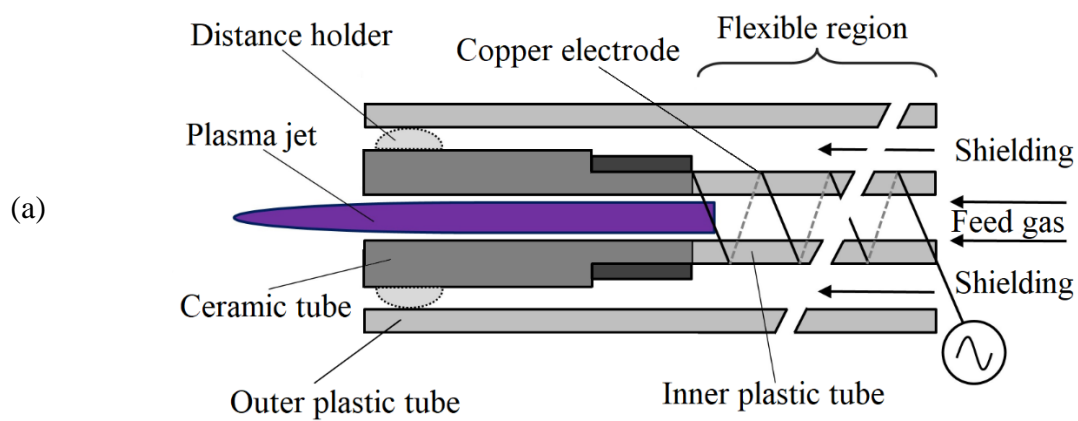
Source: Adapted from Winter et al. (2018)

Figure 3.2: Experimental setup of the plasma endoscope for power and gas temperature measurements. The scheme shows how the optical emission spectra was acquired. C represents the capacitor used for power acquisition.
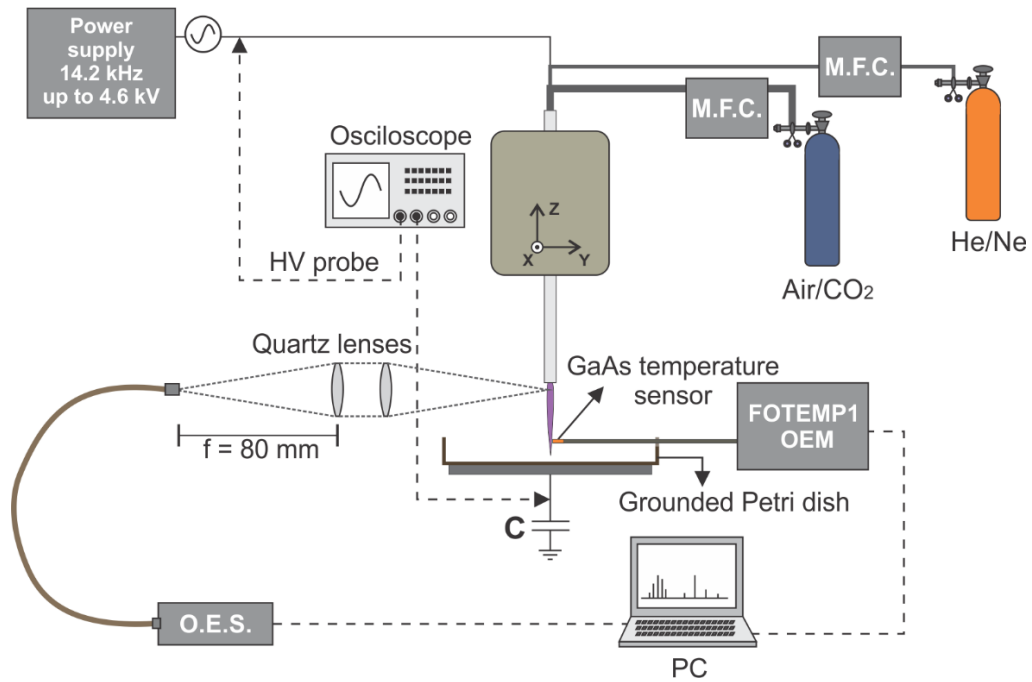
Source: Adapted from Winter et al. (2018)

3.1.2 Long tube plasma jet (Unesp)

The long tube plasma jet was developed at the São Paulo State University (Unesp) and consists of a flexible plastic tube attached to a primary DBD reactor. Inside this tube is placed a thin metal wire at floating potential that penetrates few mm in the primary discharge, as shown in Figure 3.3. The other wire termination finishes around 2 mm before the tube tip end, where a plasma jet can be ignited. The elongation component can be connected to two different primary reactors configurations: parallel plates and pin electrode.

Figure 3.3: Connection scheme of the long plastic tube with metal wire. Attachment example for the pin electrode configuration.
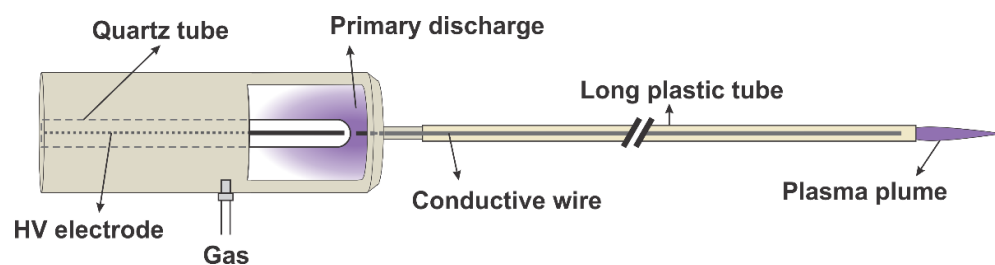
Source: Kostov et al. (2015a)

3.1.2.1 Parallel plates configuration

The first primary reactor consists of an enclosure made of polyoxymethylene Delrin® with two parallel metal disks serving as electrodes. As presented in Figure 3.4, the upper electrode plate (15.6-mm-diameter) is connected to HV and is fitted inside a Delrin® compartment which serves as dielectric barrier with a thickness of 2.0 mm. This compartment is fixed by a screw thread to a second piece of same material in which a floating electrode disk (7-mm-diameter) takes place. The distance between both electrodes can be easily varied by screwing in the topmost cell, where the screw pitch is 1 mm and the maximum allowed gap is 4 mm. The lower electrode is welded to the long wire (diameter of 0.1 mm). It is inserted into a long plastic tube which is tightly attached to the Delrin® enclosure. The used tube is a polyurethane nasogastric feeding tube with a length of 109 cm, 2.5 mm inner diameter and 3.3 mm outer diameter (Covidien, Ireland). The tube was cut in a way that its total length is kept in 1.0 m. Gas connection is made in the region between electrodes and, surrounding the floating disk, 4 holes allows the gas stream to flush into the long tube. When high voltage is applied, a DBD discharge ignites in the primary reactor and a plasma jet is immediately generated at the tube tip end.

The device was operated in two different modes, here assigned as "continuous" (continuously provided AC signal) and burst (section 2.3.1.2) modes. High purity helium was used in both cases and the gas flow (up to 2.0 slm) was controlled by a mass flow controller. In continuous mode, the plasma jet was connected to a non-commercial HV power supply developed at the INP that provides voltage signals with amplitude up to 4.6 kV. The device was always operated in the minimum voltage amplitude required to ignite the discharge, 4.5 kV. For the burst mode, the HV electrode was connected to a commercial AC power supply Minipuls4 (GBS Elektronik GmbH, Germany) that allows amplitude modulation of the voltage signal. Parameters from the power supply, such as burst repetition period (1.0 to 4.0 ms), number of HV cycles (2 to 20 cycles), signal frequency (25 to 35 kHz) and voltage (5 to 15 kV) were varied in order to study the discharge. The distance between electrodes was kept in 2 mm for all experiments, except for one parameters variation experiment in which the gap was changed. Apart from the gap variation, two different diameters of floating wire (0.1 and 0.6 mm) were tested. Also, the effect of different dielectric material with various thickness was investigated.

Figure 3.4: Experimental setup of primary discharge reactor scheme with parallel plates configuration. C represents the capacitor used for power acquisition and R the resistor connected in series for current measurements.
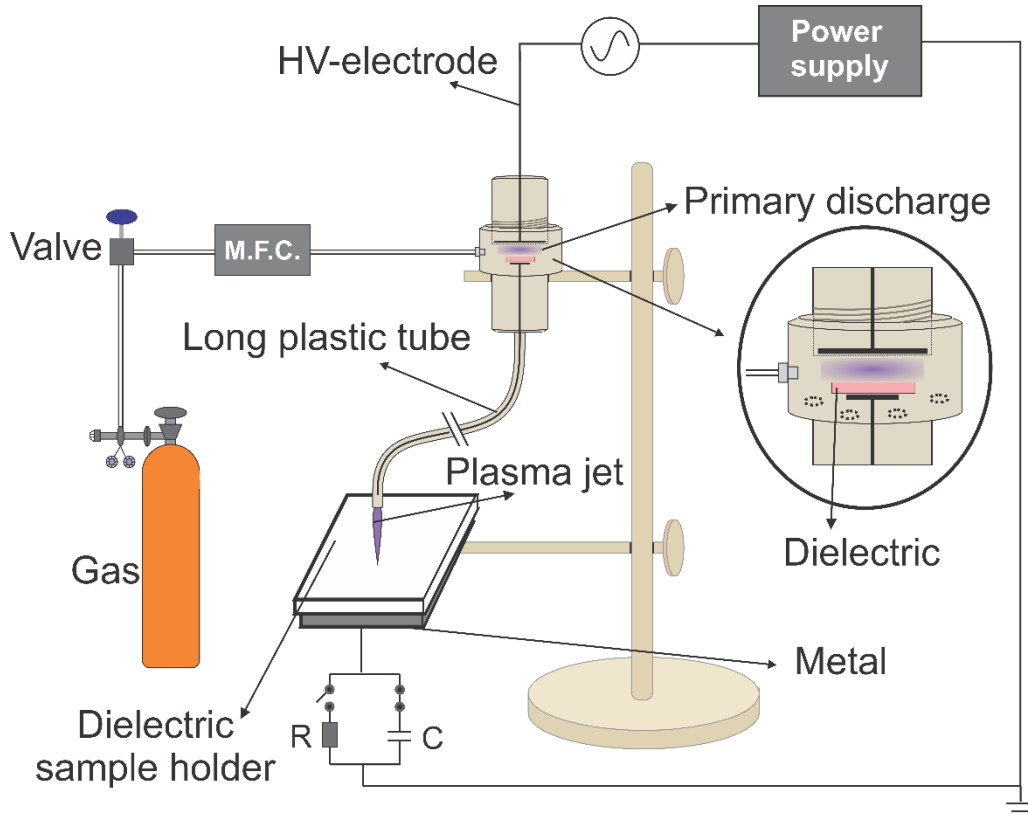
Source: Author's illustration

3.1.2.2 Pin electrode configuration

The second primary reactor configuration used consists of a syringe-like dielectric (Delrin®) enclosure with a pin electrode in its axis (KOSTOV et al., 2015b; NISHIME, 2015) which is embedded in a bottom-closed quartz tube used as dielectric barrier, as shown in Figure 3.5. The working gas, controlled by a mass flow controller (Horiba, model SEC-N100 until 10 slm for N_2), is introduced on the side of the device and, when HV is applied to the central electrode, a DBD is generated in the adjacent region. When no tube is connected to the syringe exit nozzle, a plasma jet is extracted from it and this configuration was already applied in previous works for decontamination (BORGES et al., 2017; KOSTOV et al., 2015b; NISHIME, 2015; NISHIME et al., 2016). In the present study, the above-mentioned long plastic tube was connected to the syringe nozzle (inner diameter of 1.5 mm). In this case, the floating wire tip is placed within the discharge around the HV electrode and a small plasma jet is ejected from the plastic tube downstream end.

Figure 3.5: Experimental setup of primary discharge reactor scheme with pin electrode configuration.
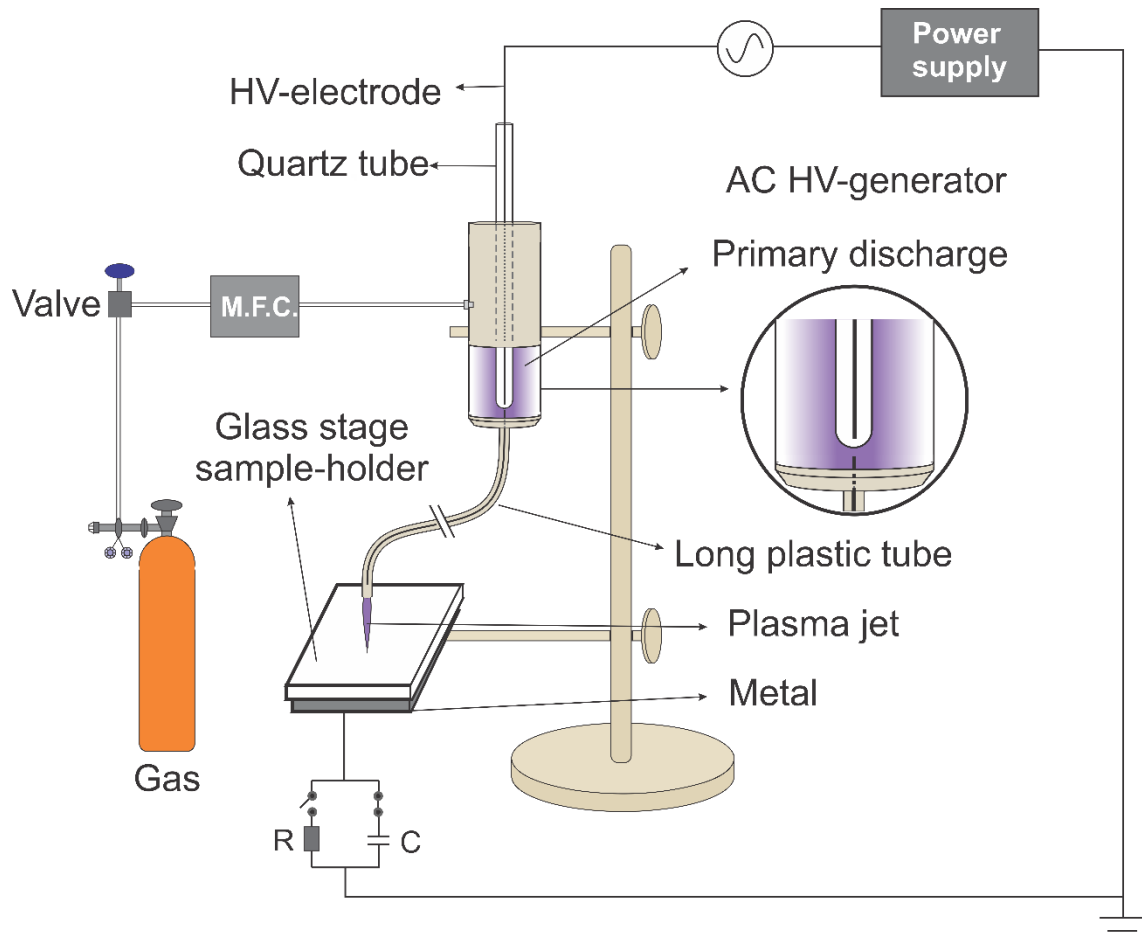
The HV-electrode was connected to the commercial AC power supply Minipuls4 (GBS Elektronik, Germany) operating in burst mode with a modulation frequency of 667 Hz. The voltage signal applied was generated with a frequency of 32 kHz and amplitude of 14 kV. In such conditions, the plasma jet operates stably. The voltage duty cycle was varied from 7 to 45% and the distance between tube tip and target was kept in 5 mm. Helium with 99.5% purity was used as working gas with a gas flow of 2.0 slm.

3.2 DISCHARGE CHARACTERIZATION

3.2.1 Electrical characterization

The voltage signal from the plasma sources was monitored by a digital oscilloscope using a 1:1000 HV probe. The power for each reactor was obtained by the Q-V Lissajous method (see section 2.3.1) using the transferred charge measured by the voltage drop across a HV capacitor. Figure 3.6 presents a simplified plasma jet circuit for electrical characterization of the plasma jets, where for the plasma endoscope, only the plasma jet capacitance (assigned as number 2) is considered. In the schematic circuit, the pink rectangles represent the dielectric barriers between electrodes. In capacitor number 1 of Figure 3.6, the upper dielectric is only present in the case of system parameters variation of section 4.2.1.3. Given the different places in which each plasma source was operated, distinct capacitors were used, by instance, a 1.3 nF capacitor was used for the plasma endoscope (Figure 3.2) and a 10 nF for the long tube plasma jet (see Figures 3.4 and 3.5).

Figure 3.6: Simplified electric circuit representation of the plasma jet
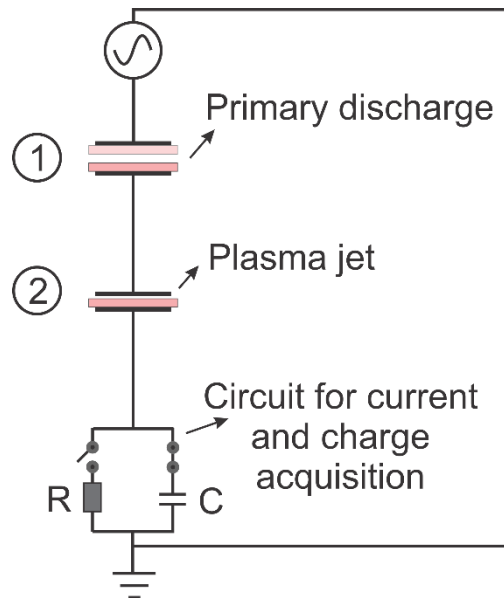
Source: Author's illustration

For acquiring the current flowing through the system, mainly a current monitor TEK CT-1 (Tektronix) that provides a 5 mV/mA voltage signal was used. For the long plasma jet used for applications, the current was obtained by the voltage drop across a serial resistor of 100 Ω.

The setup for electrical characterization is schematized in each experimental setup presented in the previous sections – Figure 3.2 for the plasma endoscope from the INP and Figures 3.4 and 3.5 for the long tube jet from Unesp with parallel and pin electrode configurations respectively.

3.2.2 Plasma jet temperature measurements

The non-conductive probe used for temperature measurement consists of a Teflon-coated glass fiber with a 550-µm-diameter GaAs crystal at the tip end (OPTOcon GmbH, FOTEMP1-OEM). It provides a voltage signal proportional to the temperature that was acquired through a voltage input module (NI-9205, National Instruments) connected to a data acquisition chassis (cDAQ-9178, National Instruments). The equipment used for temperature analysis belongs to the Leibniz Institute for Plasma Science and Technology (INP) – Greifswald, Germany. Therefore, only the plasma endoscope and the long tube jet with parallel plates configuration could be analyzed with this method.

The plasma jet position was handled by X-Y-Z step motors that were controlled by a self-developed LabView program. This allowed the temperature investigation in consecutive cross sections along the floating plasma plume, as displayed in Figure 3.7 (a). Each cross section was scanned with 20 steps of 100-µm for the plasma endoscope and 30 steps of 200-µm for the long tube jet generating a temperature profile for accurate detection of the temperature in the jet axis. For temperature measurements when the jet is in contact with a target, the plasma jet nozzle was fixed above a grounded Petri dish as shown in Figure 3.7 (b). In this case, the plasma endoscope nozzle was kept 3 mm above the surface, while the tip of the long tube jet was fixed at a distance of 4 mm. Due to the crystal sensitivity and measurements deviation from the motor's position, a maximum deviation of $\pm$ 0.4 ˚C was considered for all temperature data.

Figure 3.7: Temperature measurements setup for (a) floating configuration and (b) using the grounded Petri dish. In (a), the red circles represent the spots for temperature acquisition. Dist: distance between two steps.

(a)   (b)
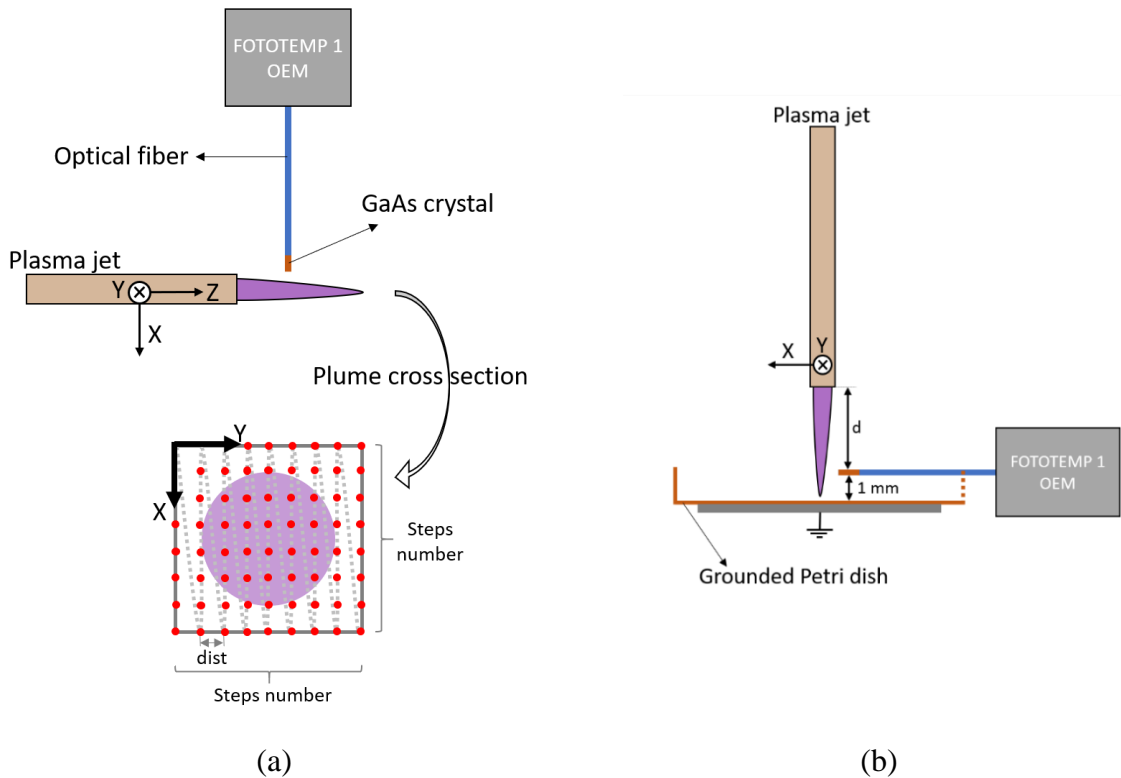
Source: Author's illustration

3.2.3 Optical emission spectroscopy (OES)

Optical emission spectroscopy was performed for all plasma sources, however, different spectrometers were used for each plasma jet. The long tube jet used for applications (pin electrode configuration, described in section 3.1.2.2), was operated at Unesp (Brazil) and was analyzed using the spectrometer Shamrock 303I, Andor Technology, borrowed from the Physics Institute "Gleb Wataghim" – Unicamp. This spectrometer of spectral resolution of 0.1 nm has a focal length of 30 cm and the light was focused by a set of two plane-convex quartz lenses. The first, with focal length of 15 cm, captures the light from the plasma, while the second one, with focal length of 30 cm, is used to converge the light beam into the slit. With this configuration, it is possible to analyze the emission of excited species with certain spatial resolution (around 0.5 mm).

The other two plasma sources, the plasma endoscope (described in section 3.1.1) and the long tube jet with parallel plates configuration (described in section 3.1.2.1) were analyzed at

the Leibniz Institute for Plasma Science and Technology (INP, Germany) using the dual channel spectrometer AvaSpec – 2048-2-USB2, Avantes with spectral resolution of 0.7 nm. A bifurcated optical fiber was used to connect both channels to the set of lenses. A similar set of quartz lenses, as described above, was used in this case, but the second lens focused the light beam into the optical fiber. A simple scheme of the lenses set configuration is shown in Figure 3.2 for the plasma endoscope. As described, a similar setup was employed for the long tube jet with pin electrode configuration.

3.3 APPLICATIONS

Due to its flexibility, plasma jets can be applied in many different fields. Here, the efficacy of the long tube jet from Unesp for material treatment and decontamination was investigated. For both usages, the pin electrode configuration (described in section 3.1.2.2) was employed.

3.3.1 *Candida albicans* inhibition

All samples preparation procedures and antimicrobial analyses were performed in collaboration with microbiology group from the São Paulo State University – Unesp at São José dos Campos. The reference strain *Candida albicans* SC 5314 was used for the assays. Cultures were kept in Sabouraud Dextrose (SD) broth supplemented with 20% glycerol at -6ºC. To obtain fresh cultures, *C. albicans* cells were plated in SD agar and incubated at 37ºC for 24h, under aerobiosis. The working suspensions were obtained by resuspending fungal colonies in 0.9% NaCl solution. Suspensions were standardized spectrophotometrically to 10^6 cells/mL. An aliquot of 100 µL of the fungal suspension was plated on Sabouraud agar with sterile swabs. The plates were dried under sterile laminar flow device at room temperature for 15 min and then exposed to plasma for 30, 60, 120 and 180 s in triplicate. As control, the inoculated plates were placed under helium flow without plasma ignition (plasma off). After treatment, plates were incubated for 24h at 37ºC, under aerobiosis, and then the fungal growth was analyzed. To investigate the efficacy of decontamination using the plasma jet, the shape and size of the inhibition zones were measured. Since in the most cases the observed inhibition zones were approximately round, their diameters were used as an indicator of the fungal decontamination efficiency.

3.3.2 Polymer treatment

Samples of polyethylene terephthalate (PET) with thickness of 0.5 mm were obtained from commercial colorless water bottles from Schincariol (Kirin Company), Brazil. The samples were removed from the most regular region of the bottle and cut into small squares of 50 x 50 mm. Due to material curvature, the samples were glued on glass microscope slides of 1-mm-thickness using double-sided tape. To help identifying the actual treatment position, a piece of grid paper was glued in between the glass slides and the polymer, as shown in Figure 3.8.

Figure 3.8: Polymer film preparation for plasma treatment. The square PET sheet was glued on top of a glass plate with grid paper.
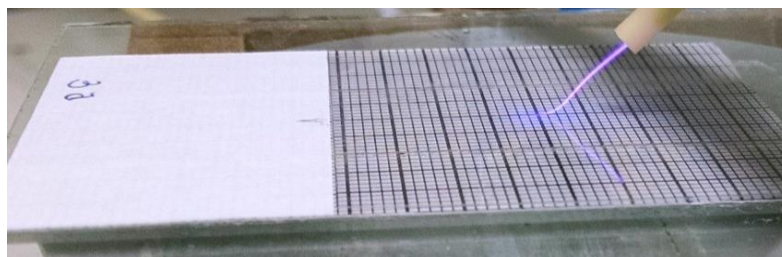
Source: Author's illustration

The cleaning procedure was performed using an ultrasound cleaner. The samples were placed in beakers with cleaning substances inside the cleaner. Firstly, the samples were washed for 10 min with distilled water and detergent. Then, to remove organic impurities from the surface, they were rinsed with isopropyl alcohol (99.9% purity) for more 20 min. Following, the samples were washed for 20 min with only distilled water to remove possible contaminant residues. At last, the samples were dried in a controlled environment at room temperature.

The treatments were performed with three different tilting positions with and without a grounded counter electrode. The plasma jet was placed in a way that the plume formed angles of 90º, 45º and 0º with the PET surface. For the perpendicular case (90º), the distance was varied from 5 to 15 mm, while for the parallel case (0º) a distance of 2 mm was set and the gas flow rate was changed from 1.0 slm to 3.0 slm.

3.3.2.1 Water contact angle (WCA) analysis

To perform contact angle measurements, the goniometer Ramé-Hart 300-F1, from the Department of Physics and Chemistry, FEG/Unesp, Brazil, was used. The measurements were taken in static mode using deionized water with droplets of 0.3 µL. The drop image is acquired by high resolution camera and the contact angle is automatically calculated by the DROPimage standard software.

The drops were equally spaced each 3 mm on top of the samples to provide a surface mapping, as shown in Figure 3.9. Due to the small dimension of the plasma jet, this measurement method allows the identification of the actual modification zone.

Figure 3.9: Schematic illustration for water contact angle measurements to obtain a surface mapping.
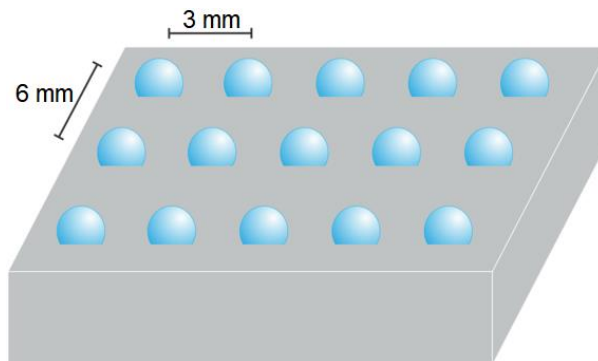
Source: Author's illustration

4 RESULTS AND DISCUSSION

4.1 PLASMA ENDOSCOPE (INP)

4.1.1 Using air as shielding gas

The plasma endoscope was designed to have small dimensions thus consuming small gas flow rates and operating with relative low power. As described in section 3.1.1, this plasma jet device consists of two concentric tubing systems, conducting the feed and the shielding gas. Applying helium with 300 sccm as feed gas and 300 sccm air shielding gas, the discharge ignites at a voltage amplitude of 1.75 kV at a frequency of 14.2 kHz and a plasma plume emerges from the nozzle (endoscope tip) when the voltage is further increased. Some parameters variation such as voltage, gas flow rate and distance to sample can result in a wider range of power. Figure 4.1 presents the power measurements of this endoscopic plasma jet at a distance of 3 mm from a grounded Petri dish. The measurements were taken for different values of applied voltage and He feed gas flow. Pictures of the plasma plume are displayed at the four edges of the graph. The weakest plasma jet intensity (lower left-hand side picture) corresponds to low applied voltage combined with a low gas flow rate. This condition also corresponds to the lowest dissipated power achieved. On the other hand, for high values of applied voltage and high gas flow (upper right-hand side photograph) the discharge appears much more intense, reaching the grounded electrode and exhibiting higher power values when compared to other conditions. It can be observed that the power strongly depends on the applied voltage, while higher gas flow rates have little influence on its values. However, for feed gas flow lower than 200 sccm, the effect of gas flow rate on the power is more pronounced.

According to Figure 4.1, the power can be adjusted by the input voltage and the feed gas flow. Depending on the application, the precise control of discharge power is necessary. On the one hand, some of them, such as blood coagulation (MINKYUNG LEE et al., 2012), wound healing and skin disinfection (HEINLIN et al., 2011), require cold plasmas with low discharge power to avoid damaging the surrounding tissue. On the other hand, applications concerning devitalization and tissue reduction, e.g. removal of tumors and treatment of overlarge nasal conchae (RAISER; ZENKER, 2006), may demand a higher power.

Figure 4.1: Discharge power measurements on the endoscopic plasma jet source for different applied voltages (each 0.25 kV) and He feed gas flow (each 50 sccm). Contains 88 measurement points.
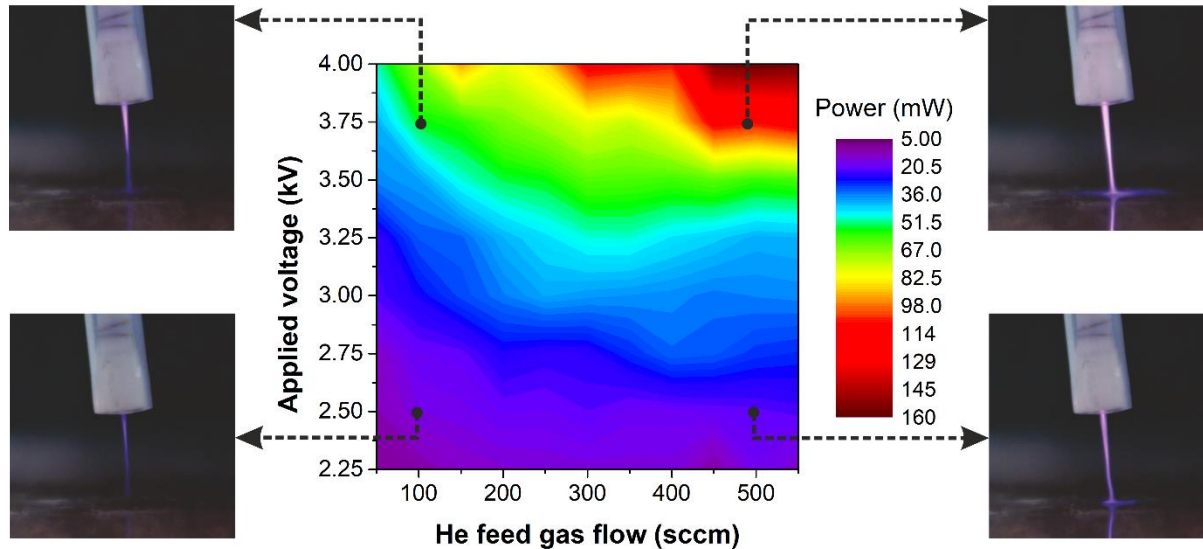
The present plasma jet was developed for endoscopic operation. Thus, for future in-body applications it is necessary to fulfil some requirements, such as low temperature and capability of operating inside closed cavities. Another important condition would be the non-production of toxic compounds or impurities. As a result of the endoscope configuration, discharge can be generated inside the plastic tube degrading the material. To avoid the undesired in-tube plasma generation, the wire electrode winding distance plays an important role. When a bigger distance between two loops exists, the sudden drop in the electric field leads to a big potential difference in region causing discharge. If the wire winding is made narrower, the electric potential remains approximately constant and no plasma ignition is observed within the tube (WINTER et al. 2018). Those differences caused by the winding distance can be observed in Figure 4.2 in which narrow and wide spiralling around the feed gas tube were photographed. In the narrow winding regions, no discharge can be observed. On the other hand, in the part of the tube in which the winding spacing was made broader than 2 mm, plasma is generated. Therefore, the distance between two adjacent windings of the HV electrode was set to 80 µm, the equivalent of 6 loops in 1 mm-length.

Figure 4.2: Influence of the electrode winding distance in the generation of plasma inside the endoscopic tube. (a) Experimental setup photograph and (b) scheme of the winding distance differences.
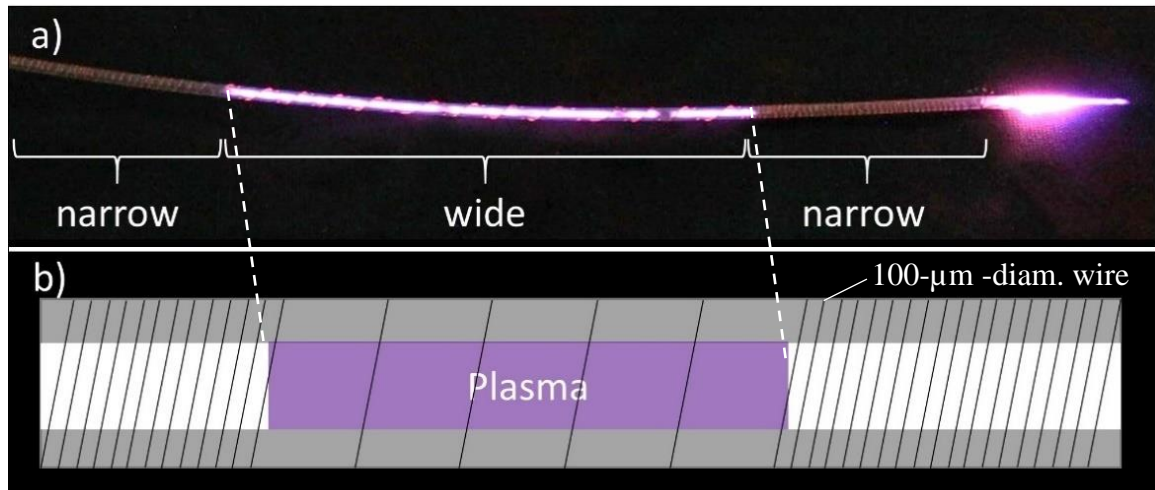
Source: Adapted from Winter et al. (2018)

Temperature is one critical factor concerning the use of plasma devices in the biomedical field. In order to allow its manipulation inside living bodies, the temperature limitation is around 43 °C (DEWHIRST et al., 2003). Higher temperatures can lead to changes in cellular membrane and internal molecular structures, can also result in formation of edema and approximately double the rate of epidermal necrosis for each degree of temperature increased (MORITZ; HENRIQUES, 1947).

The temperature measured for different values of discharge power is presented in Figure 4.3. The plasma jet operated with both helium and shielding air flow of 300 sccm and the measurements were taken at 2 mm from the nozzle. Within these parameters, the plasma plume has a total length of 3 mm and spreads over the grounded platform. It can be observed in Figure 4.3 that the plasma jet temperature does not exceed 31 °C, and thus, this endoscopic He plasma source operates far from the biological intolerance limit of 43 °C. Figure 4.3 also shows a linear dependence of the plasma temperature with the discharge power as expected according to Equation 5. This behaviour demonstrates that the working temperature can be easily adjusted by controlling the plasma jet power.

Figure 4.3: Linear dependence of the plasma plume temperature with discharge power for a grounded setup.
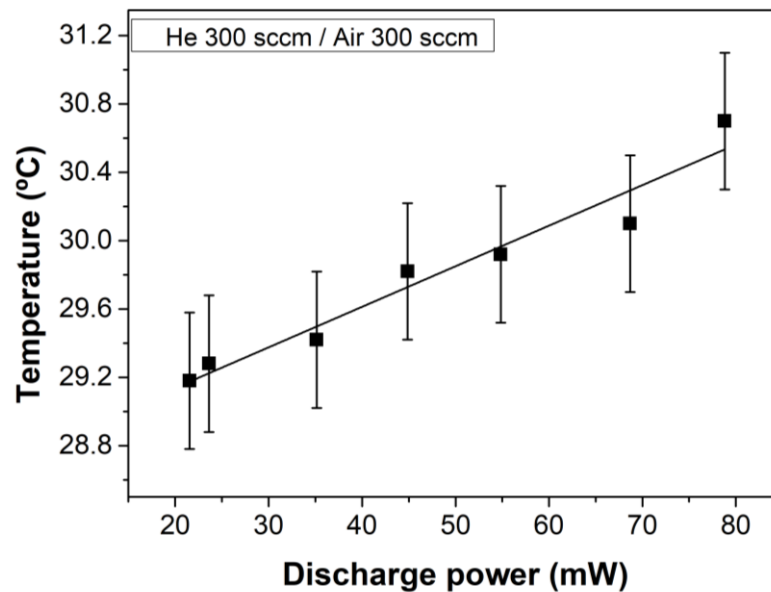
Besides the low temperature aspect, endoscopic plasma sources must allow an in-body manipulation. Particularly, it should operate inside closed cavities regardless the atmosphere. When a plasma jet is placed inside a container, the feed gas displaces the originally present air creating a new internal environment. If a noble gas is used, the new environment will supress the plasma plume formation due to the lack of oxygen (REUTER; VON WOEDTKE; WELTMANN, 2018). It was demonstrated by Schmidt-Bleker and coauthors (2015) that when a non-electronegative gas is flushed around the plume region, the electrons diffuse in radial direction close to the nozzle. They also revealed that in the presence of an electronegative gas – e.g. oxygen – negative ions are formed as result of electrons attachment forming a layer of anions around the jet column. The electric field generated by this layer works as a plasma sheath and bound the electrons avoiding the radial diffusion (SCHMIDT-BLEKER et al., 2015). Thus, the use of electronegative shielding gas helps the formation of a plasma plume when operating inside cavities.

In the present work, a quartz cavity was employed to create a closed environment. The tube was inserted into the cavity and the length of the plasma plume was investigated when both gas flows, i.e. feed (helium) and shielding (air) gas, were varied. The measured jet length is presented in Figure 4.4 for different values of gas flow rates together with some pictures of the plasma plume length. It is evident in Figure 4.4 that the plume length strongly depends on the feed gas flow. Varying the rate of shielding gas does not influence the plasma jet dimensions

for helium flows smaller than 300 sccm. However, when feed gas flow is further increased the plasma plume tends to shorten. This effect can be attributed to turbulences at the tip of the jet. Additionally, when the shielding gas is set to low values while the feed gas flow is kept high, the plasma jet tends to convert to a glow-like discharge. In this case, the plasma channel expands losing its well-defined plume shape and filling the entire cavity length, as can be observed in the right-hand side picture in Figure 4.4.

Figure 4.4: Influence of the feed and shielding gas flows on the plasma plume length when operating inside a closed cavity. Contains 160 measurement points.
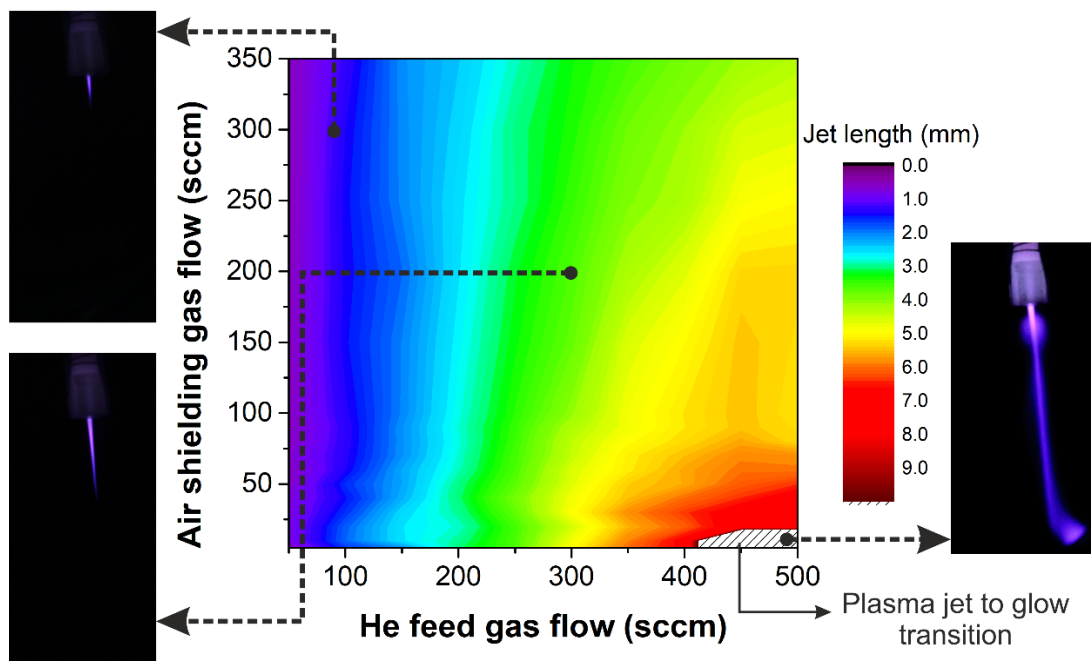
Source: Adapted from Winter et al. (2018)

Considering the different environments when operating a plasma jet inside and outside a cavity, OES was used to compare the emissions in both conditions. For comparison reasons, all controllable parameters were kept the same in both cases – for instance, an applied voltage amplitude of 3.0 kV, frequency of 14.2 kHz and both gas flow rates in 300 sccm – except for the quartz cavity. The spectra are displayed in Figure 4.5. Except by the OH peak at 308 nm observed for the open case, both spectra present the same emission lines although some peaks have different intensities. As expected, lines of atomic He between 550 nm and 710 nm are present with similar emission intensity in both spectra. Also, the atomic oxygen peak at 777 nm appears with same intensity in both cavity settings. In the open-air condition, Figure 4.5 (a), the OH band at 308 nm suggests that a significant amount of humid air get decomposed by the

plasma jet after being dragged into the effluent region (plasma plume) (WINTER et al. 2018). Another evidence of the turbulent interaction with the ambient air for the outside case is the higher intensity for the nitrogen emission lines. The highest peaks observed for this case correspond to the N_2 second positive system bands and to the first negative system band (N_2^+). This last one confirms the presence of excited nitrogen molecular ions that are commonly excited by He metastables by Penning ionization processes (HÜBNER et al., 2014, NASTUTA et al., 2017). Once the emission intensity for the He lines is approximately the same inside and outside the cavity, a similar excitation behaviour is expected for both cases. So, the excited nitrogen peaks intensity can be correlated to the amount of available nitrogen in the environment. Since both gas flow rates used are same in value, the atmosphere inside the cavity is roughly composed by 50% He and 50% air. Therefore, it is expected to observe a lower intensity for excited nitrogen in the case of a cavity as shown in Figure 4.5 (b).

Figure 4.5: Optical emission spectroscopy measured at the effluent region of the endoscopic plasma source for an applied voltage of 3.0 kV, frequency of 14.2 kHz and 300 sccm of feed and shielding gas. Figure (a) shows the emission spectrum in open air, while (b) displays the results from in-cavity operation.
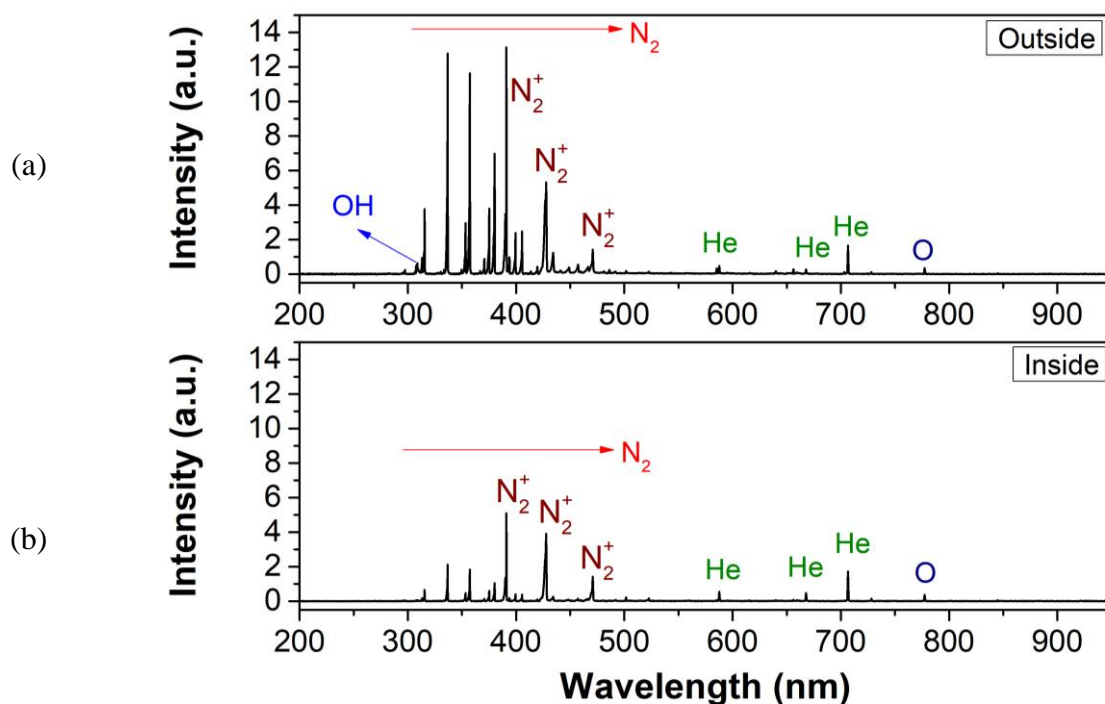
Source: Adapted from Winter et al. (2018)

Working with air as shielding gas allows the plasma endoscope to operate inside closed environments with minor changes in the excitation behaviour. Thus, the plasma jet can be mounted inside an endoscope device for further analysis. However, for security reasons, the endoscope housing has a grounded interior which can be problematic due to the HV electrode along the tube. As a result of the intense electric field between the HV winding electrode and the grounded housing, some parasitic discharges may arise not just inside the shielding gas tube but also inside the endoscope structure. Figure 4.6 (a) shows a picture of the jet tube with a grounded wire around it when air is used as shielding gas and is flushed in the outermost tube observed in the picture, representing the endoscope housing. It is noticeable the formation of parasitic discharges along the tube. To make it more evident, Figure 4.6 (b) presents the current and voltage signals for the current setup. The parasitic discharges in air are depicted by randomly distributed current peaks in the rising and falling cycles of voltage. Parasitic discharges must be avoided for being assured causes of considerable tube erosion (WINTER et al. 2019). Besides the risk of contaminating the discharge with eroded material, the parasitic discharges can contribute to shorten the device lifetime.

Figure 4.6: Visualization of the parasitic discharges generated when air is used as shielding gas with 300 sccm. In (a) is presented the setup picture with transparent tube and in (b) the voltage and current signals. In both cases, air at 1000 sccm was flushed inside the outermost tube.

(a)

(b)
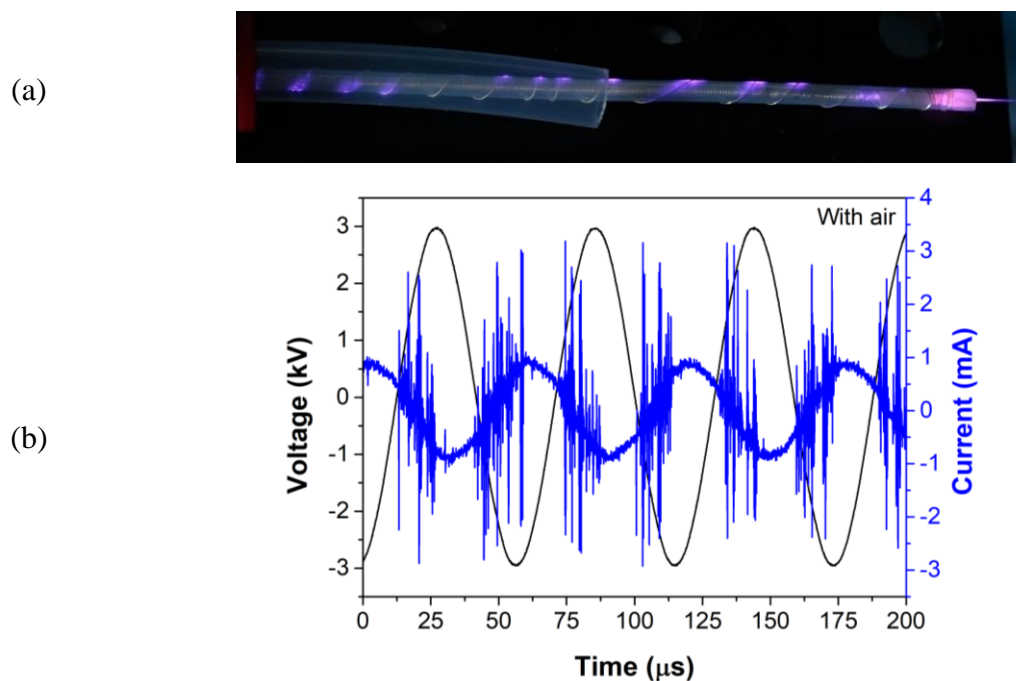
Source: Adapted from Winter et al. (2019)

4.1.2 Avoiding parasitic discharges

One possibility to avoid the parasitic discharges is to change gas, filling this specific area by one with higher breakdown voltage. Carbon dioxide (CO_2) is also an electronegative gas, which is a crucial property for the shielding gas and has a higher ignition voltage than air, as can be checked in the Paschen curve in Figure 2.1. In addition, CO_2 is the most common gas used to pump up organs for endoscopic treatments. Firstly, the plasma endoscope was operated with air as shielding gas while flushing CO_2 through the outer tube (that corresponds to the endoscope housing). The result is shown in Figure 4.7 (a) where the parasitic discharges suppression only within the CO_2 flushing tube is evident. Looking carefully to Figure 4.7 (a), parasitic discharges can be seen both inside and outside the shielding gas tube; hence, CO_2 could also be employed as solution for the shielding gas.

Figure 4.7: Visualization of the parasitic discharges suppression when CO_2 is flushed into the outermost tube. In (a) is presented a picture with transparent outer tube where CO_2 is fed at flow rate of 1000 sccm while using air (300 sccm) as shielding gas. In (b) is shown the voltage and current signals.

(a)

(b)
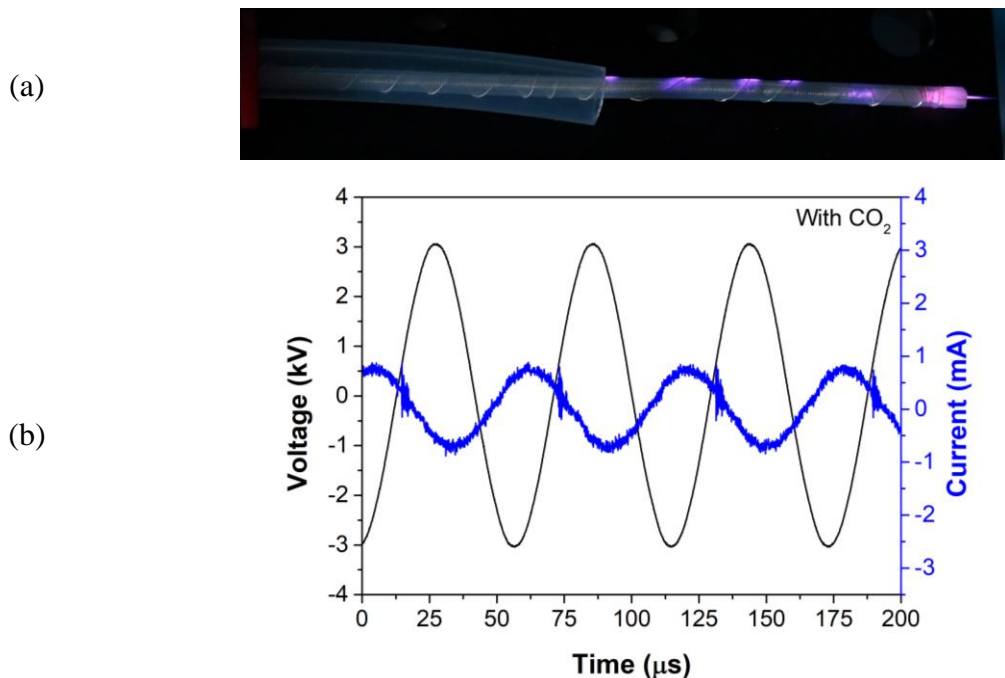
Source: Adapted from Winter et al. (2019)

Accordingly, the plasma jet was operated using carbon dioxide as shielding gas as well as flushing inside the endoscope housing and the resulting voltage and current signals are

presented in Figure 4.7 (b). When CO_2 is used in both tubes (shielding gas and endoscope), all parasitic discharges disappear and only current peaks that are typical from He discharges are observed. Thus, CO_2 revealed to be a better option for the shielding gas.

4.1.3 Comparing different feed gases

In the first subsection of section 4.1, the importance of a refined control of jet power was mentioned. Even though the helium jet can operate with very low transferred charge, the range in which the plasma reaches higher power values is certainly small. Thus, the study of the plasma endoscope operating with a different noble gas is presented. Henceforth, CO_2 is used as shielding gas to avoid the formation of parasitic discharges. It is used at a flow rate of 300 sccm, except for the cases with shielding gas flow variation. Here, the plasma endoscope operating with helium and neon are compared.

Differently from the helium discharge, the neon jet ignites at a voltage amplitude of 1.5 kV and appears much brighter easily reaching the grounded Petri dish underneath. The photographs of the plasma endoscope working with the two different feed gases are displayed in Figure 4.8. Visually, both plasma jets are very different. The neon plume is much longer and for all cases spreads over the surface, while the helium jet is shorter and does not touch the counter electrode for any of the showed conditions. Once the ionization potential of neon (V_{ion} = 21.56 eV) is lower than the ionization potential of helium (V_{ion} = 24.59 eV), it is expected for the neon to ignite for lower applied voltages. When the voltage amplitude exceeds 3.0 kV, a back-directed discharge can be observed for the neon jet. Equivalently to the parasitic discharges, the back-directed discharge can highly degrade the tube material and therefore, must be avoided.

Figure 4.8: Photographs of helium and neon plasma jets operating with different input voltages. The nozzle is placed at 3 mm above a grounded Petri dish. CO_2 is used as shielding gas in both cases.
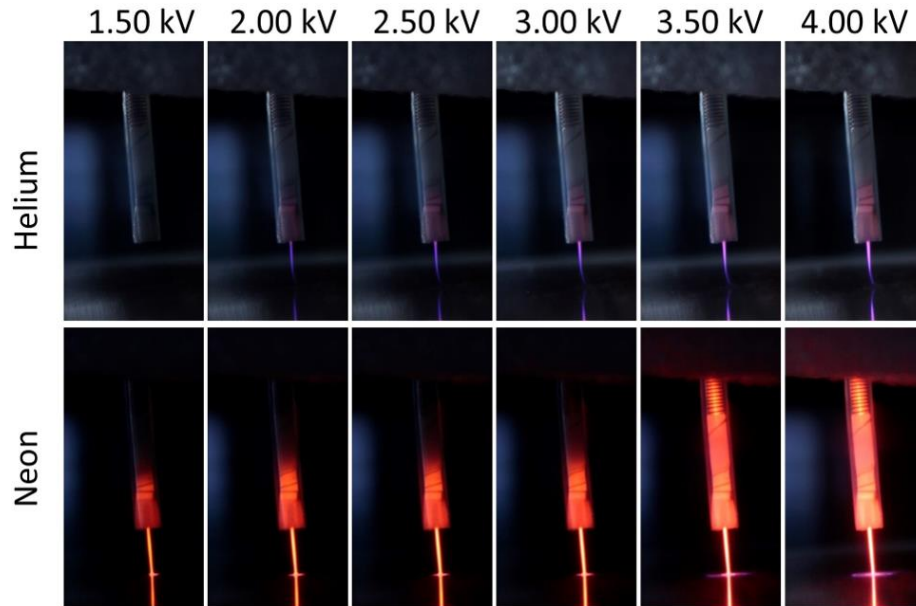
Figure 4.9 shows the results for dissipated power on the counter electrode for a distance of 3 mm for both feeding gases. Here, the applied voltage and feed gas flow rate of helium and neon are varied while CO_2 gas flow rate and distance to the grounded Petri dish remain fixed. The helium discharge power graph, Figure 4.9 (a), is very similar in values to the one presented previously when using air as shielding gas (Figure 4.1). The trend of transferred charge to the capacitor is the same for both gases although the neon discharge reaches higher values of power. Up to almost 2.7 kV of voltage amplitude, the power values of neon and helium discharges are very similar, except by the sudden increase of power that occurs between 250 and 400 sccm of Ne flow possibly due to changes in operating gas flow regimes. For voltages higher than 3.4 kV, the neon jet exhibits significantly higher power values. The ionization rate of neon discharge is possibly higher due to the low energy metastable level (Ne* $^3P_0$ = 16.72 eV) allowing an easier discharge ignition. For the helium case, the energy of the lower metastable level (He* 2^3S_1) is 20.62 eV which might result in a lower Penning ionization rate. This higher power dissipation can be correlated to the back-directed discharge observed in Figure 4.8 that only occurs for neon feed gas. Higher feed gas flow rates seem to have little effect on the discharge power for both cases. As showed before, He gas flow rates below 200 sccm seem to play a role for the He jet power. However, in the case of neon discharge, the power only appears to be less influenced above 300 sccm.

Figure 4.9: Discharge power variation for different values of applied voltage (each 0.25 kV) and feed gas flow (each 50 sccm) for (a) helium and (b) neon discharges. Each graph contains 90 measurement points.

(a)   (b)
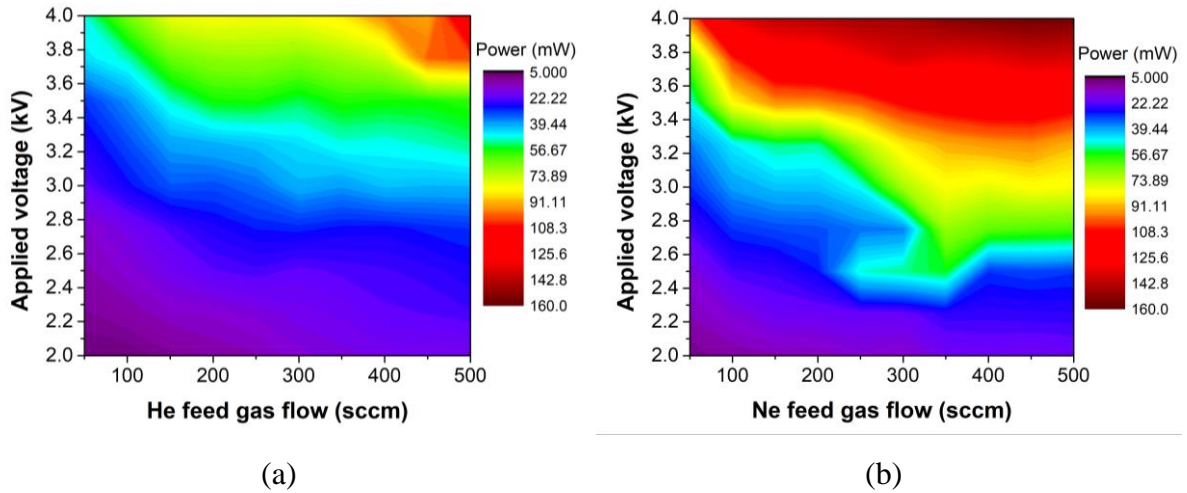
Source: Author's illustrations

Even though the neon plasma jet reaches much higher power values than the helium, its temperature it slightly lower. The temperature measurements obtained for the grounded setup are presented in Figure 4.10 for comparison. Both feed gases were fed with a flow rate of 300 sccm with shielding gas of CO_2 (also with 300 sccm), voltage amplitude of 3.0 kV and frequency of 14.2 kHz. As shown before for the He case, it presents a linear temperature dependence with the discharge power. For the Ne case, an approximately linear behaviour can be observed for higher power values, but not for lower values as can be observed in Figure 4.10. However, the temperature values of different gases differ by approximately 1ºC. Even for higher power values of more than 100 mW the gas temperatures of both discharges do not exceed 30ºC, still under the limitation value described in subsection 4.1.1.

The shielding gas is essential for the proper endoscope application of this plasma jet. However, having a gas around the main channel can affect the plume interactions with the surrounding environment and compromise the generation of some reactive species. OES was used to investigate the excited species in the presence or absence of CO_2 shielding gas. The analysis was performed in ambient air (outside the cavity) with a counter electrode at a distance of 3 mm from the nozzle. The spectra are presented in Figure 4.11, where (a) and (b) correspond to the discharge in helium and (c) and (d) to the neon jet. For the helium discharge, Figure 4.11 (a,b), roughly the same spectral lines as in Figure 4.5 were observed. Lines of atomic He at 587.6, 667.8, 706.5 and 728.2 nm appear with similar intensity in the absence – Figure 4.11 (a) – and presence – Figure 4.11 (b) – of shielding gas. The same applies to the observed oxygen

species, the triplets of atomic oxygen emission lines at 777.2 and 844.6 nm and the emission bands of OH at 308 nm. However, the intensity of nitrogen emission lines corresponding to the second positive system bands (N_2) are clearly reduced when CO_2 is used as shielding gas with a flow rate of 300 sccm. One interesting aspect is that the detected emission lines from the first negative system bands (N_2^+) also present similar intensities after introducing the shielding gas (CAMACHO et al., 2007). Since most of the excited nitrogen ions derive from Penning ionization process with helium metastables, the use of CO_2 as shielding gas does not seem to affect the energy transfer process from those species, but only reduces the amount of available nitrogen in plasma effluent.

Figure 4.10: Linear dependence of the plasma plume temperature with higher values of discharge power. The temperature was measured in the grounded plasma jet at 1 mm above the grounded Petri dish for a total distance of 3 mm between nozzle and surface.
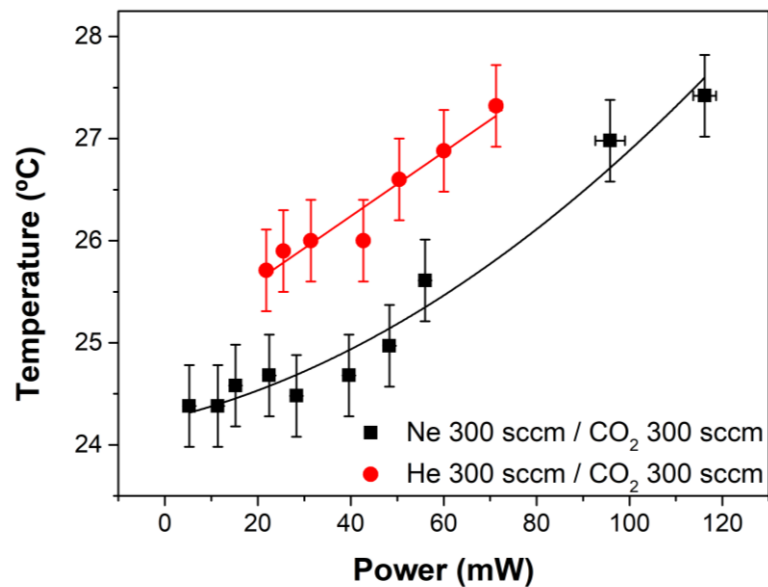
Source: Author's illustration

Figure 4.11: Optical emission spectra from the effluent regions of the endoscope plasma jet working with (a,b) helium and (c,d) neon feed gases in the presence (b,d) or not (a,c) of shielding gas.
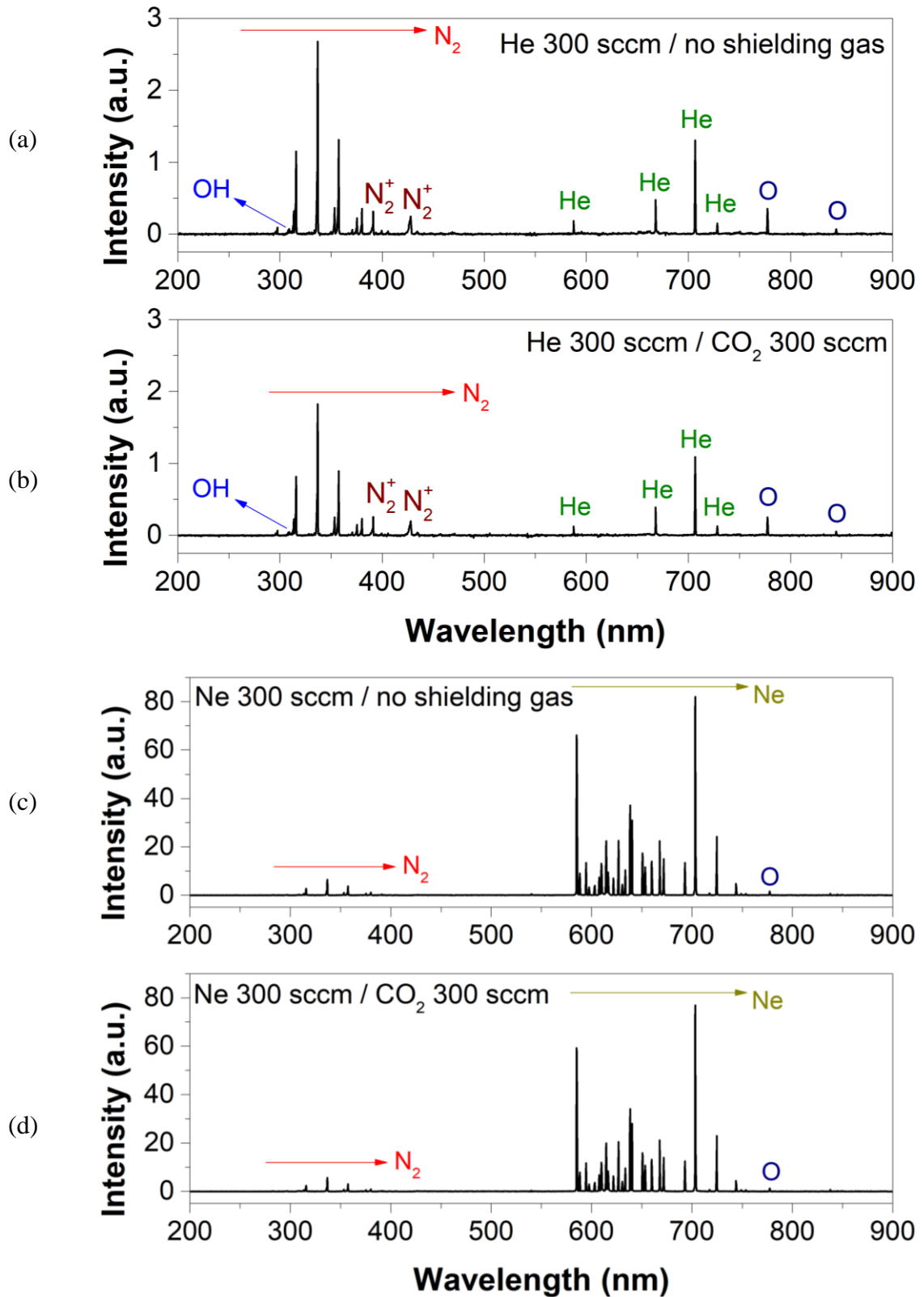
For the neon discharge presented in Figure 4.11 (c,d), as expected, very intense excited atomic Ne emission lines are observed between 585 and 744 nm with same intensity for both conditions. Possibly, the main ionization process that takes place is the Penning ionization between two neon metastable species. Besides the intense neon lines, atomic oxygen emission at 777.2 nm and some nitrogen lines relative to the second positive system bands (N_2) can be identified with similar intensity in the absence – Figure 4.11 (c) – and presence – Figure 4.11 (d) – of shielding gas. Apparently, the neon jet excitation processes seem to be less affected from using CO_2 as shielding gas.

Another investigation concerning the operation of this plasma source was the influence of shielding and feed gases on the discharge power values. Power graphs for both feed gases when keeping the applied voltage constant at 3.0 kV are presented in Figure 4.12. Previously, in Figure 4.9, it was observed that decreasing the feed gas flow under 200 and 300 sccm influences the mean power for the helium and neon jets, respectively. However, when applied voltage is kept constant and both feed and shielding gases are varied (Figure 4.12) no influence from the shielding gas can be detected. For 3.0 kV of voltage amplitude, the effect of neon flow variation – Figure 4.12 (b) – is more pronounced than helium – Figure 4.12 (a). However, the power values for the neon discharge remain uniform above 200 sccm.

Figure 4.12: Influence of feed and shielding gas flow variation (each 50 sccm) on the power values when using (a) helium and CO_2 and (b) neon and CO_2. Each graph contains 80 measurement points.

(a)   (b)
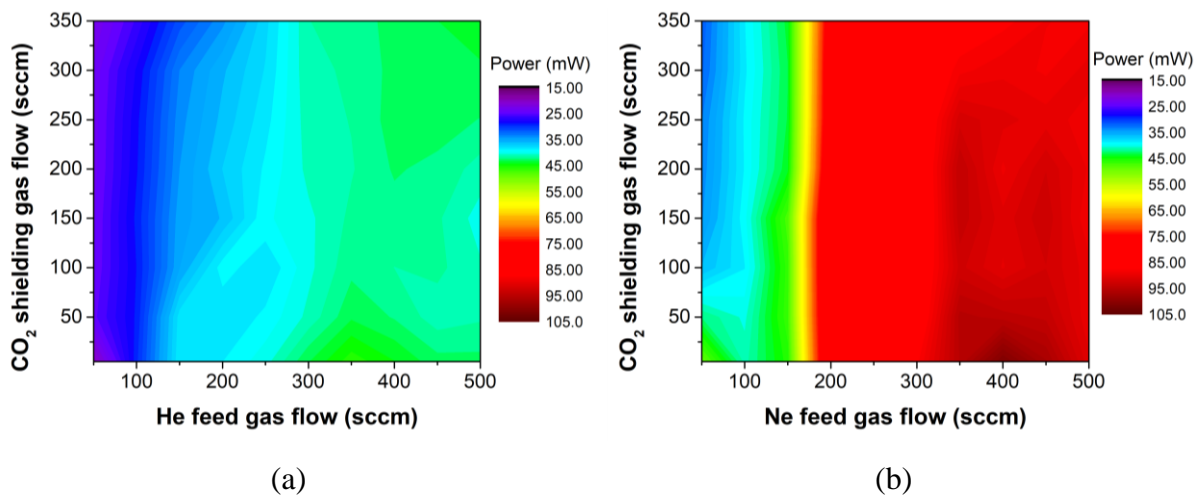
Source: Author's illustrations

The importance of the shielding gas for the in-cavity operation was already mentioned. Even though the shielding gas variation does not influence the plasma jet power, it guaranties

that the plasma plume can keep its shape in closed environments. Figure 4.13 displays the different plume lengths when changing feed and shielding gas flow rates of the plasma jet operating inside a closed cavity. In both feed gas cases, a low feed gas flow combined with high shielding gas flow rate results in short plasma jets of around 1-2 mm. Longer plumes are achieved by increasing both gas flow rates. However, the neon jet – Figure 4.13 (b) – is always longer than the helium – Figure 4.13 (a) – for all possible combinations of parameters. The helium plume gradually increases mainly affected by the feed gas variation. In general, its length remains between 2 to 5 mm and only for smaller CO_2 rates it extends to 7 mm. For the neon case, the jet rapidly increases reaching lengths of around 8 mm for a big range of flow settings. Further decreasing the shielding gas leads to the transition to glow discharge in both cases, pointed in the graphs as dashed areas. When small concentrations of CO_2 are provided, the feed gas concentration increases inside the cavity leading to a lack of electronegative barrier around the plume allowing the diffusion of electrons from the jet. Even though this transition region is bigger for the CO_2 case than for air, the range of possible parameters for punctual in-cavity operation (jet form) is large. Also, a precise control of operation regimes (local or diffuse) can be attractive depending on the desired application.

Figure 4.13: Plasma plume length characterization for (a) helium and (b) neon feed gas in dependence of the feed and shielding gas flow rates. The dashed areas represent the parameters combinations in which the plume evolves to a glow discharge. Each graph contains 160 measurement conditions.

(a)   (b)
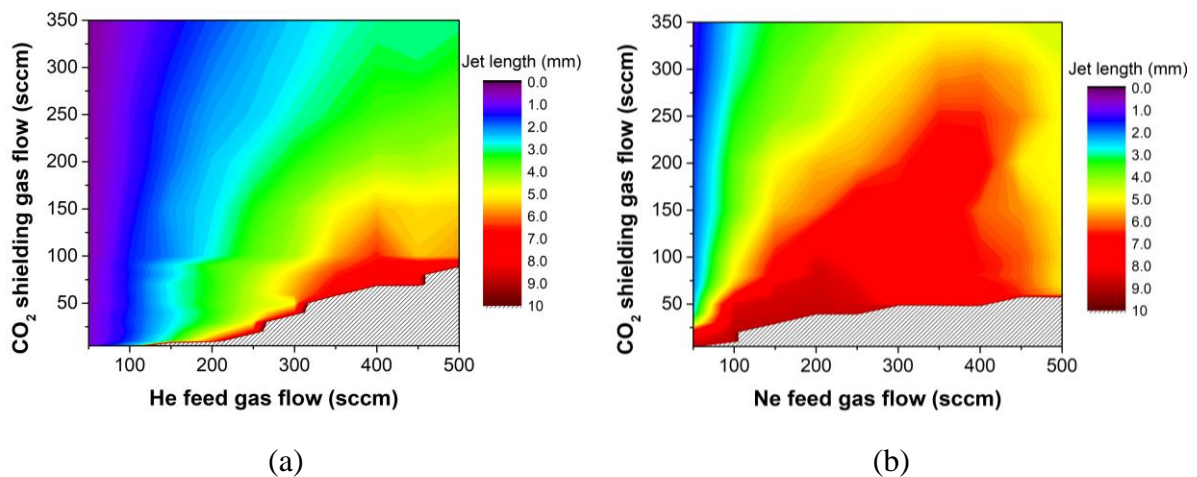
Source: Winter et al. (2019)

When the plasma jet is not directed to a conductive surface – being covered by a dielectric – it can be said that the plume is operating in a floating regime. A floating jet behaves differently

from a grounded one due to lack of surface charge generation and charge transfer processes and therefore, besides visually, power and temperature usually differs. This difference can be better visualized in Figure 4.35 of section 4.2.2.3 for the PET surface modification using another plasma jet device. If the plasma jet is operated inside a body by means of an endoscope, while it is not pointed to any specific spot and if the distance to the skin wall is sufficiently large to avoid the discharge disturbance, it operates in floating mode. Thus, it is important to check how the plume temperature changes along its length and further when no grounded substrate is presented.

The temperature measurements from the floating jet operating with helium and neon feed gases are presented in Figure 4.14. For this analysis, the floating plasma jet was operated with an amplitude voltage of 3.0 kV and both feed and shielding gases with a flow rate of 300 sccm. Here, the temperature discrepancy between the helium and neon discharges is bigger than the difference measured for the grounded condition (Figure 4.10). Again, the neon plume exhibits lower temperatures than the helium and a difference of around 2.5ºC was observed for the maximum point. Possibly, the heat generated within the tube due to helium plasma ignition might more easily reach the sensor as a result of its better heat transport.

Comparing Figure 4.10 with Figure 4.14, the temperature difference between grounded and floating mode is much more pronounced for the neon case. This is due to the fact that with 3 mm distance between nozzle and grounded electrode, the helium plume does not reach the surface thus, being less disturbed by it. The X-axis of Figure 4.14 corresponds to the distance from nozzle and the plasma jet schemes on top of the temperature graph clarifies how the device was positioned. Thus, the rapid initial increase in temperature is measured within the plasma plume, where the maximum point coincides with the tip of the jet. Not surprisingly, the neon plume is longer reaching 3 mm against 2 mm from the helium jet. The temperature increase rate also differs for both feed gases, where the helium jet, with an increase of nearly 1 ºC/mm, has the double temperature increase rate than the neon jet. In addition, after reaching the end of the plasma plume, the temperature drops quickly for both gases.

Figure 4.14: Temperature measurements comparison for both feed gases on the floating plasma jet. Plasma jets schemes represent the position for measurement acquisition and the length of each plume.
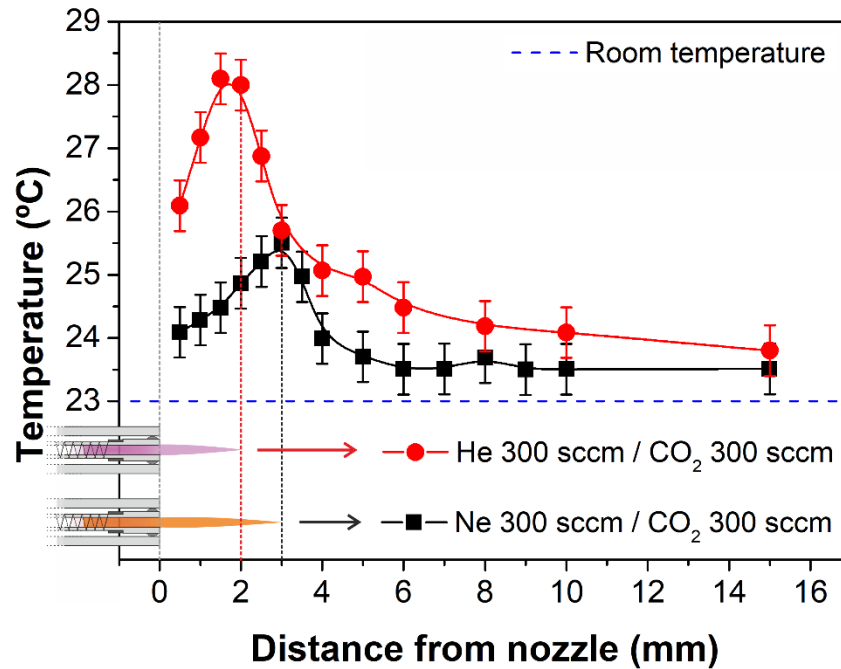
Source: Author's illustration

Formerly, it was demonstrated that the neon plasma jet exhibits some better qualities than the helium jet. Although they have similar characteristics, the neon discharge showed to be slightly colder and achieve a wider range of power values. Although longer, the neon plume is less influenced by the shielding gas with CO_2, presented by the OES spectra in Figure 4.11 (c,d). In our paper (WINTER et al., 2019), the operation of the plasma endoscope with another power supply compared to the one presented here was studied. The alternative HV generator operates with a frequency of 720 kHz and the voltage signal can be switched on or off by an external clock input – controlling the duty cycle. This second power supply has the current limited by the direct current source. Thus, reducing the leakage current even for distances lower than 3 mm. Indeed, the new HV generator helps diminishing the measured fluoride concentration in plasma treated water to extremely low values. In this cooperation paper with Winter (2019) the microbicide effect of the neon plasma jet against the bacterial species *Pseudomonas aeruginosa* was also studied. The alternative pulsed power supply was more effective than the conventional one used here reaching almost 6 log of bacterial load reduction when 0.3% of O_2 is added to the feed gas (WINTER et al. 2019).

4.2 LONG TUBE JET (UNESP)

4.2.1 Parallel plates configuration

The long tube jet developed at Unesp has two different versions. The parallel plate configuration allows the variation of system parameters. Thus, it is possible to investigate how the resulting plume is affected by the primary discharge.

4.2.1.1 Influence of gas flow variation

As mentioned before in section 2.1, one way to generate plasma in laboratory is by applying high voltage (DC, AC, RF or pulsed) to a metal electrode. For DBDs, the simpler way to ignite plasma is by connecting the electrode to a sinusoidal voltage signal. At first, the long tube jet with parallel plates configuration was connected to the same power supply used for the plasma endoscope (section 4.1), working with helium at a frequency of 14.2 kHz and reaching up to 4.6 kV of voltage amplitude. Even for higher gas flow values, the plume only ignites at a voltage of 4.5 kV when a covered grounded electrode is placed 4 mm underneath. Figure 4.15 shows the plasma jet appearance when different gas flow rates are used. With only 0.5 slm the plasma plume already reaches the counter-electrode. Further increasing the gas flow leads to an enlargement of the plume width and the spreading over the surface. It is important to emphasise that for all gas flow rate values no plasma generation is observed along the tube, only at the primary reactor and the resulting plasma jet.

Figure 4.15: Photographs of the plasma jet for different applied gas flow rates. The distance to ground was set to 4 mm and the voltage amplitude of 4.5 kV.
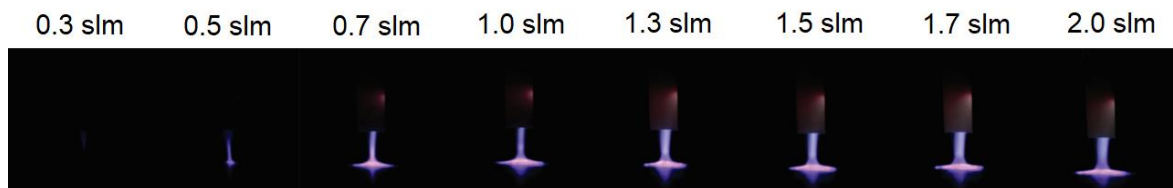
Source: Author's illustration

Since the plasma jet operates at the power supply upper limit, it is not possible here to check the influence of input voltage in the measured transferred charge. Thus, the applied voltage of 4.5 kV is used for all experiments with "continuous mode". Besides the input voltage,

distance and gas flow can also influence the resulting plasma power. The voltage and current signals for the plasma jet positioned with a distance of 4 mm to the counter-electrode is shown in Figure 4.16 (a). Current signals of helium APPJ are characterized by two main peaks (KARAKAS; AKMAN; LAROUSSI, 2012, MCKAY et al., 2013). One short and broad peak in the negative voltage half cycle and a sharper and more pronounced peak in the positive half cycle, as can be observed in Figure 4.16 (a). For this same distance the measured discharge power was measured and is presented in Figure 4.16 (b). It is clear that the power tends to increase with the gas flow rate, reaching a saturation after 1.0 slm. Over 1.5 slm slight decreasing tendency of power can be observed. This can be associated to a probable gas flow transition from laminar to turbulent mode. Giving the dimensions of this plasma jet device, the achieved maximum power was quite low, around 0.7 W. It is important to consider that the measured power at the counter-electrode is equivalent to an association between primary discharge and plasma jet. Thus, the power related only to the plasma plume is even lower. Further investigations concerning the power distribution within the device is presented in section 4.2.2.1.

Figure 4.16: Electrical characterization of the long tube plasma jet with parallel plates configuration at a distance of 4 mm from the grounded electrode. (a) Voltage and current signals and (b) discharge power measurements for different helium gas flow rates.

(a)　　　　　　　　　　　　　　　　　(b)
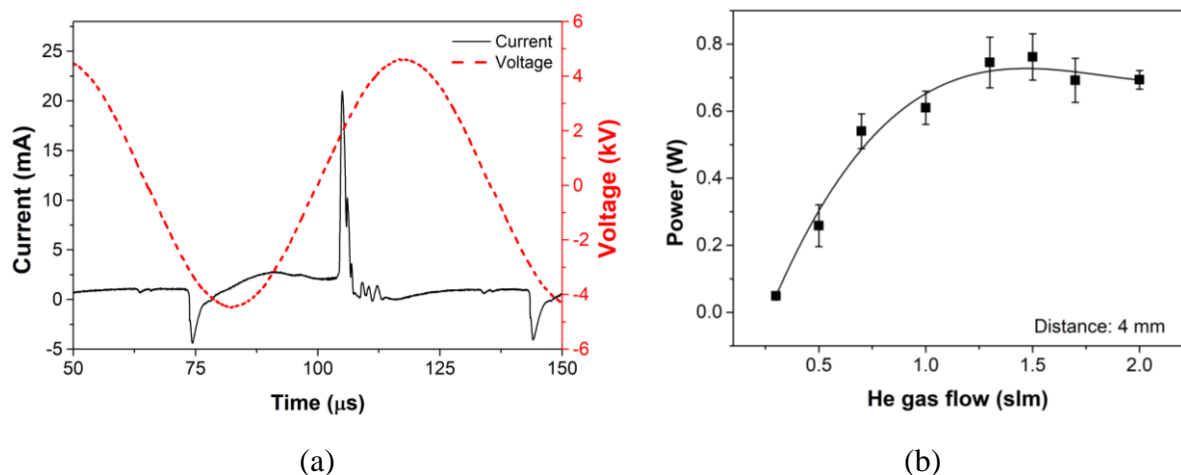
Source: Author's illustration

Besides influencing the plasma jet power, the gas flow is important to cool down the discharge gas. To investigate the cooling effect of the gas flow, a temperature probe was placed 1 mm above the grounded surface to scan the plume and detect the maximum temperature region. The obtained values are displayed in Figure 4.17, where the biggest one corresponds to

the smallest gas flow rate applied, 0.3 slm. For this gas flow rate the temperature is relatively high, reaching almost 43ºC. The plasma plume temperature drops approximately linearly with increase of helium gas flow in the studied region decreasing to around 38ºC, as shown in Figure 4.17. Therefore, the temperature can be controlled by the gas flow. However, for the given parameters, the temperature is relatively close to the upper biological limit of 43ºC presented by Dewhirst (2003).

Figure 4.17: Linear dependence of the plasma plume temperature with gas flow rate.
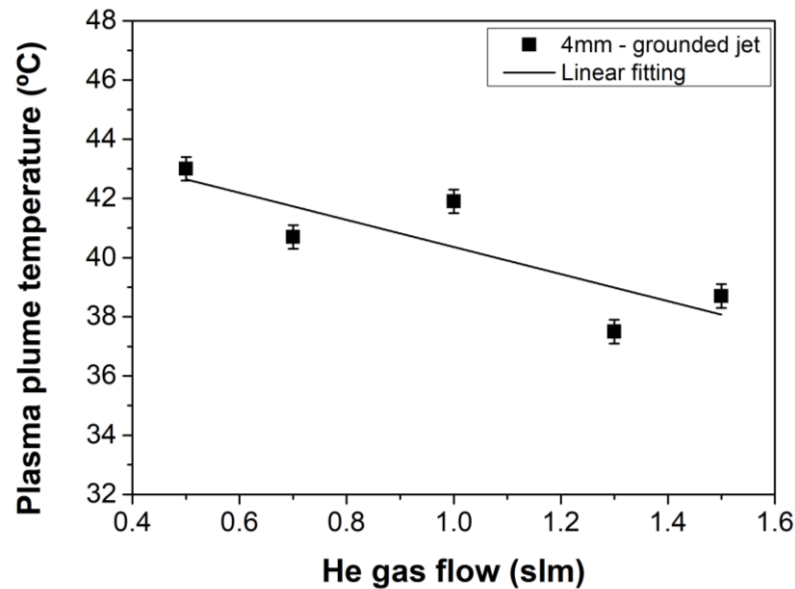
Source: Author's illustration

When expelled from the device, the plasma plume interacts with ambient air ionizing and/or exciting its molecules. The gas flow is an important factor responsible for driving the plasma to the outside region. Besides influencing the plume length, the gas flow rate can alter the flow regime changing the amount of surrounding ambient air mixing within the feed gas. OES was used to investigate if small increase of helium gas flow can decrease such interaction. Figure 4.18 presents the emissions of the main observed excited species detected by OES along the plume length where the point zero corresponds to the tube nozzle. Only the most intense peaks of each specie were tracked along the plume, by instance the OH band at 308.9 nm, the second positive system band of N_2 at 337.1 nm, the first negative system band (N_2^+) at 391 nm, the He line at 706.5 nm and the atomic oxygen emission line at 777 nm. This investigation was performed for 1.0 slm – Figure 4.18 (a) – and 1.5 slm – Figure 4.18 (b). For both gas flow rates, the intensity of all analysed peaks slowly increases from the nozzle until achieving maximum value and then abruptly dropping down. The intensity of the two nitrogen bands rapidly

increases reaching the maximum around 2.5 mm distant from the nozzle and dropping promptly to zero before the counter-electrode position. The same intensity of the first negative system band peak is observed for both He gas flow rates. This indicates the production of excited nitrogen molecular ions (N_2^+) by Penning ionization through He metastable species interactions, suggesting that the He (2^3S) metastable state density is bigger some mm away from the tube tip. Cadot et al. (2014) observed a similar trend, where a maximum He metastable density is observed at 13 mm distance from the nozzle. Furthermore, this group detected that the He metastable density distribution has initially annular shape that in less than 100 ns collapses into a Gaussian. The observed similar intensity of N_2^+ for both conditions implies that the gas flow rate does not seem to influence the ionization behaviour, leading to similar Penning ionization rates. However, the intensity of excited N_2 species decrease when the He flow rises, suggesting a smaller mixing effect in the plasma plume.

Similarly (only slightly shifted) to the above-mentioned species, the peak intensities of He and atomic oxygen reach the maximum at around 3.0 mm. Comparing Figures 4.18 (a) and (b), one can notice a small increase in excited He line intensity, while O remains unaltered. The OH species can be better observed in the magnification graphs in the right-hand side of Figure 4.18 pointed by the arrows. Even at the tube tip, excited OH can be detected although with small intensities which appear to be constant until the nitrogen bands peaks reach their maximum, and quickly going to zero afterwards. By increasing the gas flow, its intensity slightly decreases implying that OH originates mainly from the humid ambient air dragged into the plasma effluent region. It is important to highlight that the maximum intensities are observed shortly above the grounded surface. Therefore, this intensity increase probably corresponds to the region where the plasma column starts to enlarge for spreading over the surface.

Figure 4.18: Intensity of excited species obtained by OES along the plume axis for (a) 1.0 slm and (b) 1.5 slm. The right-hand side graphs are magnifications of the less intense peaks of OH, He and O.

(a)

(b)
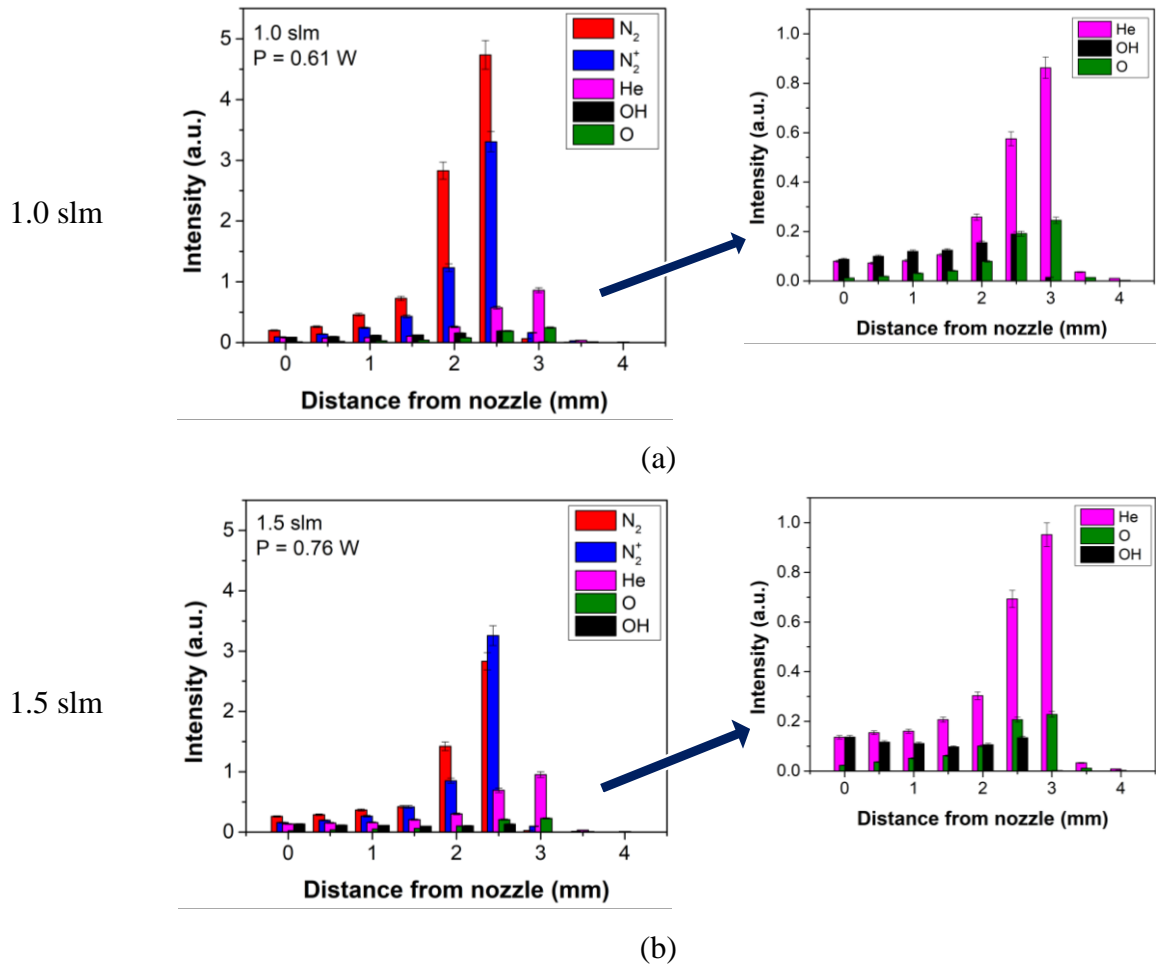
Source: Author's illustration

Focusing in two regions of the plasma plume, slightly under the tube tip (nozzle region) and 1 mm above the counter-electrode (sample region), OES was performed while varying the gas flow rate. Figure 4.19 presents the intensities of each group of excited species, the same already detailed in Figure 4.18, for both regions. As was observed before, close to the nozzle the intensities of all observed species are really low. It can be observed in Figure 4.19 (a) that for extremely low gas flow – 0.3 slm – no plasma jet is generated and therefore, no emission is detected. Slowly raising the gas flow leads to sudden increase of the N_2 peak and other species related to the diffusion of ambient air into the plasma column, such as OH and N_2^+. From 1.0 slm, the radiation intensities of all species seem to reach saturation, besides He that keeps gradually increasing. On the other hand, the emission intensities at the sample position – Figure 4.19 (b) – are much higher, where N_2 species reach the maximum values at about 0.5 slm of

helium flow. This behaviour suggests that higher gas flow rates hinder the surrounding air to diffuse into the plasma effluent. This is supported by the intensity drop of N_2 and OH with gas flow increase. It can be observed that He and atomic O lines get more intense. Moreover, the N_2^+, that is produced by Penning ionization with He metastable species, has an intensity increase until 1.3 slm after which it saturates. This reinforces the idea that further increasing the feed gas flow does not lead to a bigger population of He metastable species.

Figure 4.19: Intensity of excited species obtained by OES at (a) nozzle and (b) sample regions for different applied gas flow rates.

(a)　　　　　　　　　　　　　　(b)
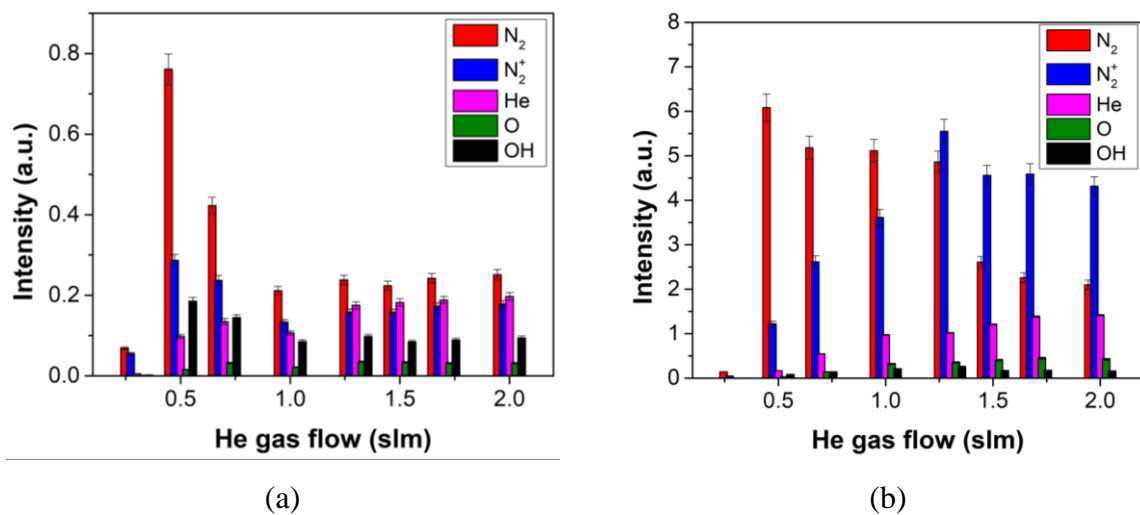
Source: Author's illustration

For many applications investigating the temperature of the floating plasma jet is important, since not always the plume is directed to a conducting surface. In this case, as already mentioned in section 4.1.3, the plasma appearance changes and also the temperature. The plasma plume cross sections were scanned with the temperature probe at different distances from the tube tip. Differently from the observed Gaussian pattern of the grounded jet, the floating plume exhibited a donut shape temperature profile. The 3D image of the scanned cross section at 2 mm distance from the tube nozzle is presented in Figure 4.20 (a). The temperature raises towards the center reaching the maximum within a ring around the central axis. Thereafter, the temperature drops exhibiting a donut shape profile that can be better visualized in Figure 4.20 (b) with the 3D image contour. This feature was observed along the entire length of the plasma plume and thus, it was not considered to be attributed to the presence of the internal floating wire. Therefore, the reason why the gas temperature exhibits such pattern is not fully understood yet. However, it can be possibly related to an annular electron's density distribution causing the gas temperature to rise in this region. Hübner (2014) observed a density

distribution of electrons with donut shape for a DBD-type He plasma jet. This annular distribution was detected close to the nozzle and after that it evolved to an on-axis distribution close to the plume end. Moreover, Hübner's group noticed also that the plasma emission intensity, coming mostly from He and N_2^+ lines, exhibits similar tendency. Nevertheless, for deeper understanding of the phenomenon, further investigations concerning the electrons density distribution and spatial resolution optical emission analysis should be carried out.

Figure 4.20: Temperature profile of the floating plasma jet with gas flow rate of 1.5 slm. (a) 3D image of the scanned cross section at 2 mm exhibiting a donut shape. (b) Image contour for better visualization of the warmer ring region. Each temperature mapping contains 900 measurement points.

(a)   (b)
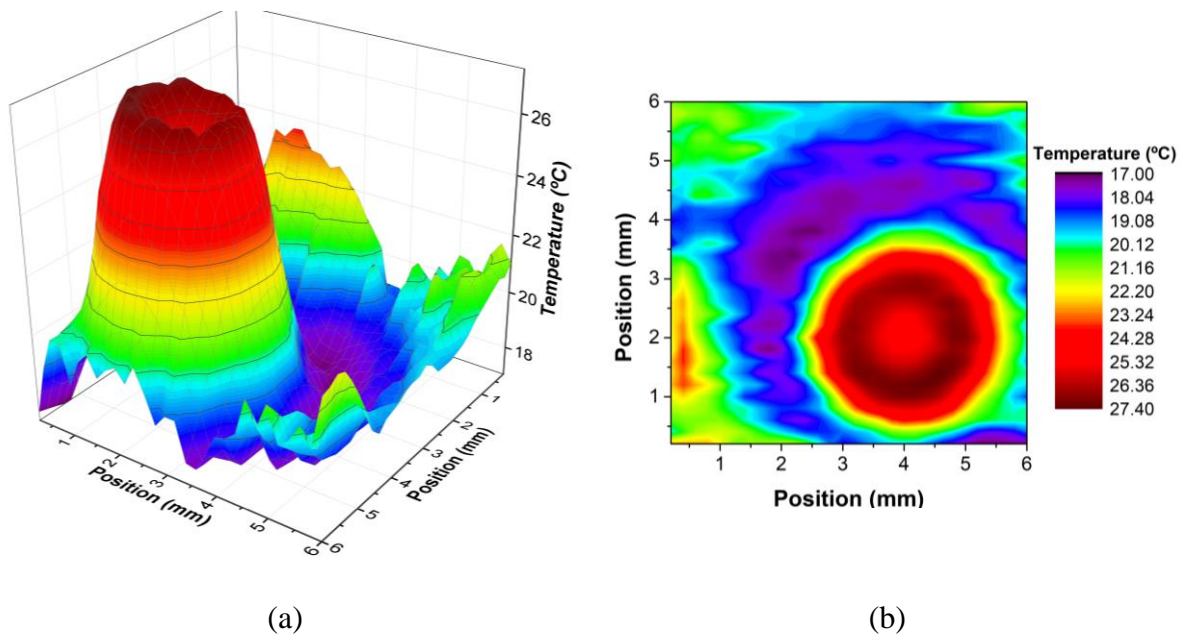
Source: Author's illustration

The temperature at the centermost spot increases with distance until the donut pattern evolves into a Gaussian-like shape at the end of the plasma plume. The temperatures of both regions were measured for different distances from the nozzle when the plasma jet was operated with 1.5 slm of He and the values are displayed in Figure 4.21. It can be observed that the temperature difference between center and ring edges diminishes and after reaching the end of the plasma plume (around 10 mm), only the maximum temperature from the Gaussian-like profile is exhibited. Differently from the plasma endoscope presented in Figure 4.14, the temperature does not drop immediately after the end of the plume. In this case, the temperature values unexpectedly continue rising with the distance until around double the size of the jet (20

mm), after which it saturates and start falling from 45 mm away. If a highest He metastable density is expected close to the plasma plume tip, most of the ionization processes would occur in this region. Thus, presumably, the temperature would tend to increase towards this area. Even though the temperature rises for a long distance, its values are not as high as the ones obtained for the grounded jet. Moreover, the values measured within the plasma plume are below 30ºC.

Figure 4.21: Temperature variation along the plume axis with the two different values (border and center of the donut) assigned. The plasma jet operated with 1.5 slm.
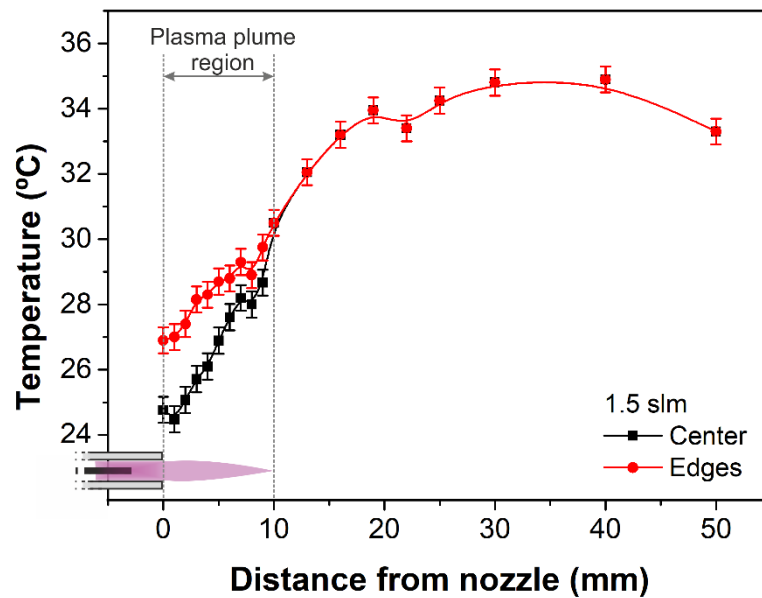
Source: Author's illustration

Besides the previously mentioned (section 4.1.1) biological applications that may require a wide range of power variation, some material treatments can also demand higher or lower discharge power. By instance, thermal sensitive materials like polymers can be damaged when treated with high power. However, more robust objects like metal, ceramics and some composites could be exposed to such conditions. Since this plasma jet is operating at the upper limit of the power supply, one way to vary power, without changing the gas flow, is varying the distance to the counter-electrode. Figure 4.22 (a) presents the discharge power obtained for three different distances between tube tip and the grounded surface. With 4 mm of distance, the power tends to increase with gas flow rate. Highest values of power can be obtained when a distance of 6 mm is set and the gas flow rate is increase beyond 1.0 slm. This increase may arise from a difference in operating regime due to higher gas flow rates. In this case, the jet length for 1.0 slm gas flow can reach the counter-electrode intensifying the charge transfer increasing the power. Possibly, at shorter distances and higher gas flow rates, the discharge is perturbed

by the reflected flow from the target surface. Further increasing the distance to 10 mm cause the power values to drastically drop to around 0.2 W for gas flow near 2.0 slm. Figure 4.22 (b) shows images of the plasma plume for 1.3 and 1.5 slm, in which the power obtained for the distance of 6 mm is higher than the power measured for 4 mm. It can be observed a low intense plasma jet formed for 1.5 slm when 10 mm is used. This corresponds to the slight increase in power observed in the blue curve of Figure 4.22 (a).

Figure 4.22: (a) Discharge power variation for different distances between the tube tip and the grounded electrode and different gas flow rates. (b) Pictures of the non-monotonic behaviour of the plume for the three distances for 1.3 and 1.5 slm.

(a)   (b)
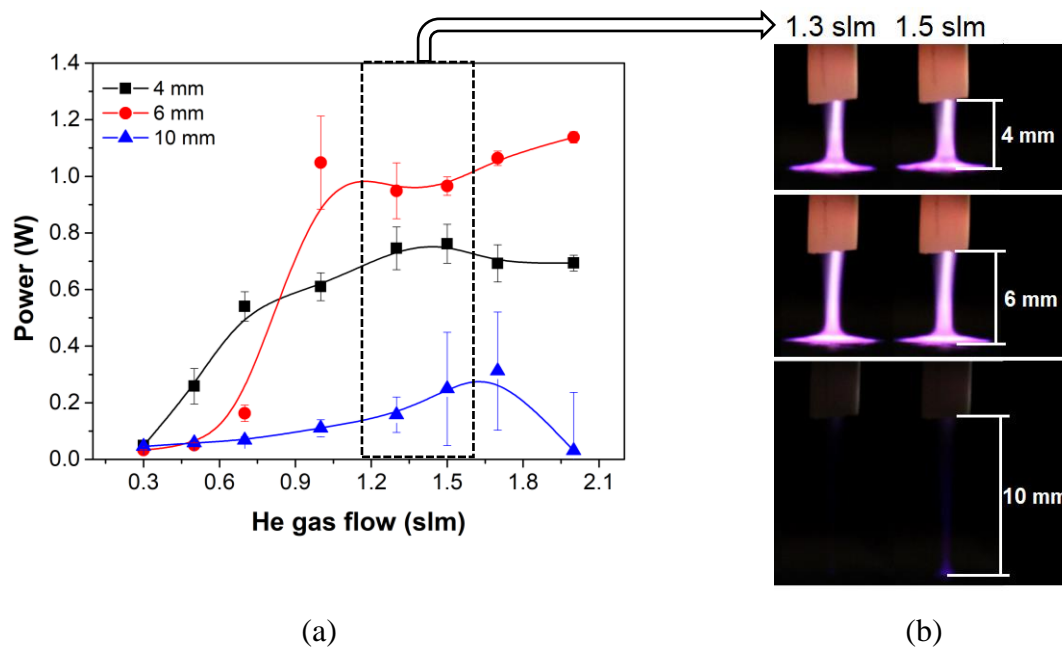
Source: Author's illustration

The higher power values were obtained for 6 mm distance and bigger gas flow rates are in agreement with the current peaks. In Figure 4.23, the current peaks for the three different distances and gas flow of 2.0 slm are presented. As discussed before, helium APPJ current signals are characterized by two main peaks. When gas breakdown occurs, in the positive voltage cycle, the powered electrode acts as an anode and a cathode directed streamer is generated. In this case, positively charged particles are driven towards the cathode while the negative ones are directed to the anode, resulting in the sharp positive current peak observed in the current waveform (MCKAY et al., 2013, KOSTOV et al. 2015a). The plasma bullet in this situation is then produced and sustained by photoionization processes (KARAKAS; AKMAN; LAROUSSI, 2012). When, however, the voltage polarity is inverted, the powered electrode acts

as a cathode and an anode directed streamer takes place. Karakas (2012) concluded that in the negative voltage cycle the secondary electron emission occurs due to charges accumulated on the anode's surface. Thus, the anode directed streamers are maintained by secondary electron avalanches resulting in the negative current peaks. The mechanisms of growth of the two streamers are slightly different and because of divergent charge motion processes and accumulation on the dielectric surface (KOSTOV et al., 2015a). Therefore, the negative and positive current peaks exhibit different amplitude and shapes.

According to Figure 4.23, the negative peaks always occur in the same moment and have their amplitude reduced with the distance increase. This behaviour is in good agreement with the anode directed streamer formation due to charge accumulation. However, the photoionization processes that gives rise to the cathode directed streamers can be sustained for longer distances. Thus, the positive peaks present higher amplitudes, where the 6 mm peak is bigger than the 4 mm in accordance to the power measurements. Some authors associated the positive peaks shift to the plasma bullets propagation (KARAKAS; AKMAN; LAROUSSI, 2012, OH; WALSH; BRADLEY, 2012), once it corresponds to cathode-directed streamer formation explained in section 2.2.3.1. However, the observed peaks shift in this case could not be correlated to plasma bullets movement due to the rather low propagation speed, around 400m/s.

Figure 4.23: Current waveforms for 4, 6 and 10 mm distance and gas flow of 2.0 slm.
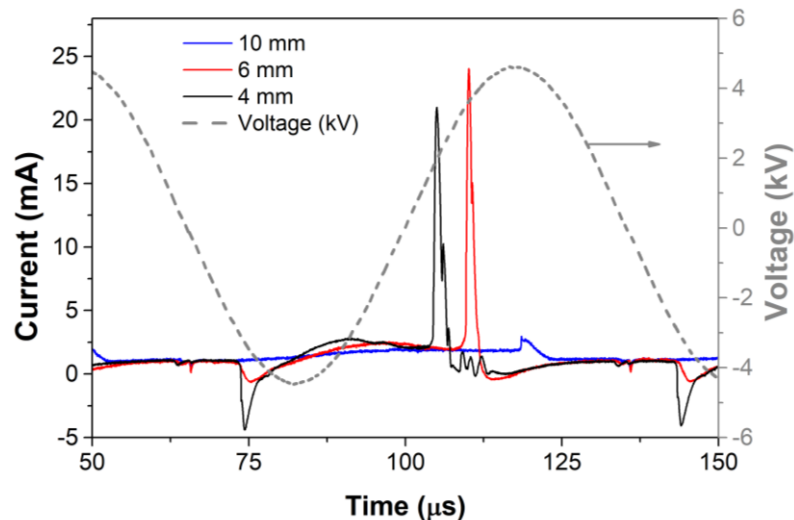
Source: Author's illustration

Even though the power can be slightly controlled by changing the distance, the values achieved with this power source are concentred in a small range – up to 1 W. Thus, it is

important to find alternatives to increase the power variation allowing the precise control of treatment dose according to the desired application. Therefore, a power supply operating in burst mode was employed.

4.2.1.2 Adjustment of discharge power with burst mode

As described in section 2.3.1.2, the power supply operation in burst mode allows a precise control of discharge power. The different voltage signal parameters – such as excitation frequency f, repetition period T_r, number of HV cycles N and voltage amplitude – were varied to investigate how they affect the plasma jet mean power when the jet is placed at a distance of 4 mm to the counter-electrode. The effects of frequency together with repetition period on the power measurements are shown in Figure 4.24. Here, the purple hatched area corresponds to null power (no plasma jet generation). In general, there is only a small region below a repetition period of 2.0 ms for which plasma can be generated given all tested frequencies. For some specific values, such as 25 kHz, 27 kHz and specially between 32 and 34 kHz, peculiar wider working ranges can be observed. Even though the measured powers here do not reach such high values as demonstrated in the coloured scale, the obtained power varies from zero to 4.0 W that is around four times more than the achieved range in continuous mode. Moreover, between 32 and 34 kHz, plasma can be generated for all tested repetition period values. Thus, the operation frequency will be set to 32 kHz for all following investigations and applications.

Figure 4.25 shows the influence of the number of cycles N in comparison to (a) voltage and (b) repetition period T_r on the measured discharge power. In the first graph – Figure 4.25 (a) – the effect of voltage variation on the power values is really pronounced. While for increasing N, the power seems to increase slowly, when voltage and repetition period are kept fixed. For small N (below 5 cycles), the period of plasma on is reduced so much that the measured power is kept around 1 W for all applied voltages. The purple hatched area here also corresponds to the parameters set for which no plasma is produced. Thus, discharge can only be generated from around 9 kV for all tested N values.

Keeping the applied voltage at 10 kV and varying repetition period and N, the power is not much influenced, as can be seen in Figure 4.25 (b). As observed, a reduction of power is expected when the repetition period is increased. Again, for lower numbers of oscillation cycles N, the mean power is very low. When N is increased above 5 cycles, the plasma jet power rises until around 3.0 W, however, this is more pronounced for smaller repetition period values (below 2.0 ms) from which the power only rises when both parameters (N and T_r) are increased

at the same time. Therefore, setting the number of oscillations is not the most important parameter for controlling the power, but can play a role only when adjusted simultaneously with repetition period.

Figure 4.24: Influence of the oscillation frequency in comparison to repetition period on the discharge power. The voltage was fixed in 10 kV, the gas flow was kept in 1.5 slm and were used 10 HV oscillation cycles. Contains 188 measurement conditions.
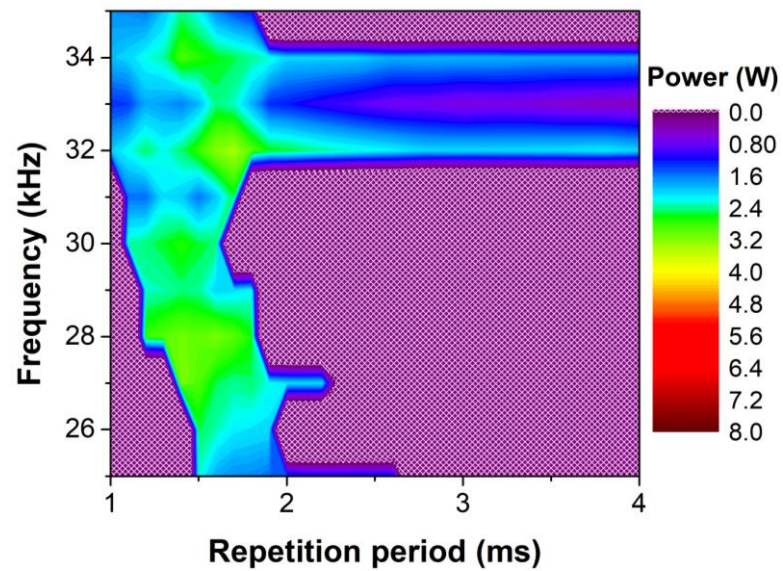
Source: Author's illustration

Figure 4.25: Influence of the number of cycles N against (a) voltage (contains 210 measurement points) and (b) repetition period T_r (contains 160 points) on the discharge power. The frequency was kept at 32 kHz, He flow of 1.5 slm. For (a) the repetition period was 1.5 ms and the voltage amplitude for (b) was 10 kV.
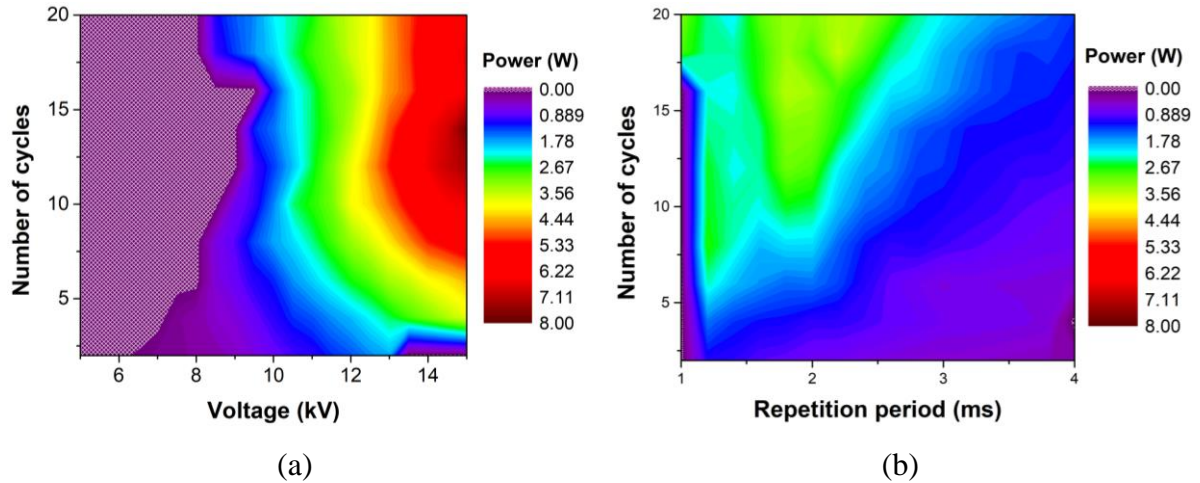
Source: Author's illustration

Keeping, therefore, the repetition period at 1.5 ms – inside the above-mentioned region of higher power values – and the 10 HV oscillations (number of cycles) which results in a repetition frequency of 667 Hz, the power can also be controlled by changing the applied voltage and the gas flow and the result is presented in Figure 4.26. As expected, the discharge power is directly influenced by the voltage amplitude, exhibiting a wide range of power that varies from 0 to 8.0 W. On the other hand, the power does not change much with the gas flow rate. However, the gas flow helps reducing the power when less than 0.5 slm of helium is fed into the system. Therefore, operating the plasma jet in burst mode can efficiently increase the achievable power range allowing a better control of the treatment dose, since it depends on the discharge power, the treatment time and distance and treated area.

Figure 4.26: Power measurements on the long tube jet for different values of duty cycle and gas flow rates. The repetition period was kept in 1.5 ms for a burst of 10 HV cycles. The frequency was 32 kHz. Contains 110 measurement conditions.
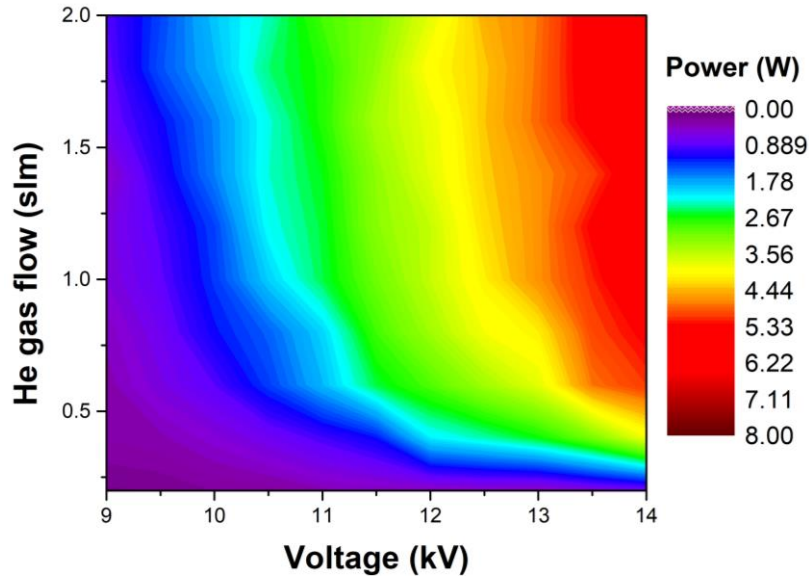
Source: Author's illustration

4.2.1.3 Variation of system parameters

The parallel plates configuration reactor allows the variation of system parameters such as the gap between electrodes and the presence or not of different dielectric materials. In this section, some parameters were varied in order to investigate how the primary discharge influences the resulting plasma jet and the power was measured for a distance of 4 mm between tube tip and the grounded electrode. For those tests, the frequency was kept in 32 kHz, voltage amplitude of 10 kV with 10 cycles and repetition period of 1.5 ms, resulting in 22% of duty cycle. The gas flow was set to 1.5 slm for all experiments in this section. First, it is important to study if the position in which the floating wire is placed inside the discharge influences the total power. In other words, analyse how the power values change if the gap between HV electrode (covered with Delrin®) and the floating electrode is altered. In this case, no dielectric is placed on top of the floating electrode. Figure 4.27 presents the power values for different gap distances and for two copper wire diameters (floating electrode). The power drops when the gap is increased. However, only a small power difference (less than 20%) is observed between the minimum and maximum possible distances. Thus, even though bigger gaps can lead to a reduction of power, the difference is not so pronounced. It can also be noticed in Figure 4.27 that the power values obtained for both wire thickness are very similar and both curves

presented approximately the same trend. Therefore, the wire thickness does not seem to play an important role in the plasma jet power. Certainly, if it would be increased too much compared to the tube dimensions, the gas flow dynamics would be influenced and therefore, bigger impact on the discharge power could be expected.

The floating wire is important to avoid the discharge ignition along the tube (KOSTOV et al., 2015c, ROBERT et al., 2009). Without it, plasma can be observed through the whole length, increasing the total discharge power and eroding the inner part of the tube.

Figure 4.27: Discharge power variation for different gap distances and two floating wire thickness.
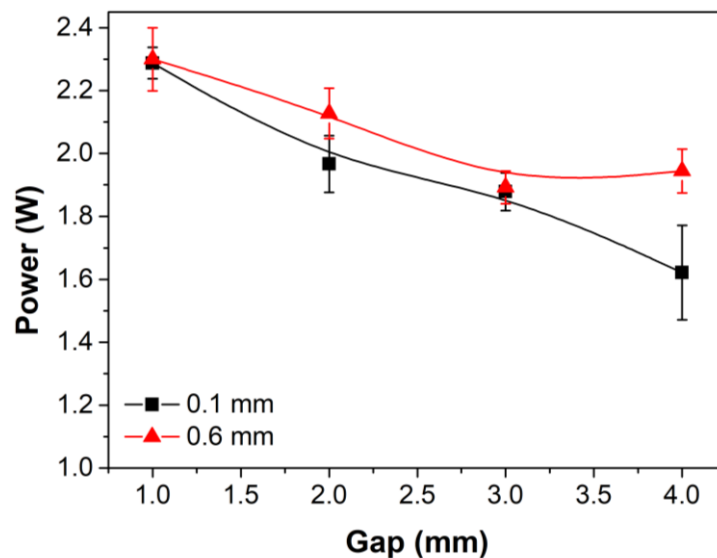
Source: Author's illustration

Another possible investigation concerning the primary discharge is the use of a dielectric barrier on top of the floating disk (connected to the long wire). The plasma jet configuration already accounts with a Delrin® enclosure that isolates the entire HV electrode. The disk connected to the floating wire is located as shown in Figure 4.28 (a). Small pieces of dielectric material were glued on top of the metal disk in a way that the holes for the gas were not blocked. Three different materials with several thickness were used (Delrin®, alumina and glass) maintaining a total gap of 4 mm. The mean discharge power values obtained when different dielectrics were used are presented in Figure 4.28 (b). For each material the power seems to keep approximately constant regardless the thickness. The small power values fluctuations are in the range of around 0.1 W and therefore, can be considered negligible. In addition, the use of different dielectric materials led to similar power values between 1.8 and 2.0 W. Thus, no

significant difference in power was observed when distinct dielectric materials were used in the system. Furthermore, the same power value of around 1.8 W was obtained when no dielectric is used on top of the floating electrode. Therefore, changes regarding the floating electrode seem to be of minor importance and have little effect on the measured power.

Figure 4.28: Effect on the power values of the use of different dielectric materials with various thickness on top of the floating electrode. (a) Picture of the floating metal disk where the dielectric plates are placed and (b) discharge power as a function of the dielectric thickness.

(a)   (b)
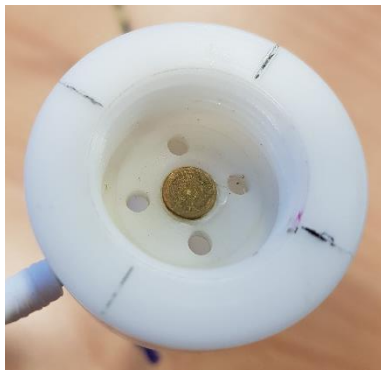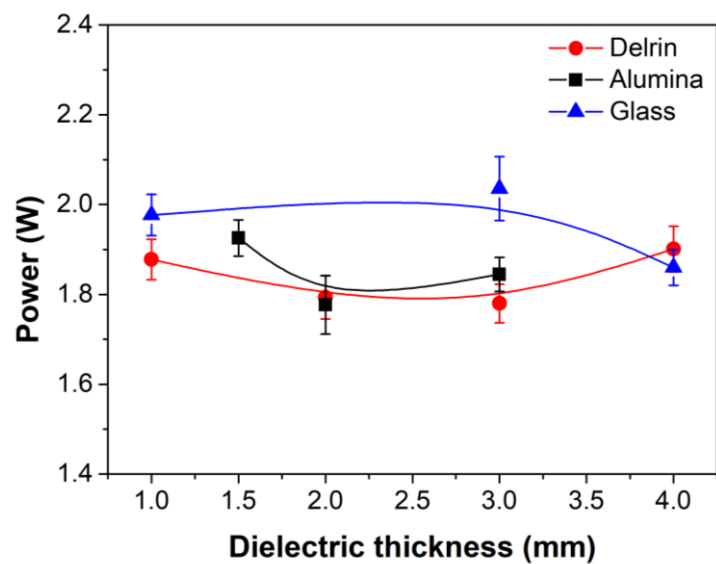
Source: Author's illustration

The tested variation of system parameters did not lead to major changes in power values. Only the increase of the gap distance can slightly reduce the power. The diameter of the floating disk was also varied (data not shown), however, it did not affect the mean power of the discharge. Thus, in general, big changes in the resulting plasma jet are not expected when the primary reactor configuration is modified. Evidently, if the discharge volume is bigger due to changes in the primary reactor geometry, the total power will also increase.

In their paper, Kostov and coauthors (2015c) studied the transfer of an argon discharge through a long plastic tube with a floating metal wire. The same experimental setup presented in section 3.1.2.2 (pin electrode configuration) was used, but different discharge parameters were chosen. Even though they studied a different discharge and therefore values cannot be compared, a parallel can be drawn concerning the obtained investigation trends. In their work,

the variation of voltage on the floating metal wire and power were investigated when different lengths of flexible plastic tube were used. Steep linear drop of wire voltage was observed within the first meter of tube length, after which the voltage continued decreasing linearly (with different slope) (KOSTOV et al., 2015c). The voltage was measured until 4 m tube length, after what plasma jet cannot be ignited anymore. The author described that for long tubes it gets increasingly difficult to ignite a plasma jet at the end of the tube, and the optimum tube length was between 1 and 2 m long. The measured power rapidly decreases in the first decimetres and gradually drops when the tube is made longer, thus decreasing the risk of electric shock (KOSTOV et al., 2015c). Therefore, the flexible tube length can be set according to the desired application and can be increased up to few meters.

4.2.2 Long tube jet applications – Pin electrode configuration

The plasma jet's primary reactor in this section is the same used for biomedical applications in previous works (BORGES et al., 2017, KOSTOV et al., 2015b, NISHIME et al., 2016) and master dissertation (NISHIME, 2015). As presented in the previous section, the primary discharge geometry does not play an important role regarding the measured discharge power. Thus, a long plastic tube with inner floating wire was adapted to the nozzle of this pre-existing plasma jet. Here, the wire tip is placed freely inside the primary discharge region. This plasma jet was only operated in burst mode and was more focused for applications in two different fields: fungi inhibition and material surface modification.

4.2.2.1 Discharge characterization

According to section 4.2.1.2 the best frequency values are between 32 and 34 kHz, since a much wider working range is provided. Assuming a similar behaviour for both plasma jets, the pin electrode device connected to the same power supply used for the burst mode in previous sections, was here operated with a signal frequency of 32 kHz. The amplitude voltage was set to 14 kV with the signal modulated with a frequency of 667 Hz, which corresponds to a repetition period of 1.5 ms. In general, the duty cycle was set to 22% (corresponds to same conditions from Figure 4.26 at 14 kV), only in one set of experiments the duty cycle was varied by changing the number of high voltage oscillations N while the other parameters are kept constant. The waveform of modulated voltage signal was already presented for such parameters (duty cycle of 22%) in Figure 2.11 of section 2.3.1.2 about the use of burst mode.

Typically, the helium discharge current for a plasma jet is composed by two current peaks. Their occurrence is described by streamers formation mechanisms that were already discussed in section 4.2.1.1 in Figure 4.23 for the continuous mode. The current signal for this plasma jet operating in the above-mentioned parameters was obtained by grounding the counter-electrode through a low inductance resistor of 100 Ω and the waveform is presented in Figure 4.29. The two current peaks occurring on the rising and falling parts of the sinusoidal voltage can be clearly observed. The difference here is the superposition of the current signal with a large capacitive current.

Figure 4.29: Applied voltage and discharge current waveforms recorded into the HV on region of the modulated signal for a gas flow of 2.0 slm.
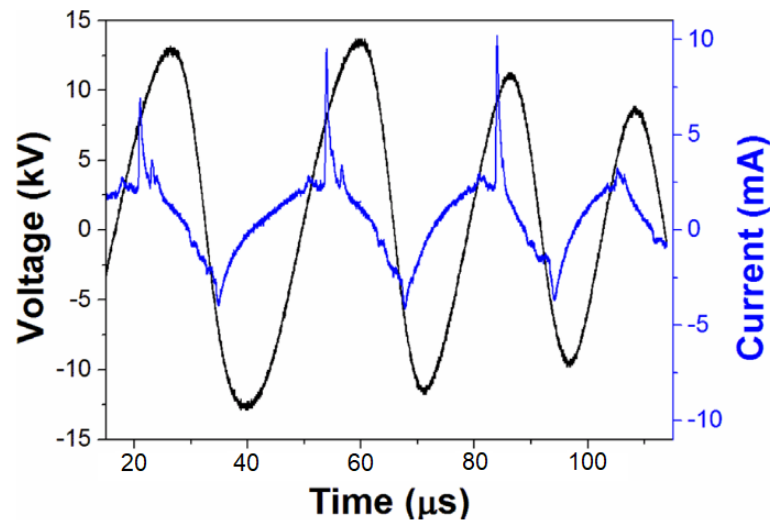
Source: Kostov et al. (2015a)

The plasma jet power can be calculated in the same way done previously, by the Lissajous figure method. All power values presented before for the long tube plasma jet corresponded to the total measured discharge power, that means, the power correspondent to both discharge regions. Considering that the whole device is composed by primary discharge and plasma plume, it is expected that only a fraction of the total power is delivered to the substrate. In order to determine how the total power is distributed into the two discharge regions, the power was acquired in two steps. First, the total power was measured when both discharges were on (as in all other previous cases). Then, the plasma jet was extinguished and only the power corresponding to the primary discharge could be measured. This was accomplished by introducing a small amount of air – around 0.2 slm – into the plastic tube by a secondary input while all other parameters were kept constant. Presence of a molecular gas greatly reduces the

mean electron energy in the discharge due to excitation of rotational and vibrational levels. Thus, introducing air into the tube with helium flow reduce the frequency of ionization by electron impact avoiding the plasma jet ignition (KOSTOV et al., 2015a). The plasma emission in the primary region was monitored while air was gradually introduced into the tube. The injection of 0.2 slm of air in the tube did not affect the plasma emission from the primary discharge. After the air injection, the spectrum from the primary discharge exhibited only characteristic He emission lines and no additional peaks were observed. Thus, it can be considered that the small amount of air introduced in the tube does not disturb the primary DBD discharge.

After the plasma jet elimination by this method, the measured power corresponds to the primary DBD discharge alone. Therefore, having the total power – from both discharges in series – and the power correspondent only to the primary DBD, the mean discharge power transferred by the plasma jet alone can be determined. To illustrate such approach, Figure 4.30 exhibits two Lissajous figures for one voltage cycle in two different conditions. The first figure, depicted by solid symbols, represents the transferred charge by both discharges operating in series. The second, defined by hollow symbols, corresponds to the primary discharge alone. These measurements were performed for a distance of 15 mm to the grounded platform. The area difference of two Lissajous figures represents the energy consumed only by the plasma jet for one cycle of the applied voltage. Accordingly, the calculated mean power was 1.3 W for the both discharges in series and 0.4 W for the DBD discharge alone. Thus, the power of the plasma jet alone was approximately 0.9 W, which means that only about two thirds of the total measured power was actually transferred to the substrate. When the discharge parameters, such as, voltage amplitude, duty cycle, gas flow rate and distance to counter-electrode were varied (data not shown), the ratio between transferred and total power remained approximately constant between 60% and 65%.

Figure 4.30: Q-V Lissajous figures acquired with and without air flow. The solid symbols curve corresponds to the combination of both discharges in series (no air), while the hollow symbols to the primary discharge operating alone.
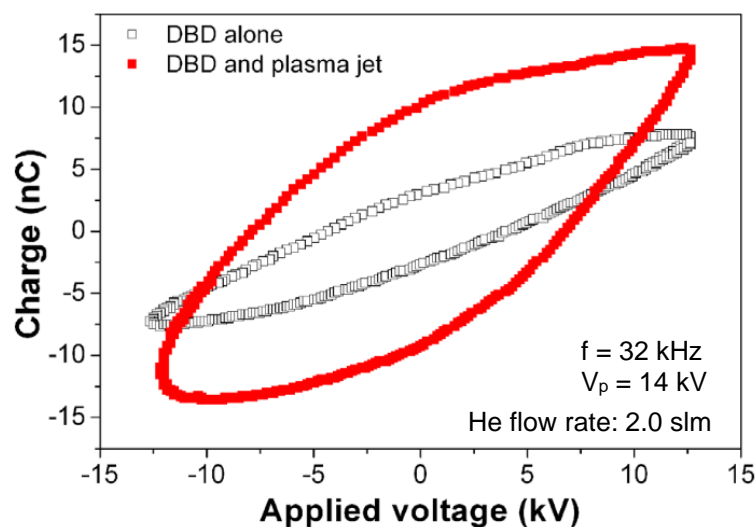
Source: Kostov el al. (2015a)

The microbicide efficiency of the plasma jet without the long plastic tube was already proven in previous studies (KOSTOV et al., 2015a, NISHIME, 2015). The idea behind the new adaptation is to transfer the discharge far from the HV electrode facilitating jet manipulation and allowing a safe use. In order to compare both jet configurations, emission spectra were taken from each of them when generated with same electrical and flow rate parameters. Thus, spectrum of the plasma jet extracted from the primary DBD reactor (when no long tube is adapted) was analysed and compared to the emission of the plasma jet generated at the end of the tube. The acquired spectra are presented for comparison in Figure 4.31, where the upper spectrum (a) corresponds to the plasma jet without the tube elongation and the lower spectrum (b) was measured at the resulting plasma jet from the plastic tube. The plasma jet was operated with same parameters as for Figure 4.30.

Similarly to the previous spectra shown in this study, both spectra in Figure 4.31 (a) and (b) are dominated by second positive system of excited N_2 and first negative system band of N_2^+. Once again, the intense peaks of excited nitrogen ions suggest a big population of He metastable species that are able to ionize nitrogen molecules by Penning ionization. Several helium lines can be observed between 500 and 750 nm and the existence of reactive oxygen species (ROS) are evidenced by two molecular oxygen peaks at 777 and 844 nm. No emissions coming from possible impurities trapped in the tube could be detected. Comparing both spectra, very similar features can be observed suggesting that the plastic tube simply transfers the

plasma jet away from the HV region without visually changing the plasma composition. Thus, it is reasonable to expect that the plasma jet generated at the end of the flexible plastic tube would exhibit similar performance as the plasma jet extracted directly from the primary reactor regarding the decontamination efficiency and surface modification.

Figure 4.31: Emission spectra of two plasma jets: (a) one extracted directly from the primary DBD reactor when no plastic tube elongation is used and (b) the resulting plasma jet at the tip of the long plastic tube.
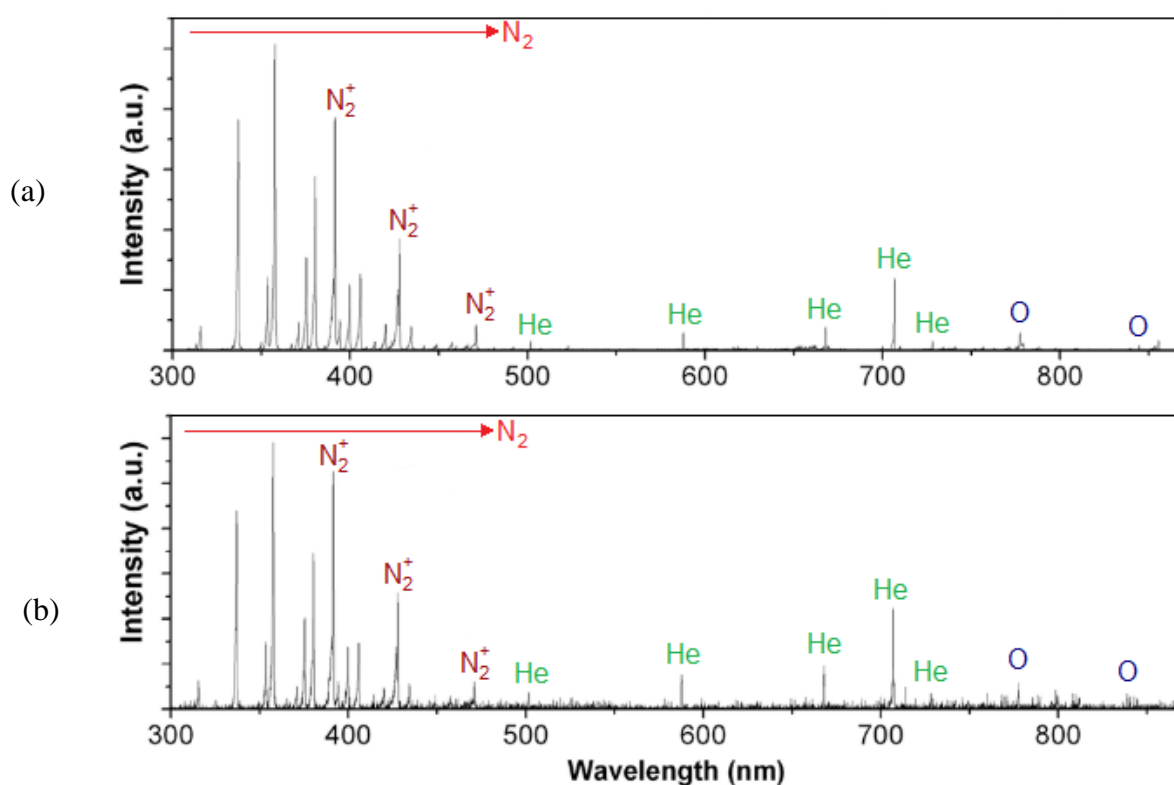
Source: Adapted from Kostov et al. (2015a)

4.2.2.2 Decontamination

The first explored application of the long tube jet with pin electrode configuration was the decontamination efficacy. The plasma jet was directed perpendicularly to an agar plate keeping a distance of 5 mm between the agar surface and the tube tip end. The agar plates were inoculated with *Candida albicans* suspension as described in section 3.3.1. The gas flow was kept in 2.0 slm since in this condition, the plasma plume slightly touched the agar surface. The Petri dishes were placed underneath the plasma jet in pre-defined spots until the desired treatment time was reached. To avoid overlapping of treatment regions, each Petri dish

contained only four spots as shown in Figure 4.32 (a). As control, the plates were exposed to gas flow only, and no inhibition zone was observed in this case. Immediately after treatment, the Petri dishes were incubated for 24h at 37ºC to allow the fungal growth. If the microorganisms are killed by plasma treatment, no colonies growth would be observed in the treated region (inhibition area) which area serves as parameter for evaluation of the plasma jet decontamination efficiency. Due to the short distance, higher gas flow rates were not used in this study because they caused undesired indentations on the agar surface. Moreover, higher gas flow rates can lead to formation of irregular inhibition zones previously reported by Goree (2006) and Nishime (2015, 2016). Therefore, the selected gas flow rate combined with the 5 mm of treatment distance ensured the formation of circular killing spots with well-defined borders – as can be seen in Figure 4.32 (a) – allowing the decontamination efficiency to be evaluated by simply measuring the inhibition zone diameter.

Figure 4.32: Increase of inhibition zone size caused by plasma jet treatment in the (a) Petri dish inoculated with fungal suspension and (b) as a function of the treatment time. The treatment was performed at a distance of 5 mm between tube tip and agar surface.

(a)

(b)
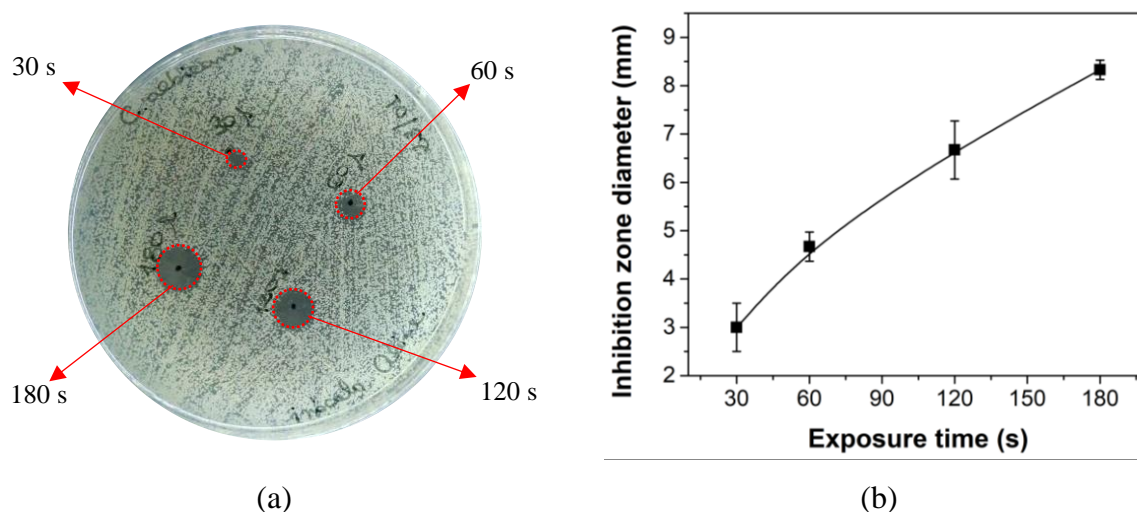
Source: Kostov et al. (2015a)

The variation of inhibition zone diameter is presented as function of the treatment time in Figure 4.32 (b). The size of the inhibition areas gradually increases for the time frame analysed. The maximum inhibition zone diameter achieved was around 8.0 ± 1.0 mm which is already much larger than the plasma jet diameter. Some long-living reactive oxygen species – such as O, OH and O_3 – can propagate radially outwards the plasma column reaching areas much larger than the plasma jet itself (KAWASAKI et al., 2015, KOSTOV et al., 2015b). Some authors

already reported that further increasing the treatment time did not result in larger inhibition zones due to the limited lifetime of the long-living active species (GOREE; LIU; DRAKE, 2006, KOSTOV et al., 2015b). The ROS supposedly play important role in the decontamination process, however the exact mechanisms behind the APPJs microbicide effect of are not fully understood yet. The complex composition of low temperature atmospheric discharges consisting of charged particles, UV radiation and very reactive oxygen and nitrogen species is important for such microbicide effect, in which, these agents individually are known for decontamination capabilities. In case of plasma jets working with helium, the UV photons and the RNS are not expected to play a significant role in this process even though UV is known for causing DNA damage (LU et al., 2008). On the other hand, ROS produced in the plasma jet effluent are highlighted as important agents that cause oxidation of lipids (YUSUPOV et al., 2017) and proteins that constitute cell membranes which can lead to microbial death. Moreover, ROS induced by plasma can pass through outer membranes and act on intracellular components (HAN et al., 2016). Additionally, the microbicide effects of He metastable species and charged particles produced by the ionization fronts could not be fully excluded since they can be driven to the target by the gas flow and the local electric field (KOSTOV et al., 2015a). Therefore, plasma produced species act synergistically enhancing the decontamination efficacy (LACKMANN et al., 2013) and making low temperature plasmas very attractive for such applications. The described action mechanisms are summarized and schematized in Figure 4.33.

Figure 4.33: Non-thermal plasma action mechanisms on microbial inactivation.
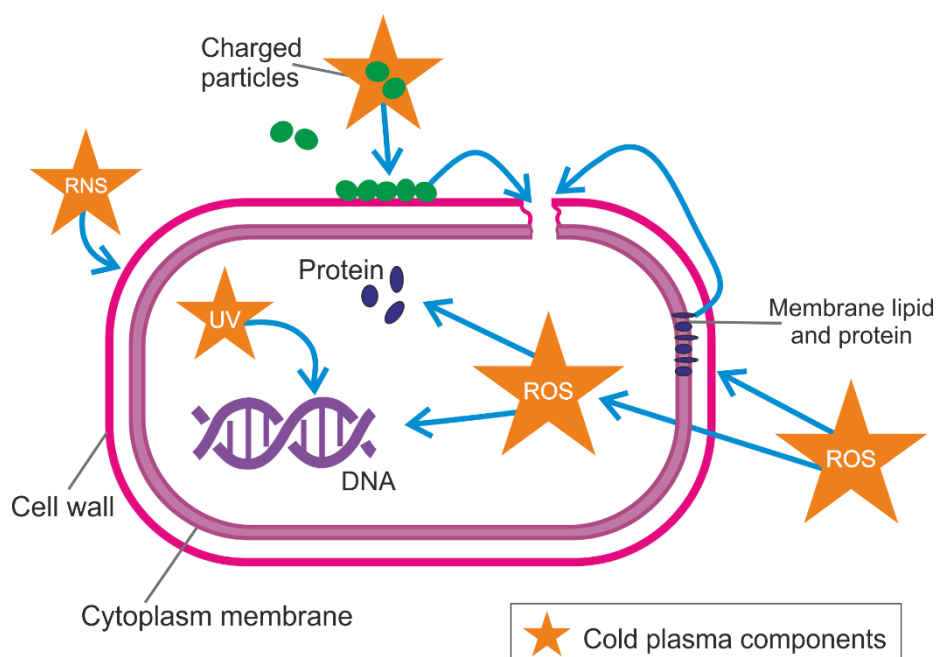
Source: Adapted from Liao et al. (2017)

The precise control of treatment dose is of great importance for mostly every kind of applications. For instance, in plasma medicine, fighting cancer cells or treating of infected lesions, without damaging the surrounding healthy tissue is essential. As previously mentioned, the plasma jet power can be altered by different ways. When using burst mode, the power can be gradually adjusted by changing the duty cycle. Thus, the effect of varying discharge power on the produced inhibition zones was investigated. The mean power was adjusted between 0.5 and 1.6 W by varying the duty cycle of the applied voltage. The time of plasma exposure was kept in 120 s while distance and gas flow rate are kept the same as in Figure 4.32. The inhibition zones diameter in the same strain of *C. albicans* as a function of the discharge power is presented in Figure 4.34. It can be observed that raising the plasma jet power leads to increase of the inhibition zones diameter. When more power is applied, the reactive species necessary for the microbicide effect are generated in higher amounts. However, a saturation of the inhibition regions size was observed when the power was increased above 1.5 W. Thus, similar trend of decontamination efficiency saturation was detected for increase of treatment time or discharge power. Therefore, the delivered energy dose is apparently a very important parameter for microbial decontamination and it can be controlled by either increasing the treatment time or changing the plasma jet mean power.

Figure 4.34: Variation of inhibition zone diameter with increase of the discharge power. The time of plasma exposure was 120s.
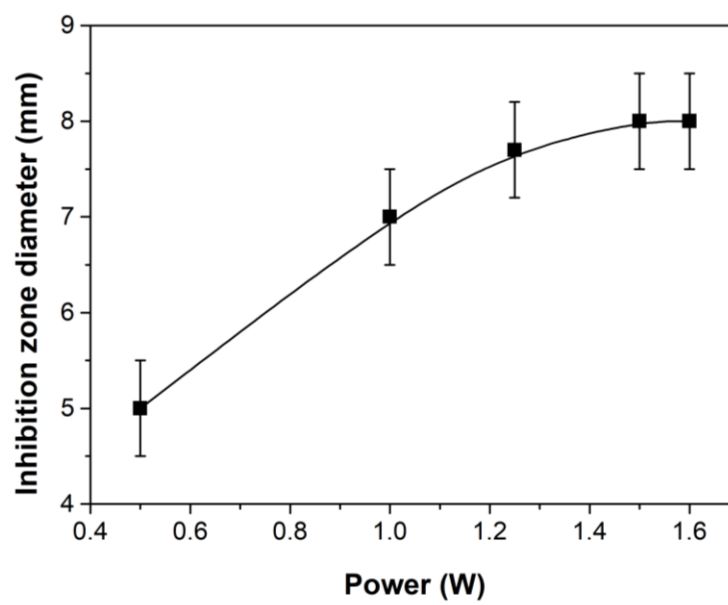
Source: Kostov et al. (2015a)

In previous work, the formation of inhibition zones in Petri dishes plated with the same fungal strain was evaluated (NISHIME et al., 2016). The plasma jet used in this work was the pin electrode primary reactor (as presented here) but without the long tube extension. The results cannot be directly compared since the treatment distances are quite different and consequently, the inhibition zones obtained in the present work are much bigger for the same treatment time. However, the same trend of increase followed by saturation of the inhibition zones was obtained. Additionally, it was shown that decreasing the distance leads to bigger inhibition zones, which is in accordance to the larger areas obtained in this work. As mentioned in the paper, the distance could not be further decreased due to deformations at the agar surface generated by the gas flow. When the tube is attached, the gas velocity at the plasma jet region diminishes because of the bigger tube diameter. Thus, with a smaller gas velocity the long tube allows the plasma jet manipulation closer to the agar surface. Due to the similar decontamination trends obtained with and without the use of the long plastic tube, it is reasonable to assume that the elongation device only transfers the plasma generated in the primary reactor to the tube tip keeping its microbicide characteristic. Therefore, the tube acts as an extension pipe that can be easily bent and manipulated close to the target. Moreover, the tube allows the treatment in regions with difficult access such as teeth and gums.

The studied microorganism (*Candida albicans*) can express virulence features and cause acute and chronic oral infections. In our paper (BORGES et al., 2018), the presented elongated

plasma jet operating in burst mode was studied against oral candidiasis. There, the early stage of *C. albicans* infection in experimentally induced oral candidiasis *in vivo* was evaluated. Before the *in vivo* study, cytotoxicity testing of this plasma jet to Vero cells exhibited cell viability higher than 80% after plasma exposure for 3 and 5 min, which is considered non-cytotoxic according to the ISO 10993 protocol for testing cytotoxicity *in vitro*. As one of the controls, the plasma jet was applied to the tongue epithelium of non-infected mice and no tissue alterations were observed. Borges and coauthors (2018) observed that after 24h plasma was more effective in reducing tissue invasion than the positive control treated with nystatin. Furthermore, the plasma-treated group showed less posterior inflammatory alterations 24h and 48h after treatment compared to the control and nystatin-treated groups. However, in comparison to control no significant reduction in *C. albicans* CFU counts in the plasma-treated group was observed. According to our investigations, the disease occurs as a result of a complex interplay among the expression of candidal virulence factor, the interactions with bacterial microbiome and the immune system of the host (BORGES et al., 2018). Thus, the results presented in the paper point out a promising clinical applicability of this plasma jet.

4.2.2.3 Polymer surface modification

Atmospheric pressure plasma jets are very versatile concerning their applications. Once the plasma is dragged outside the HV-electrode region, it can be easily applied to different target shapes. In addition, it is possible to achieve a punctual application or even homogeneous treatment over large surface when it is scanned with the plume. As presented in the previous section (4.2.2.2), if the plasma jet is kept static on top of a surface, some long-living species generated at the plasma effluent can diffuse radially and interact with the target. Here, the surface modification of a commercial polyethylene terephthalate (PET), when a punctual treatment is performed, was studied.

The main processes that lead to surface modification in polymers by atmospheric pressure plasmas are surface etching, removal of hydrogen atoms from the polymeric chain, cross-linking on the surface and incorporation of polar groups (SHAO et al., 2011). However, during plasma treatment, it is difficult to isolate their effect since the predominance of each respective process may depend on the processing conditions (FRICKE et al., 2012b). The attachment of new radicals generated in the discharge can also lead to modifications on the polymer surface. Chemical changes and roughness modifications alter the material characteristics and change the polymer wettability. Thus, in the present section, only the PET wettability is analyzed and the

changes in static mode water contact angle (WCA) measurements are adopted as surface modification indicative while the plasma jet position configuration is altered.

Samples of PET with 50 x 50 mm size were arranged underneath the plasma jet, which was placed at perpendicular position (forming 90º with the polymer surface). The polymer was treated for 60s with a He gas flow rate of 2.0 slm using the same voltage parameters presented previously for decontamination – voltage amplitude of 14.0 kV, frequency of 32 kHz and duty cycle of 22%. After treatment, the surfaces were analyzed by water contact angle measurements employing a series of droplets with a small distance between them (each 3 mm in the length and each 6 mm in the lateral direction, as schematized by Figure 3.8) until the whole treated surface could be analyzed. Figure 4.35 exhibits the contour map of drop contact angle measured soon after treatment for different distances: (a) 5 mm, (b) 10 mm and (c) 15 mm, where the red color corresponds to the untreated hydrophobic areas. In addition, the treatments were performed in two different substrate regimes: floating and grounded. In the floating regime, the polymer is placed on top of a dielectric platform, while for the grounded condition a grounded metal plate was placed underneath this dielectric. In Figure 4.35 each column corresponds to one treatment regime (left column is floating and right column is grounded) as specified. It can be observed that all modified areas are approximately round, where the major WCA decrease is located in the center slowly increasing radially outwards. Moreover, the treated areas were much larger than the tube diameter (2.5 mm), where a 12 times bigger diameter was obtained for the grounded jet at 5 mm – Figure 4.35 (a) right-hand side. On the other hand, for the biggest tested distance in Figure 4.35 (c) for floating regime, only 4 times bigger diameter was achieved. The most pronounced water contact angle drop was observed for the grounded substrate condition, in which the hydrophilic areas reached WCA around 33º after 60 s of treatment. Besides the lowest contact angle, the grounded jet also appears to lead to a more homogeneous modification. The better results obtained for the grounded condition and shorter distance are related to the bigger treatment dose caused by the increase in power when the discharge is disturbed by the grounded electrode. Moreover, with shorter distances the plasma species can reach the surface faster and act longer, according to its life-time.

Figure 4.35: Water contact angle measurements of PET samples treated for 60 s with a static plasma jet positioned perpendicularly to the surface. The treatment was performed in floating and grounding conditions for distance of (a) 5 mm, (b) 10 mm and (c) 15 mm. Each graph contains 126 measurement points.
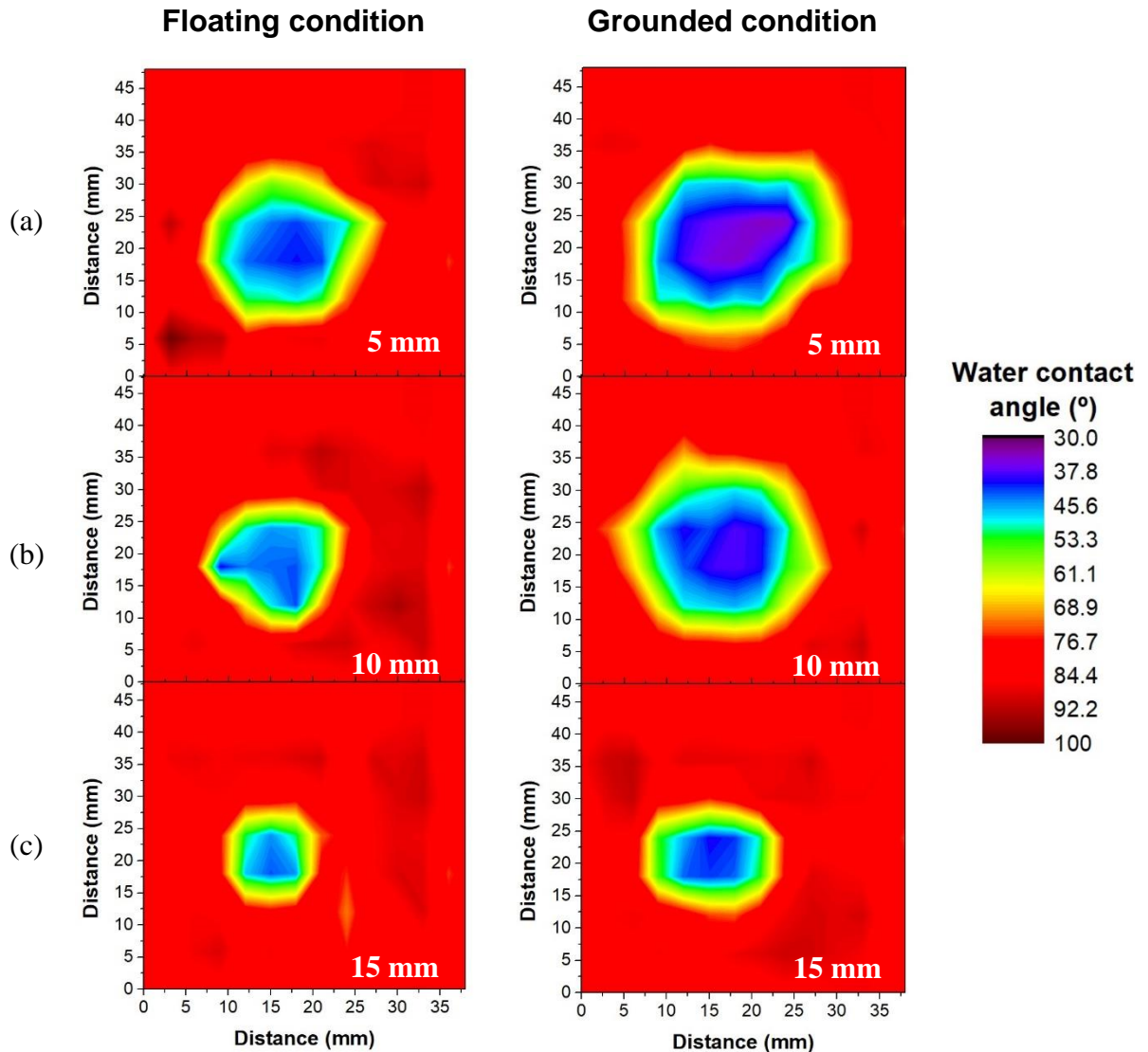
Source: Author's illustration

Commonly, plasma jets are utilized for applications in the perpendicular position, as used for the polymer treatments of Figure 4.35. However, in some cases, for instance in some biomedical applications, a different manipulation of the plume may be required to reach regions of difficult access. Moreover, holding the plasma plume at 90° to perform treatments on the skin is easily achievably but inside the mouth for example, it is not always possible. Besides, for some robust plasma jet devices, tilting operation is not feasible. Thus, the elongation

apparatus presented in this study is a good alternative for those cases, allowing an easy handling of the plasma plume enabling the device to be comfortably and safely bent. Therefore, the treatment of PET samples with the long tube jet (pin electrode configuration) was tested using different tilting angles such as the normal 90º already presented, 45º and parallel to the surface (0º). For the 45º case, the distance between the tube tip and the polymer was kept in 5 mm and the He flow rate was set to 2.0 slm.

Figure 4.36 presents the resulting water contact angle distributions after treatment at 45º. The plasma jet was placed in the middle of the PET sample leaning to the left-hand side of the contour maps. It can be noted that the contact angle values for the grounded condition in Figure 4.36 (a) are lower than the values obtained for the floating configuration – Figure 4.36 (b). Similar to the curve maps achieved for 90º treatments in Figure 4.35, the treated area obtained here for the grounded platform is considerably bigger than the area obtained with floating configuration. However, areas obtained here presented a roughly elliptical shape. Also, the better uniformity of treated areas when a grounded platform is used can be observed for the 45º condition, where the treated region of Figure 4.36 (a) exhibited a smaller eccentricity than the one in Figure 4.36 (b). Moreover, the modified region obtained for the treatment with inclination of 45º and grounded condition showed a 30% bigger area than the one performed perpendicularly, even though both treatments reached similar minimum contact angle value of around 33º after 60 s of exposure to plasma.

Further tilting the plasma jet can also be interesting for some applications. Placing the plasma plume parallel to the polymer surface increases the contact surface area and can help in situations in which the surface needs to be scanned for uniform treatment. In this case, the tube tip was placed parallel to the PET surface but without touching it. Thus, a 2 mm spacer was used to keep the plastic tube slightly above the sample. Figure 4.37 exhibits the water contact angle measurements when no grounded platform was used and 2.0 slm was applied.

Figure 4.36: Water contact angle measurements of PET samples treated for 60 s by the plasma jet placed at an angle of 45º using a (a) grounded platform and (b) only the floating plasma plume. Each graph contains 126 measurement points.

(a) Grounded condition

(b) Floating condition
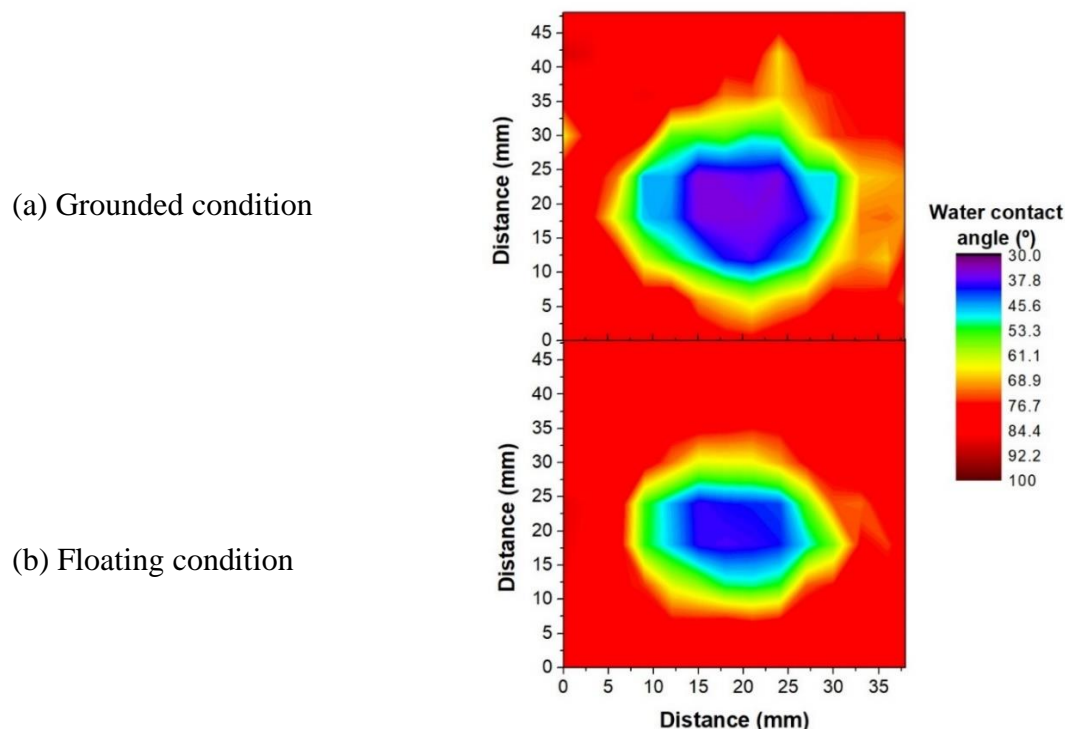
Source: Author's illustration

Figure 4.37: WCA measurement of PET sample treated for 60 s with plasma jet placed parallel to the polymer surface for the floating condition. The position of the plastic tube tip is marked in the WCA map by a black rectangle. The distance to the sample was 2 mm and gas flow of 2.0 slm. A photograph of the plasma plume in such condition is presented. Contains 126 measurement points.
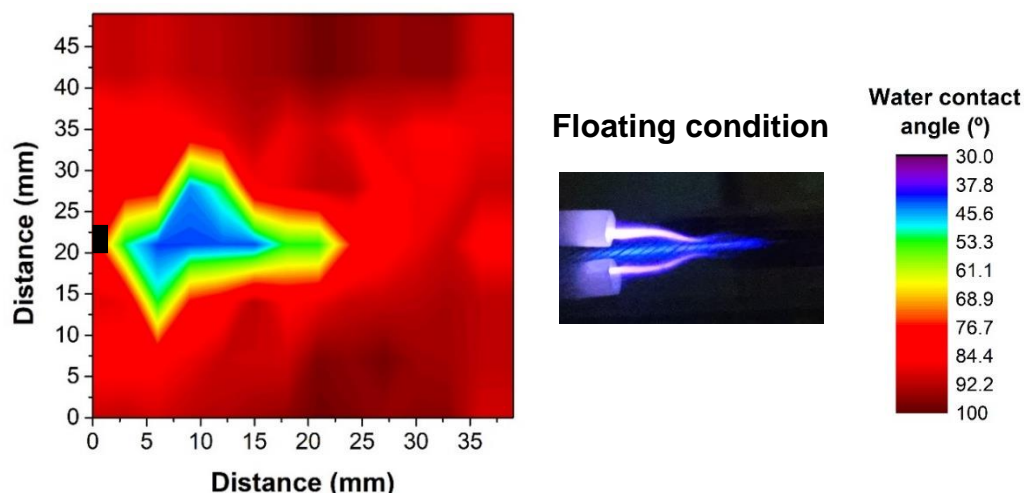
Source: Author's illustration

Next to the contact angle map of Figure 4.37, there is a photograph of the plasma plume in such condition. The plasma jet was placed in the middle of the far left-hand side border of the polymer sample (marked in the WCA map with a black rectangle) and it can be observed in the picture that the plume does not touch the PET surface. In agreement with the preceding results for the floating condition, a non-uniform treatment was obtained. It is clear that the treatment is not homogeneous within the plume region, where a treated length of around 20 mm along the plume was detect but the lateral sides were not equidistantly altered. Therefore, the treatment of PET samples with parallel positioned plasma jet was tested using grounded configuration. Due to the grounded platform, the plasma plume is attracted to the material surface and thus, bigger distances between jet and surface would only lead to less homogeneous treatments. Accordingly, the distance to the surface was kept constant (2 mm) but the gas flow rate was varied from 1.0 to 3.0 slm.

The water contact angle measurements for the grounded condition are presented in Figure 4.38. Each letter in the following figure corresponds to a different He gas flow rate from 1.0 slm (a) to 3.0 slm (e) in ascending order. Combined with the contour maps, pictures of the plasma plume for each condition are shown. Differently from the plume photograph presented in Figure 4.37, it is visible for all pictures of Figure 4.38 that the jet tips are attracted to the grounded platform. Observing Figure 4.38 it is evident that the length of treated areas varies with gas flow. The white dotted line on top of the WCA map points out the treated length for the 1.0 slm condition in comparison to the others. It is clear that the length of modified area increases until the gas flow reaches 2.0 slm (indicated by the dotted black line) after which it starts decreasing but not as much as for the lowest gas flow rate. For pure helium flow, in such conditions, the obtained Reynolds number is quite low due to the small gas density of helium; Rn between 73 and 217 for 1.0 slm and 3.0 slm, respectively. The obtained values are also much lower than the critical Reynolds number of Rn = 2000 that indicates the laminar-turbulent transition (JIN; UHM; CHO, 2013). Thus, the flow is expected to be laminar for all chosen conditions. However, with plasma on, the fluid dynamics changes and a turbulent condition can be much easily achieved. In our paper (WINTER et al., 2018) we observed with shadowgraphy images that a laminar He flow from a plasma jet device can become turbulent when plasma is ignited. Thus, the shortening of the plasma plume length above 2.5 slm can be explained as the transition from laminar to turbulent regimes, which can be noticed by the more diffused plume tip shown in the photographs of Figure 4.38. Moreover, the lowest reached values of contact angle correspond to the laminar conditions: 1.0, 1.5 and 2.0 slm, where a reduction of WCA to almost 30° was obtained.

Figure 4.38: Water contact angle measurement of PET sample treated with plasma jet placed parallel to the polymer surface (at point 0) for the grounded condition and different gas flow rates: (a) 1.0 slm, (b) 1.5 slm, (c) 2.0 slm, (d) 2.5 slm and (e) 3.0 slm. The distance between tube and PET surface was kept in 2 mm. Photographs of the plume in the respective conditions are presented. The white arrow indicates the treatment direction. Each graph contains 126 measurement points.
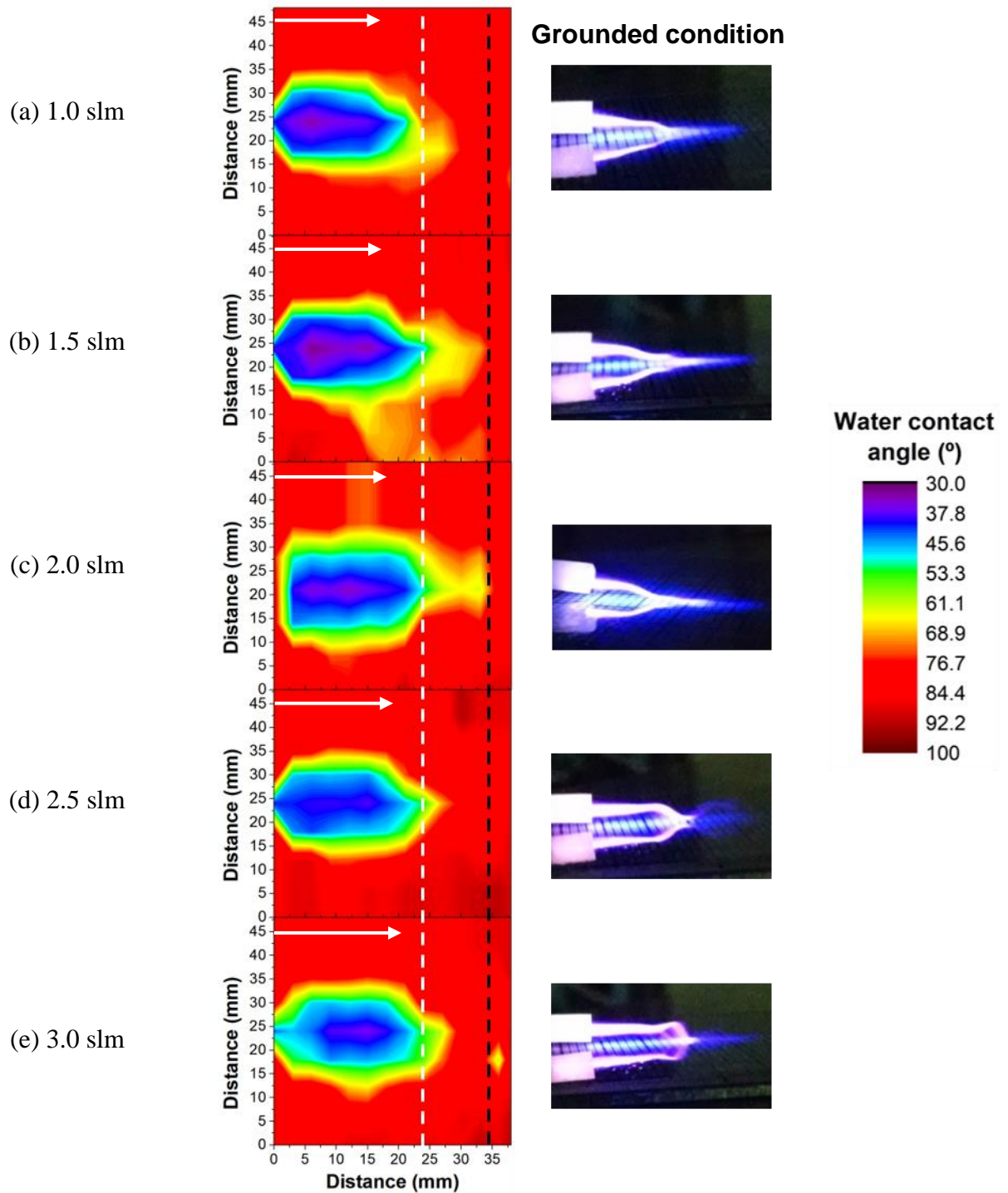
Source: Author's illustration

The five modification areas presented in Figure 4.38 exhibited similar shape. However, the areas obtained for 2.5 and 3.0 slm (turbulent conditions) are slightly bigger than the 1.0 slm case. Even though the turbulent plasma plumes generate bigger modification zones as the 1.0 slm case, the treatment seems to be less efficient once the WCA drop is not so pronounced. The laminar flow conditions presented much larger zones with lower contact angle values. Furthermore, the treated area obtained here for 2.0 slm is 20% bigger than the one achieved for the 90° treatment at the shortest distance. Comparing the three different tilting positions studied for the grounded condition, Figure 4.35 (a) right-hand-side for 90°, Figure 4.36 (a) for 45° and Figure 4.38 (c) for 0°, the increase in treated area can be observed. In this case, a 45° treatment led to the biggest increase in modification area of around 30%. Therefore, tilting the plasma jet when a grounded platform is used seem to enhance the treated area reached.

Another application of this plasma jet was studied by Prysiazhnyi and coauthors (2017). They investigated the use of this long tube jet to modify the inner surface of polymer tubes. In their paper, three different polymeric materials were used: vinyl, polyurethane and silicone. To provide a more uniform plasma distribution inside the tube, an outer coiled grounded electrode was used. Thus, plasma jet and grounded electrode were kept fixed while the treated tube was passed through. Parameters similar to the ones in this section were selected for treatment – voltage amplitude of 14 kV, duty cycle of 22%, but slightly lower frequency of 31 kHz – using argon as feed gas due to its lower cost. With those parameters, tubes with lengths starting from 20 cm could be homogenously treated and a gradual decrease of water contact angle was observed with increase of treatment time. In addition, it was demonstrated that this plasma jet configuration can be applied for homogenous treatment of inner surface of polymer tubes with length up to 1.0 m (PRYSIAZHNYI; SATURNINO; KOSTOV, 2017).

5 CONCLUSION

The development of remote plasma jets is a recent and important step in the plasma jets research field. It allows a better manipulation of the plasma plume improving the sample targeting by plasma species and opening new possibilities in many areas of applications such as endoscopy, odontology and material treatment. However, developing a long plasma jet or a remotely generating device brings difficulties that were explored throughout this study. The development, improvement and characterization of two elongated cold plasma jets have been carried out here first. Aiming a new and promising combination of plasma and an endoscope device, a plasma jet configuration was successfully developed. The device was tested for fulfilling the specific requirements necessary for small configuration dimension, in-body operation and safety operation conditions. Additionally, the possibility of transferring plasma through long plastic tubes by using an inner floating wire was also investigated in the present work. Obstacles concerning the construction of a remotely generated plasma jet for safe *in vivo* treatments were surpassed, until a secure plasma jet operation with low cytotoxicity was obtained.

The first plasma jet, plasma endoscope, was designed to operate inside commercial endoscopes allowing simultaneous diagnosis and treatment. Thus, this plasma jet can be applied for in-body treatments inside hollow organs or regions of difficult access.

Since the plasma endoscope is a long plasma jet device designed for endoscopic applications, it presented specific drawbacks. In this case, the high voltage wire is winded around the tube until the nozzle tip. The wire winding distance is a very important parameter and needs to be made very narrow to avoid formation of parasitic discharges inside the tube. This atmospheric pressure plasma jet can produce small plasma plumes with temperature in the range of 30ºC and maximum discharge power of 160 mW. The working temperature and the discharge mean power can be directly controlled by the input voltage. To ensure its proper operation inside closed cavities, a second shielding gas channel coaxially aligned with the main stream gas tube was arranged. An electronegative gas curtain is important to confine the discharge electrons into the main column avoiding dispersion. Carbon dioxide appeared to be a suitable alternative to air, since its breakdown voltage is higher and no parasitic discharges were observed inside the endoscope tube. The plasma jet worked evenly with helium and neon, however the neon jet ignited at lower input voltages and provided a wider range of power operation.

A comparison of emission spectra obtained with and without CO_2 shielding gas led to the conclusion that the neon jet excitation processes were less affected than helium jet when using the shielding curtain. When operated inside half-closed cavities, the plasma jet can switch between local (plasma plume) and diffuse (glow discharge) modes by controlling the shielding gas flow rate. It was proven by Winter and coauthors (2019) that the use of a HV generator operating in burst mode helps reducing the leakage current of this plasma jet. Using the new power supply, the neon plasma jet proved to be efficient in decontaminating the bacteria *P. aeruginosa*. Thus, the plasma endoscope operating with neon as feed gas and CO_2 as shielding gas connected to the new HV power supply forms a promising combination for operating inside an endoscope and shall be further investigated for future in-body application.

The second source, the long tube plasma jet, is a device capable of generating a remote helium plasma jet by transporting the discharge from a primary reactor to the tube far end. Since it transfers the discharge through a flexible plastic tube, the plasma jet can be easily and safely applied in fields like dermatology, dentistry and material treatment.

When operated with a simple AC power supply, the device produces plasma plumes with low power (below 1.0 W) but with temperatures close to the biological upper limit of 43ºC when operating in grounded conditions. The power can be adjusted by changing either the gas flow rate or the distance between tube end and target. The temperature analysis of the floating plasma plume revealed a donut-shaped temperature distribution along the plasma jet. This singular temperature profile shape can be possibly associated to the annular electron's distributions in the plasma jet. However, further investigations about the electron's density distribution and optical emission analysis with improved spatial resolution should be carried out for better understanding of this phenomenon.

Operating the long tube plasma jet in burst mode allowed the precise adjustment of parameters enabling it to work in special regions with broader range of operation. Thus, the plasma jet power can be better controlled which leads to a more precise management of treatment dose. The role of primary discharge geometry was also investigated and it has been demonstrated that only the penetration distance of the floating metal wire inside the discharge can slightly influence the discharge power.

The long plastic tube device can be adapted to other plasma jet configurations efficiently transferring the discharge to the tube tip end. It was successfully adapted to a pre-existing plasma jet improving its manipulation and allowing a safer use regarding biological applications. The long tube jet was tested against *C. albicans* in agar plates and the area of

inhibition zones was used to evaluate its decontamination efficiency. The size of the inhibition zones depends on the treatment dose, which can be precisely controlled by increasing either the treatment time or the discharge power. Its maximal size is determined by the lifetime of generated species. Since the observed killing zones were much bigger than the tube diameter, it can be concluded that the long-living ROS are the most important agents for decontamination. By means of optical emission spectroscopy and the decontamination efficiency tests, it was proved that the plastic tube elongation acted as a gas channel in which the plasma is only transferred to the other extremity exhibiting similar characteristics to the primary discharge. Thus, the long tube acts as a safe extension device that can be easily bent and manipulated close to the target allowing treatment in regions with difficult access.

Since this tube extension allows fine control of the plasma plume, the treatment of surfaces with tilting positions is made possible. Thus, the effects when the plasma jet is not applied in the conventional perpendicular manner was investigated. The long tube plasma jet has been tested for surface modification of PET with different angling positions. Tilting the plasma jet increased up to 30% the treated areas and more pronounced and homogeneous modified areas were achieved when a grounded platform was used below the target polymer. Additionally, the use of laminar flow conditions also cooperated with improving homogeneity. Thus, the small diameter, the flexibility, the tube biocompatibility and the operation safety (distant from the HV electrode) broadens the field of applications of this plasma jet, making possible a secure treatment of living tissues, in-body procedures or treatment of complex-shaped targets.

REFERENCES

ABOUBAKR, H. A. *et al.* Cold argon-oxygen plasma species oxidize and disintegrate capsid protein of feline calicivirus. **PLoS ONE**, v. 13, n. 3, p. 1-24, 2018.

ALVA R., E. *et al.* Non-thermal plasma for exhaust gases treatment. **Front. Mech. Eng.**, v. 10, n. 3, p. 301-305, 2015.

BÁRDOS, L.; BARÁNKOVÁ, H. Cold atmospheric plasma: sources, processes, and applications. **Thin Solid Films**, v. 518, n. 23, p. 6705-6713, 2010.

BINENBAUM, Y. *et al.* Cold atmospheric plasma, created at the tip of an elongated flexible capillary using low electric current, can slow the progression of Melanoma. **PLoS ONE**, v. 12, n. 1, p. 1-15, 2017.

BITTENCOURT, J. A. **Fundamentals of plasma physics**. Third edit. New York: Springer US, 2004, 678.p.

BORCIA, G; ANDERSON, C A; BROWN, N M D. The surface oxidation of selected polymers using an atmospheric pressure air dielectric barrier discharge. Part II. **Applied Surface Science**, v. 225, p. 186-197, 2004.

BORGES, A. C. *et al.* Amplitude-modulated cold atmospheric pressure plasma jet for treatment of oral candidiasis: *In vivo* study. **PLoS ONE**, v. 13, n. 6, p. 1-19, 2018.

BORGES, A. C. *et al.* Cold atmospheric pressure plasma jet modulates *Candida albicans* virulence traits. **Clinical Plasma Medicine**, v. 7-8, p. 9-15, 2017.

BRANDENBURG, R. Corrigendum: dielectric barrier discharges: progress on plasma sources and on the understanding of regimes and single filaments (2017 Plasma Sources Sci. Technol. 26 053001). **Plasma Sources Science and Technology**, v. 27, n. 7, p. 079501, 2018.

BREATHNACH, R. *et al.* Evaluation of the effectiveness of kINPen Med plasma jet and bioactive agent therapy in a rat model of wound healing. **Biointerphases**, v. 13, n. 5, p. 051002, 2018.

BRUGGEMAN, P. J; IZA, F.; BRANDENBURG, R. Foundations of atmospheric pressure non- equilibrium plasmas. **Plasma Sources Sci. Technol**, v. 26, 2017.

BRUGGEMAN, P. *et al.* Characterization of a direct dc-excited discharge in water by optical emission spectroscopy. **Plasma Sources Science and Technology**, v. 18, n. 2, 2009.

BRULLÉ, L. *et al.* Effects of a non thermal plasma treatment alone or in combination with gemcitabine in a MIA PaCa2-luc orthotopic pancreatic carcinoma model. **PLoS ONE**, v. 7, n. 12, p. 1-10, 2012.

BURÁNY, N.; HUBER, L.; PEJOVIĆ, P. Corona discharge surface treater without high voltage transformer. **IEEE Transactions on Power Electronics**, v. 23, n. 2, p. 993-1002, 2008.

CADOT, G. *et al.* Spatio-temporally resolved mapping of helium metastable density in an atmospheric pressure plasma jet. **IEEE Transactions on Plasma Science**, v. 42, n. 10, p. 2446-2447, 2014.

CAMACHO, J. J. *et al.* Optical emission studies of nitrogen plasma generated by IR CO_2 laser pulses. **Journal of Physics B: Atomic, Molecular and Optical Physics**, v. 40, n. 24, p. 4573-4590, 2007.

CHANG, J.; LAWLESS, P. A.; YAMAMOTO, T. Corona Discharge Processes. **IEEE Transactions on Plasma Science**, v. 19, n. 6, p. 1152-1166, 1991.

CHANG, Z. *et al.* Diagnosis of gas temperature, electron temperature, and electron density in helium atmospheric pressure plasma jet. **Physics of Plasmas**, v. 19, n. 7, p. 073513, 2012.

CHANG, Z. *et al.* Influence of Penning effect on the plasma features in a non-equilibrium atmospheric pressure plasma jet. **Journal of Applied Physics**, v. 115, n. 10, 2014.

CHANG, Z. *et al.* Plasma bullet with hollow structure: Formation and evolution. **Scientific Reports**, v. 8, n. 1, p. 1-10, 2018.

CHENG, K. Y. *et al.* Wound Healing in Streptozotocin-Induced Diabetic Rats Using Atmospheric-Pressure Argon Plasma Jet. **Scientific Reports**, v. 8, n. 1, p. 1-15, 2018.

COBURN, J. W.; CHEN, M. Optical emission spectroscopy of reactive plasmas: A method for correlating emission intensities to reactive particle density. **Journal of Applied Physics**, v. 51, n. 6, p. 3134-3136, 1980.

DAESCHLEIN, G. *et al. In vitro* susceptibility of important skin and wound pathogens against low temperature atmospheric pressure plasma jet (APPJ) and dielectric barrier discharge plasma (DBD). **Plasma Processes and Polymers**, v. 9, n. 4, p. 380-389, 2012.

DAESCHLEIN, G. *et al.* Antibacterial activity of an atmospheric pressure plasma jet against relevant wound pathogens *in vitro* on a simulated wound environment. **Plasma Processes and Polymers**, v. 7, n. 3-4, p. 224-230, 2010.

DEWHIRST, M. W. *et al.* Thermal dose requirement for tissue effect: experimental and clinical findings. **Proc SPIE Int Soc Opt Eng.**, p. 1-35, 2003.

DOWLING, D. P. *et al.* DC pulsed atmospheric-pressure plasma jet image information. **IEEE Transactions on Plasma Science**, v. 39, n. 11 Part 1, p. 2326-2327, 2011.

DOWLING, D. P. *et al.* Influence of dc pulsed atmospheric pressure plasma jet processing conditions on polymer activation. **Plasma Processes and Polymer**, v. 8, p. 718-727, 2011.

EL-DAKROURI, A. *et al.* VUV emission from a novel DBD-based radiation source. **Journal of Physics D-Applied Physics**, v. 35, p. 109-114, 2002.

FANG, Z. *et al.* Polyethylene terephthalate surface modification by filamentary and homogeneous dielectric barrier discharges in air. **IEEE Transactions on Plasma Science**, v. 37, n. 5, p. 659-667, 2009.

FRICKE, K. *et al.* Atmospheric pressure plasma: A high-performance tool for the efficient removal of biofilms. **PLoS ONE**, v. 7, n. 8, p. 1-8, 2012a.

FRICKE, K. *et al.* Investigation of surface etching of poly(ether ether ketone) by atmospheric-pressure plasmas. **IEEE Transactions on Plasma Science**, v. 40, n. 11 PART1, p. 2900–2911, 2012b.

FRIDMAN, A. **Plasma Chemistry**. New York: Cambridge University Press, 2008. 1022 p.

FRIDMAN, A.; FRIEDMAN, G. **Plasma medicine**. Chichester: John Wiley & Sons, 2013. 526 p.

FRIERI, M.; KUMAR, K.; BOUTIN, A. Antibiotic resistance. **Journal of Infection and Public Health**, v. 10, p. 369-378, 2017.

GARG, R. K. *et al.* Gas temperature measurements in a microwave plasma by optical emission spectroscopy under single-wall carbon nanotube growth conditions. **Journal of Physics D:** Applied Physics, v. 41, n. 9, 2008.

GOREE, J; LIU, B.; DRAKE, D. Gas flow dependence for plasma-needle disinfection of *S. mutans* bacteria. **Journal of Physics D:** Applied Physics, v. 39, n. 16, p. 3479-3486, 2006.

GOTOH, K. *et al.* Contamination control of polymer films by two atmospheric pressure plasma jet treatments. **Polymer Journal**, v. 48, p. 889, 2016.

GRINEVICH, V I. *et al.* Application of dielectric barrier discharge for waste water purification. **Plasma Chemistry and Plasma Processing**, v. 31, n. 4, p. 573-583, 2011.

HAN, L. *et al.* Mechanisms of inactivation by high-voltage atmospheric cold plasma differ for Escherichia coli and Staphylococcus aureus. **Applied and Environmental Microbiology**, v. 82, n. 2, p. 450-458, 2016.

HARRY, J. E. **Introduction to Plasma Technology**. Weinheim: WILEY-VCH, 2010. 215 p.

HEINLIN, J. *et al.* Plasma applications in medicine with a special focus on dermatology. **Journal of the European Academy of Dermatology and Venereology**, v. 25, n. 1, p. 1-11, 2011.

HONG, K. H.; OH, S. J.; MOON, S. H. Degradation of pentachlorophenol by ozone generated by a pulsed power corona discharge. **Water, Air, and Soil Pollution**, v. 145, n. 1-4, p. 187-203, 2003.

HÜBNER, S. *et al.* Electron properties in an atmospheric helium plasma jet determined by Thomson scattering. **Journal of Physics D:** Applied Physics, v. 47, n. 43, 2014.

ISO 10993-5-**Biological Evaluation of Medical Devices-**Part 5-Tests for in vitro cytotoxicity. In: Standardization) ItIOf, editor. 2009.

JIANG, H. *et al.* Experimental study of Q-V Lissajous figures in nanosecond-pulse surface discharges. **IEEE Transactions on Dielectrics and Electrical Insulation**, v. 20, n. 4, p. 1101-1111, 2013.

JIN, D. J.; UHM, H. S.; CHO, G. Influence of the gas-flow Reynolds number on a plasma column in a glass tube. **Physics of Plasmas**, v. 083513, n. May, 2013.

JIN, Y. *et al.* Atmospheric pressure plasma jet in ar and O2/Ar mixtures: Properties and high performance for surface cleaning. **Plasma Science and Technology**, v. 15, n. 12, p. 1203-1208, 2013.

JOSHI, S. G. *et al.* Nonthermal dielectric-barrier discharge plasma-induced inactivation involves oxidative DNA damage and membrane lipid peroxidation in *Escherichia coli.* **Antimicrobial Agents and Chemotherapy**, v. 55, n. 3, p. 1053-1062, 2011.

KARAKAS, E.; AKMAN, M. A.; LAROUSSI, M. The evolution of atmospheric-pressure low-temperature plasma jets: Jet current measurements. **Plasma Sources Science and Technology**, v. 21, n. 3, 2012.

KAWASAKI, T. *et al.* Detection of reactive oxygen species supplied into the water bottom by atmospheric nonthermal plasma jet using iodine-starch reaction. **Japanese Journal of Applied Physics**, v. 54, n. 8, 2015.

KIM, G. J. *et al.* DNA damage and mitochondria dysfunction in cell apoptosis induced by nonthermal air plasma. **Applied Physics Letters**, v. 96, n. 2, 2010.

KIM, S. J. *et al.* Induction of apoptosis in human breast cancer cells by a pulsed atmospheric pressure plasma jet. **Applied Physics Letters**, v. 97, n. 2, p. 2008-2011, 2010.

KLÄMPFL, Tobias Gabriel. **Cold atmospheric plasma decontamination against nosocomial bacteria**. 162 f. PhD thesis. University of Munich, 2014.

KOGELSCHATZ, U; ELIASSON, B; EGLI, W. Dielectric-barrier discharges. Principle and applications. **Journal de Physique IV Colloque**, v. 7, n. C4, p. 47-66, 1997.

KOGELSCHATZ, U. Dielectric barrier discharge: their history, discharge physic, and industrial applications. **Plasma Chemistry and Plasma Processing**, v. 23, n. 1, p. 1, 2003.

KONG, F. *et al.* Surface modification of polystyrene and their stability: a comparison of DBD plasma deposition and direct fluorination. **Applied Surface Science**, v. 459, p. 300-308, 2018.

KOSTOV, K. G. *et al.* Surface modification of polymeric materials by cold atmospheric plasma jet. **Applied Surface Science**, v. 314, 2014.

KOSTOV, K. G. *et al.* Study of polypropylene surface modification by air dielectric barrier discharge operated at two different frequencies. **Surface and Coatings Technology**, v. 234, 2013.

KOSTOV, K. G. *et al.* Study of cold atmospheric plasma jet at the end of flexible plastic tube for microbial decontamination. **Plasma Processes and Polymers**, v. 12, n. 12, 2015a.

KOSTOV, K. G. *et al.* Inactivation of *Candida albicans* by cold atmospheric pressure plasma jet. **IEEE Transactions on Plasma Science**, v. 43, n. 3, p. 770-775, 2015b.

KOSTOV, K. G. *et al.* Transfer of a cold atmospheric pressure plasma jet through a long flexible plastic tube. **Plasma Sources Science and Technology**, v. 24, n. 2, 2015c.

LACKMANN, J.-W. *et al.* Photons and particles emitted from cold atmospheric-pressure plasma inactivate bacteria and biomolecules independently and synergistically. **Journal of the Royal Society,** v. 10, n. 89, p. 20130591, 2013.

LACKMANN, J.-W.; BANDOW, J. E. Inactivation of microbes and macromolecules by atmospheric-pressure plasma jets. **Applied Microbiology and Biotechnology**, v. 98, n. 14, p. 6205-6213, 2014.

LAROUSSI, M. Plasma medicine: a brief introduction. **Plasma**, v. 1, n. 1, p. 47-60, 2018.

LAUX, C. O. *et al.* Optical diagnostics of atmospheric pressure air plasmas. **Plasma Sources Sci. Technol.**, v. 12, p. 125-138, 2003.

LEE, M. *et al.* Blood coagulation with atmospheric-plasma jets. 2012 **IEEE 39th International Conference on Plasma Sciences (ICOPS)**, 2012.

LIAO, X. *et al.* Inactivation mechanisms of non-thermal plasma on microbes: a review. **Food Control**, v. 75, p. 83-91, 2017.

LIEBERMAN, M. A.; LICHTENBERG, A. J. **Principles of plasma discharges and materials processing**. 2.ed. New Jersey: John Wiley & Sons, 2005.

LIN, Z. H. *et al.* Ar/O2 argon-based round atmospheric-pressure plasma jet on sterilizing bacteria and endospores. **IEEE Transactions on Plasma Science**, v. 44, n. 12, p. 3140-3147, 2016.

LIU, L. **Physics of electrical discharge transitions in air**. 56 f. PhD thesis (PhD in electrical engineering) KTH Royal Institute of Technology School of Electrical Engineering, 2017.

LOEB, L. B.; MEEK, J. M. The mechanism of spark discharge in air at atmospheric pressure. I. **Journal of Applied Physics**, v. 11, n. 6, p. 438-447, 1940a.

LOEB, L. B.; MEEK, J. M. The mechanism of spark discharge in air at atmospheric pressure. II. **Journal of Applied Physics**, v. 11, n. 6, p. 459-474, 1940b.

LU, X.; LAROUSSI, M.; PUECH, V. On atmospheric-pressure non-equilibrium plasma jets and plasma bullets. **Plasma Sources Science and Technology**, v. 21, n. 3, 2012.

LU, X. *et al.* Guided ionization waves: theory and experiments. **Physics Reports**, v. 540, n. 3, p. 123-166, 2014.

LU, X. *et al.* Reactive species in non-equilibrium atmospheric-pressure plasmas: generation, transport, and biological effects. **Physics Reports**, v. 630, n. April, p. 1-84, 2016.

LUAN, P. *et al.* Model polymer etching and surface modification by a time modulated RF plasma jet: Role of atomic oxygen and water vapor. **Journal of Physics D:** Applied Physics, v. 50, n. 3, 2017.

MALIK, M. A.; GHAFFAR, A.; MALIK, S. A. Water purification by electrical discharges. **Plasma Sources Science and Technology**, v. 10, n. 1, p. 82-91, 2001.

MCKAY, K. *et al.* Mass spectrometric diagnosis of an atmospheric pressure helium microplasma jet. **Journal of Physics D:** Applied Physics, v. 46, n. 46, 2013.

MEI, D. *et al.* Plasma-assisted conversion of CO_2 in a dielectric barrier discharge reactor: understanding the effect of packing materials. **Plasma Sources Science and Technology**, v. 24, n. 1, p. 015011, 2014.

MERCHE, D.; VANDENCASTEELE, N.; RENIERS, F. Atmospheric plasmas for thin film deposition: a critical review. **Thin Solid Films**, v. 520, n. 13, p. 4219-4236, 2012.

MERICAM-BOURDET, N. *et al.* Experimental investigations of plasma bullets. **Journal of Physics D:** Applied Physics, v. 42, n. 5, 2009.

METELMANN, H-R., VON WOEDTKE, T., WELTMANN, K-D. **Comprehensive clinical plasma medicine**. Springer International Publishing, 2018. 526 p.

MILDE, H. I. Pulse corona discharge in electrostatic precipitators. **IEEE Transactions on Electrical Insulation**, v. EI-17, n. 2, p. 179-186, 1982.

MORITZ, A. R.; HENRIQUES, F. C. Studies of thermal injury II: the relative importance of time and surface temperature in the causation of cutaneous burns. **American Journal of Pathology**, v. 23, p. 695-720, 1947.

MORITZ, M. *et al.* Atmospheric pressure plasma jet treatment of *Salmonella enteritidis* inoculated eggshells. **International Journal of Food Microbiology**, v. 245, n. 2016, p. 22-28, 2017.

MUSA, G. P. *et al.* An atmospheric-pressure plasma jet treatment of polyethylene polymer films for wettability enhancement. **Science World Journal**, v. 11, n. 2, p. 27-29, 2016.

NASTUTA, A.V. *et al.* Atmospheric pressure plasma jets in inert gases: electrical, optical and mass spectrometry diagnosis. **Romanian Reports in Physics**, v. 69, n. 1, p. 1-9, 2017.

NEHRA, V.; KUMAR, A.; DWIVEDI, H K. Atmospheric Non-Thermal Plasma Sources. **International Journal of Engineering**, v. 2, n. 1, p. 53-68, 2008.

NISHIME, T. M.C. *et al.* Non-thermal atmospheric pressure plasma jet applied to inactivation of different microorganisms. **Surface and Coatings Technology**, v. 312, p. 19-24, 2016.

NISHIME, Thalita Mayumi Castaldelli. **Jato de plasma frio em pressão atmosférica para tratamento de materiais e esterilização**. 112 f. Master dissertation (master in physics) São Paulo State University (Unesp), 2015.

OH, J. S.; WALSH, J. L.; BRADLEY, J. W. Plasma bullet current measurements in a free-stream helium capillary jet. **Plasma Sources Science and Technology**, v. 21, n. 3, 2012.

OLDHAM, C. J. **Applications of Atmospheric Plasmas.** 292 f. PhD thesis (PhD in materials science and engineering). North Carolina State University, 2009.

OMRAN, A. V. *et al.* Single channel atmospheric pressure transporting plasma and plasma stream demultiplexing: Physical characterization and application to E. coli bacteria inactivation. **Journal of Physics D:** Applied Physics, v. 50, n. 31, 2017.

ONYSHCHENKO, I. *et al.* Atmospheric pressure plasma penetration inside flexible polymeric tubes. **Plasma Processes and Polymers**, v. 12, n. 3, p. 271-284, 2015a.

ONYSHCHENKO, I.; DE GEYTER, N.; MORENT, R. Improvement of the plasma treatment effect on PET with a newly designed atmospheric pressure plasma jet. **Plasma Processes and Polymers**, v. 14, n. 8, 2017.

ONYSHCHENKO, I. *et al.* Local analysis of pet surface functionalization by an atmospheric pressure plasma jet. **Plasma Processes and Polymers**, v. 12, n. 5, p. 466–476, 2015b.

PARK, S.-L. *et al.* Effective ozone generation utilizing a meshed-plate electrode in a dielectric-barrier discharge type ozone generator. **Journal of Electrostatics**, v. 64, p. 275-282, 2006.

PENKOV, O. V. *et al.* A review of recent applications of atmospheric pressure plasma jets for materials processing. **Journal of Coatings Technology and Research**, v. 12, n. 2, p. 225-235, 2015.

POLAK, M. *et al.* Innovative plasma generation in flexible biopsy channels for inner-tube decontamination and medical applications. **Plasma Processes and Polymers**, v. 9, n. 1, p. 67-76, 2012.

PRYSIAZHNYI, V.; SATURNINO, V. F. B.; KOSTOV, K. G. Transferred plasma jet as a tool to improve wettability of inner surfaces of polymer tubes. **International Journal of Polymer Analysis and Characterization**, v. 22, n. 3, p. 215-221, 2017.

RAETHER, H. **Electron avalanches and breakdown in gases**. London: Butterworths, 1964.

RAISER, J; ZENKER, M. Argon plasma coagulation for open surgical and endoscopic applications: state of the art. **Journal of Physics D:** Applied Physics, v. 39, n. 16, p. 3520-3523, 2006.

RAIZER, Y. P. **Gas discharge physics**. New York: Springer Berlin Heidelberg, 1991.

RATOVITSKI, E. A. *et al.* Anti-cancer therapies of 21st century: novel approach to treat human cancers using cold atmospheric plasma. **Plasma Processes and Polymers**, v. 11, n. 12, p. 1128-1137, 2014.

REUTER, S.; VON WOEDTKE, T.; WELTMANN, K. D. The kINPen - A review on physics and chemistry of the atmospheric pressure plasma jet and its applications. **Journal of Physics D:** Applied Physics, v. 51, n. 23, 2018.

REUTER, S. *et al.* Controlling the ambient air affected reactive species composition in the effluent of an argon plasma jet. **IEEE Transactions on Plasma Science**, v. 40, n. 11, p. 2788-2794, 2012.

ROBERT, E. *et al.* Perspectives of endoscopic plasma applications. **Clinical Plasma Medicine**, v. 1, n. 2, p. 8-16, 2013.

ROBERT, E. *et al.* Experimental study of a compact nanosecond plasma gun. **Plasma Processes and Polymers**, v. 6, n. 12, p. 795-802, 2009.

ROCHA, Vanessa. **Esterilização de materiais termossensíveis através de aplicação de plasma gerado por descarga com barreira dielétrica (DBD)**. 160 f. Master dissertation (master in physics). Universidade Estadual Paulista (Unesp). Faculdade de engenharia de Guaratinguetá, 2009.

ROLAND, U. *et al.* A new fiber optical thermometer and its application for process control in strong electric, magnetic, and electromagnetic fields. **Sensor Letters**, v. 1, p. 93-98, 2003.

SANTOS, Alessandro Luiz Ribeiro dos. **Estudo de polímeros comerciais tratados a plasma em pressão atmosférica**. 82 f. Master dissertation (master in physics). São Paulo State University, 2010.

SARANI, A.; NIKIFOROV, A. Y.; LEYS, C. Atmospheric pressure plasma jet in Ar and Ar/ H_2O mixtures: optical emission spectroscopy and temperature measurements. **Physics of Plasmas**, v. 17, n. 6, 2010.

SCHMIDT-BLEKER, A. *et al.* Propagation mechanisms of guided streamers in plasma jets: the influence of electronegativity of the surrounding gas. **Plasma Sources Science and Technology**, v. 24, n. 3, 2015.

SHAO, X. J. *et al.* Research on surface modification of polytetrafluoroethylene coupled with argon dielectric barrier discharge plasma jet characteristics. **IEEE Transactions on Plasma Science**, v. 39, n. 11 Part 2, p. 3095-3102, 2011.

SHAW, D. *et al.* Mechanisms behind surface modification of polypropylene film using an atmospheric-pressure plasma jet. **Plasma Sources Science and Technology**, v. 25, n. 6, 2016.

SHISHOO, R. **The Use of Renewable Resource Based Materials for Technical Textiles Applications.** Woodhead Publishing Limited, 2007.

SOUZA, João Henrique Campos de. **Estudos de esterilização por plasma a pressão atmosférica**. 110 f. PhD thesis (PhD in physics). Universidade de Brasília, 2012.

STOFFELS, E. "Tissue processing" with atmospheric plasmas. **Contributions to Plasma Physics**, v. 47, p. 40-48, 2007.

TENDERO, C. *et al.* Atmospheric pressure plasmas: A review. **Spectrochimica Acta -** Part B Atomic Spectroscopy, v. 61, n. 1, p. 2-30, 2006.

TESCHKE, M. *et al.* High-speed photographs of a dielectric barrier atmospheric pressure plasma jet. **IEEE Transactions on Plasma Science**, v. 33, n. 2 I, p. 310-311, 2005.

VAN DEYNSE, A. *et al.* Surface activation of polyethylene with an argon atmospheric pressure plasma jet: Influence of applied power and flow rate. **Applied Surface Science**, v. 328, p. 269-278, 2015.

VESEL, A.; MOZETIC, M. New developments in surface functionalization of polymers using controlled plasma treatments. **Journal of Physics D:** Applied Physics, v. 50, n. 29, p. 293001, 2017.

WAGNER, H. *et al.* The barrier discharge: basic properties and applications to surface treatment. **Vacuum**, v. 71, p. 417-436, 2003.

WALSH, J. L.; KONG, M. G. Contrasting characteristics of linear-field and cross-field atmospheric plasma jets. **Applied Physics Letters**, v. 93, n. 11, p. 1-4, 2008.

WEISS, M. *et al.* Cold atmospheric plasma treatment induces anti-proliferative effects in prostate cancer cells by redox and apoptotic signaling pathways. **PLoS ONE**, v. 10, n. 7, p. 1-17, 2015.

WINTER, J. *et al.* On the development of a deployable cold plasma endoscope. **Contributions to Plasma Physics**, v. 58, n. 5, 2018.

WINTER, J. *et al.* Enhanced atmospheric pressure plasma jet setup for endoscopic applications. **Journal of Physics D:** Applied Physics, v. 52, n. 2, 2019.

XU, G. M. *et al.* Low-temperature atmospheric pressure helium plasma jet damages malignant melanoma cells by inducing oxidative stress. **IEEE Transactions on Plasma Science**, v. 46, n. 8, p. 2805-2813, 2018.

YAMAZAKI, H. *et al.* Microbicidal activities of low frequency atmospheric pressure plasma jets on oral pathogens. **Dental materials journal**, v. 30, n. 3, p. 384–391, 2011.

YAN, D.; SHERMAN, J. H.; KEIDAR, M. Cold atmospheric plasma, a novel promising anti-cancer treatment modality. **Oncotarget**, v. 8, n. 9, p. 15977-15995, 2017.

YUSUPOV, M. *et al.* Synergistic effect of electric field and lipid oxidation on the permeability of cell membranes. **Biochimica et Biophysica Acta -** General Subjects, v. 1861, n. 4, p. 839-847, 2017.

ZAHORANOVÁ, A. *et al.* Effect of cold atmospheric pressure plasma on the wheat seedlings vigor and on the inactivation of microorganisms on the seeds surface. **Plasma Chemistry and Plasma Processing**, v. 36, n. 2, p. 397-414, 2016.

ZHANG, X.; CHA, M. S. Electron-induced dry reforming of methane in a temperature-controlled dielectric barrier discharge reactor. **Journal of Physics D:** Applied Physics, v. 46, n. 41, 2013.

ZHOU, R. *et al.* Synergistic effect of atmospheric-pressure plasma and TiO_2 photocatalysis on inactivation of *Escherichia coli* cells in aqueous media. **Scientific Reports**, v. 6, p. 1-10, 2016.

PUBLISHED PAPERS

The work presented in this Ph.D. thesis led to publication of the following papers:

[1] WINTER, J.; NISHIME, T. M. C.; BANSEMER, R.; BALANZINSKI, M.; WENDE, K.; WELTMANN, K-D. Enhanced atmospheric pressure plasma jet setup for endoscopic applications. **Journal of Physics D:** applied physics, v. 52, n. 2, 2019.

[2] WINTER, J.; NISHIME, T. M. C.; GLITSCH, S.; LÜHDER, H.; WELTMANN, K-D. On the development of a deployable cold plasma endoscope. **Contributions to Plasma Physics**, v. 58, n. 5, 2018.

[3] BORGES, A. C.; LIMA, G. M. G.; NISHIME, T. M. C.; GONTIJO, A. V. L.; KOSTOV, K. G.; KOGA-ITO, C. Y. Amplitude-modulated cold atmospheric pressure plasma jet for treatment of oral candidiasis: *in vivo* study. **PLoS ONE**, v. 13, n. 6, p. 1-19, 2018.

[4] KOSTOV, K G; BORGES, A C; KOGA-ITO, C Y; NISHIME, T. M. C.; PRYSIAZHNYI, V.; HONDA, R. Y. Inactivation of *Candida albicans* by cold atmospheric pressure plasma jet. **IEEE Transactions on Plasma Science**, v. 43, n. 3, p. 770-775, 2015.

[5] KOSTOV, K. G.; NISHIME, T. M. C.; MACHIDA, M.; BORGES, A. C.; PRYSIAZHNYI, V.; KOGA-ITO, C. Y. Study of cold atmospheric plasma jet at the end of flexible plastic tube for microbial decontamination. **Plasma Processes and Polymers**, v. 12, n. 12, 2015.